DNA-functionalized Gold Nanoparticles for Enhanced Molecular Sensing

By

Stephen R. Jackson

Dissertation

Submitted to the Faculty of the

Graduate School of Vanderbilt University

in partial fulfillment of the requirements

for the degree of

DOCTOR OF PHILOSOPHY

in

Chemistry

August, 2014

Nashville, Tennessee

Approved:

Professor David W. Wright

Professor Sandra J. Rosenthal

Professor Frederick R. Haselton

Professor Eva M. Harth

To my family & Ed

ACKNOWLEDGEMENTS

This work would not have been possible without the assistance of many people. First and foremost, I must thank my research advisor, Dr. David Wright. None of my accomplishments in graduate school would have been possible without David's support and mentorship. Graduate school is nothing if not a humbling experience and during my tenure at Vanderbilt, there have been many days of reflection on which I (and most likely David too) have wondered exactly why it was that he consented to my joining his lab. Nonetheless, he's repeatedly made me feel as though his appreciations for my strengths as a researcher outweigh any frustrations with my weaknesses. For that, as well as his guidance and patience, I am truly grateful.

I certainly wouldn't be where I am today without the mentorship of Dr. Tom Goodwin, who allowed me to gain my first research experience in his lab at Hendrix College. Dr. Goodwin's passion for research was infectious, and while working with him, he provided me with the skills as well as the confidence to pursue a graduate degree.

I would also like to extend great thanks to my dissertation committee members, Dr. Rosenthal, Dr. Haselton, and Dr. Harth. I thank you for all of the constructive discussions during my committee meetings. Each of your comments and suggestions has contributed towards and strengthened this work. A great deal of acknowledgement for the content of this dissertation also goes to

Dr. Ashwath Jayagopal. Besides being a productive collaborator and scientific resource, Ash has been a good friend. More than anyone, he's made me feel like my skills as a scientist are valued and appreciated by seemingly never missing a chance to talk me up to both his friends and colleagues. Ash, it was neither unnoticed nor unwelcome, even if I may have pooh-poohed it at the time.

Throughout my graduate career, I have seldom had a dull day's work and I think that is a testament to the fantastic group of people that I've had the privilege of working alongside. I'd like to thank past Wright Lab members Ryan and Alex Rutledge, Leila Deravi, Melissa Carter, Reese Harry, Jonas Perez, Anh Hoang, Kristin Halfpenny, Josh Swartz, John Stone, and Becca Sandlin, who all made me feel welcomed into the lab as a young graduate student. Likewise, I must thank current lab members Nick Adams, Chris Gulka, Jenny Nesbitt, Keersten Davis, Anna Bitting, Kim Fong, Adam Ryan Travis, Wes Bauer, Nicholas Wright, Alexis Wong, Lauren Gibson, and Christine Markwalter, a group that will surely make it difficult to leave. I've never been a part of a more talented group of people, and I'm fortunate to consider each one of them a friend.

My support network here at Vanderbilt has gone beyond my amazing friends and coworkers, and I'd be remiss if I didn't acknowledge the folks at the Vanderbilt Psychological & Counseling Center, in particular Dr. Amy Best and Ellen Clark. Like most everyone else listed in these acknowledgements, this work could not have been completed without their help and support.

Finally, I'd like to acknowledge those to whom this work is dedicated: Edward Hawkins, a talented chemist and kind soul that was lost much too soon,

and most of all, my family, the constant source of love and support during the entirety of this work and beyond. Thanks again to you all.

TABLE OF CONTENTS

LIST OF FIGURES

Figure Page

CHAPTER I

INTRODUCTION

Imaging RNA in Living Systems

Increasing evidence suggests that RNA is responsible for a wide range of functions in living cells (1,2). The important role RNA plays in dictating cell behavior has led to the development of numerous methods for detecting RNA in living systems. A promising tool for RNA detection is molecular beacon (MB) technology. MBs were initially developed as a probe for quantifying nucleic acids in real-time (3). MBs combine the specificity of nucleic acid hybridization with the ability of nucleic acids to take on distinct confirmations to create hairpin-shaped oligonucleotides with a fluorophore at one end and a proximity-dependent quencher at the other end. When target nucleic acids are not present, the hairpin structure keeps the fluorophore in close proximity to the quencher and the probes are in a “dark” state. When the probes bind to their targets, they undergo a conformational reorganization that separates the fluorophore from the quencher, resulting in a bright fluorescent signal that indicates the presence of the target. Since their inception, MBs have found wide application in molecular and cellular biology, pathogen detection, and molecular diagnostics (4-7).

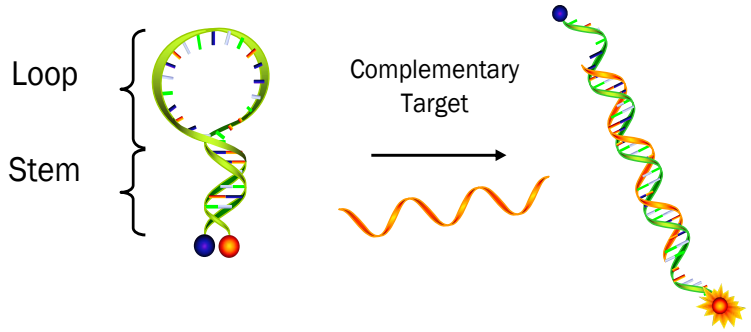

Figure 1. Diagram of a MB in a hybridized and unhybridized state (8).

Advances in MB design and modifications have enabled imaging of RNA in living cells (9,10). However, challenges encountered in using traditional MBs for in vivo imaging include nonspecific background fluorescence, potential for nuclease degradation, and reduced half-life, and limited approaches for noninvasive intracellular delivery mechanisms. Continued development of MBs has resulted in improvements to address these limitations.

Improved MB Signal to Noise Ratio

Key issues in using MBs for imaging are maximization of quenching efficiency as well as fluorophore quantum efficiency. One strategy to improve the signal-to-background ratio is to increase the brightness of the signaling moiety. Replacement of organic fluorophores with brighter signaling materials, such as quantum dots, has been reported (11). A second strategy is to minimize the fluorescence background using a more efficient quencher. While standard organic quenchers have demonstrated effectiveness in the quenching of some fluorophores, their quenching efficiencies vary significantly from one dye to another. For example, 4-((4-(dimethylamino)phenyl)azo)benzoic acid (DABCYL)

efficiently quenches fluorescein (FAM) but is much less efficient for dyes emitting at longer wavelengths such as Cy5 and Texas Red (12). Black Hole Quenchers (BHQ) have no native fluorescence and a broad effective range of absorption, but it is still important to match the BHQ with the appropriate dye. Pairing multiple assembled quenchers to one fluorophore has also been shown to provide better quenching efficiency (13). The development of quenchers which work effectively within the near infrared range open up exciting possibilities for imaging of RNA with minimal cell or tissue autofluorescence.

Nuclease Degradation

MBs are vulnerable to intracellular enzymatic degradation, such as DNAse/RNAse cleavage and non-specific opening by single strand binding proteins leading to false-positives (14). To improve the resistance of enzymatic activites, non-standard nucleic acids have been explored to design MBs, such as 2'-O-methyl-modified RNAs, peptide nucleic acids (PNAs), and locked nucleic acids (LNAs). 2'-O-methyl MBs show higher affinity, increased specificity, and faster hybridization kinetics (15-17). However, evidence suggests that not all 2'-O-methyl MBs retain a stem-loop structure inside living cells, possibly due to nucleic acid binding proteins (18). PNAs have neutral polyamide backbones, are not degraded by nucleases, and have faster hybridization kinetics than DNA probes (19). However, PNAs have not been widely used mainly because they have poor water solubility causing aggregation in biological environments (20). LNAs are nucleic acid analogues, in which the ribose ring is locked into a rigid

C3’ endo or Northern-type conformation by a simple 2’-O, 4’-C methylene bridge. LNAs as well as LNA-MBs have many attractive properties, such as high binding affinity, excellent base mismatch discrimination capability, and decreased susceptibility to nuclease digestion, making them important tools for synthesizing MBs (21).

Approaches for Delivery of MBs in Live Cells

A limitation of traditional MBs is the need to permeabilize the cell through microinjection or use of pore-forming reagents, such as streptolysin O, for effective delivery and target hybridization (9). The use of cell penetrating peptides conjugated to MBs was recently reported to provide for translocation of MBs into cells without poreforming reagents; however, Tat-linked MBs have been observed to enter the nucleus, causing nonspecific background signal due to opening of the construct within that compartment (22). In a different approach to achieve delivery of MBs, Seferos *et al*., developed a MB-based technique called “nano-flares” based on oligonucleotide-modified AuNPs that take advantage of the fact that AuNPs functionalized with oligonucleotides efficiently enter live cells without the aid of transfection/permeabilization agents (23). Their probe consists of a AuNP conjugated to many sequences of single stranded DNA (ssDNA), which are complementary to the RNA sequence of interest (Figure 2).

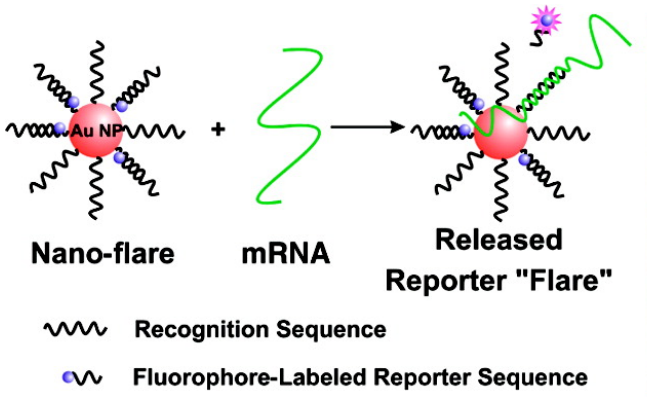

Figure 2. Diagram of a nano-flare (23).

Short “reporter” strands of fluorescently tagged ssDNA are hybridized to the probe DNA. In this state, the organic fluorophore is quenched as a result of its proximity to the AuNP surface. Upon hybridization of the probe strand with the target RNA complement, the reporter strand is displaced, spatially separating it from the AuNP and resulting in a fluorescent signal that can be correlated to the presence of the RNA sequence of interest. This design yields a signal that is separated from the hybridized RNA/nanoflare construct, consequently important spatial information is lost in live cell microscopy applications. DNA hairpin-gold nanoparticles (hAuNPs) provide spatiotemporal information about target oligonucleotides when used in live cells (24). hAuNPs utilize the fluorescence quenching ability of a 15 nm AuNP, where DNA hairpins are attached to the particle via a gold-thiol bond through a 5’ hexane thiol linker. A 3’ fluorophore is quenched by the AuNP until the hairpin binds a complementary sequence, extending the fluorophore past the quenching distance of the AuNP (Figure 3). This results in a positive fluorescent signal, allowing high specificity and high

sensitivity imaging of messenger RNA (mRNA) in live cells for elucidating spatial and temporal aspects of mRNA expression and trafficking.

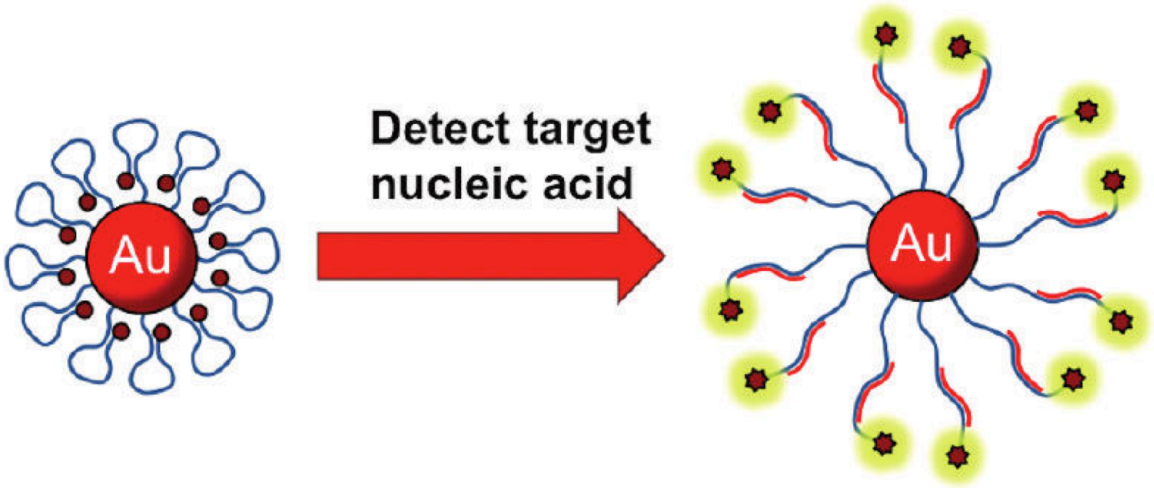

Figure 3. Hairpin DNA-gold nanoparticles (hAuNPs). The AuNP quenches the fluorophore-modified hairpin DNA. Upon binding the target nucleic acid, the hairpin DNA opens and the fluorescence is detected (12).

Outlook

Since their introduction in 1996, much progress has been made in improving applications of MBs. The flexibility of their chemical modificiation and their cost-effectiveness has led to applications in biology, chemistry, biomedicine, and biotechnology. Continuing efforts to improve MB-based technology, such as the optimization of signal transduction use of modified bases, and AuNP-based constructs will surely catalyze the development of new biochemical and biomedical applications.

References

1. Kleinman, M.E., Yamada, K., Takeda, A., Chandrasekaran, V., Nozaki, M., Baffi, J.Z., Albuquerque, R.J., Yamasaki, S., Itaya, M., Pan, Y. *et al.* (2008) Sequence- and target-independent angiogenesis suppression by siRNA via TLR3. *Nature*, **452**, 591-597.

2. Zhou, Q., Gallagher, R., Ufret-Vincenty, R., Li, X., Olson, E.N. and Wang, S. (2011) Regulation of angiogenesis and choroidal neovascularization by members of microRNA-23~27~24 clusters. *Proc Natl Acad Sci U S A*, **108**, 8287-8292.

3. Tyagi, S. and Kramer, F.R. (1996) Molecular beacons: Probes that fluoresce upon hybridization. *Nature Biotechnology*, **14**, 303-308.

4. Sandhya, S., Chen, W. and Mulchandani, A. (2008) Molecular beacons: a real-time polymerase chain reaction assay for detecting Escherichia coli from fresh produce and water. *Anal Chim Acta*, **614**, 208-212.

5. Santangelo, P.J. (2010) Molecular beacons and related probes for intracellular RNA imaging. *Wiley Interdiscip Rev Nanomed Nanobiotechnol*, **2**, 11-19.

6. Santangelo, P.J., Alonas, E., Jung, J., Lifland, A.W. and Zurla, C. (2012) Probes for intracellular RNA imaging in live cells. *Methods Enzymol*, **505**, 383-399.

7. Yeh, H.Y., Yates, M.V., Mulchandani, A. and Chen, W. (2008) Visualizing the dynamics of viral replication in living cells via Tat peptide delivery of nuclease-resistant molecular beacons. *Proc Natl Acad Sci U S A*, **105**, 17522-17525.

8. Kim, Y., Sohn, D. and Tan, W. (2008) Molecular beacons in biomedical detection and clinical diagnosis. *Int J Clin Exp Pathol*, **1**, 105-116.

9. Santangelo, P., Nitin, N. and Bao, G. (2006) Nanostructured probes for RNA detection in living cells. *Ann Biomed Eng*, **34**, 39-50.

10. Santangelo, P.J., Nitin, N. and Bao, G. (2005) Direct visualization of mRNA colocalization with mitochondria in living cells using molecular beacons. *J Biomed Opt*, **10**, 44025.

11. Kim, J.H., Morikis, D. and Ozkan, M. (2004) Adaptation of inorganic quantum dots for stable molecular beacons. *Sensors and Actuators B-Chemical*, **102**, 315-319.

12. Adams, N.M., Jackson, S.R., Haselton, F.R. and Wright, D.W. (2012) Design, synthesis, and characterization of nucleic-acid-functionalized gold surfaces for biomarker detection. *Langmuir*, **28**, 1068-1082.

13. Yang, C.J., Lin, H. and Tan, W. (2005) Molecular assembly of superquenchers in signaling molecular interactions. *J Am Chem Soc*, **127**, 12772-12773.

14. Fang, X.H., Li, J.J. and Tan, W.H. (2000) Using molecular beacons to probe molecular interactions between lactate dehydrogenase and single-stranded DNA. *Analytical Chemistry*, **72**, 3280-3285.

15. Bratu, D.P., Cha, B.J., Mhlanga, M.M., Kramer, F.R. and Tyagi, S. (2003) Visualizing the distribution and transport of mRNAs in living cells. *Proc Natl Acad Sci U S A*, **100**, 13308-13313.

16. Catrina, I.E., Marras, S.A. and Bratu, D.P. (2012) Tiny molecular beacons: LNA/2'-O-methyl RNA chimeric probes for imaging dynamic mRNA processes in living cells. *ACS Chem Biol*, **7**, 1586-1595.

17. Perlette, J. and Tan, W. (2001) Real-time monitoring of intracellular mRNA hybridization inside single living cells. *Anal Chem*, **73**, 5544-5550.

18. Molenaar, C., Marras, S.A., Slats, J.C., Truffert, J.C., Lemaitre, M., Raap, A.K., Dirks, R.W. and Tanke, H.J. (2001) Linear 2' O-Methyl RNA probes for the visualization of RNA in living cells. *Nucleic Acids Res*, **29**, E89-89.

19. Xi, C.W., Balberg, M., Boppart, S.A. and Raskin, L. (2003) Use of DNA and peptide nucleic acid molecular beacons for detection and quantification of rRNA in solution and in whole cells. *Applied and Environmental Microbiology*, **69**, 5673-5678.

20. Braasch, D.A. and Corey, D.R. (2001) Synthesis, analysis, purification, and intracellular delivery of peptide nucleic acids. *Methods*, **23**, 97-107.

21. Vester, B. and Wengel, J. (2004) LNA (locked nucleic acid): high-affinity targeting of complementary RNA and DNA. *Biochemistry*, **43**, 13233-13241.

22. Chen, A.K., Behlke, M.A. and Tsourkas, A. (2008) Efficient cytosolic delivery of molecular beacon conjugates and flow cytometric analysis of target RNA. *Nucleic Acids Res*, **36**, e69.

23. Seferos, D.S., Giljohann, D.A., Hill, H.D., Prigodich, A.E. and Mirkin, C.A. (2007) Nano-flares: probes for transfection and mRNA detection in living cells. *J Am Chem Soc*, **129**, 15477-15479.

24. Jayagopal, A., Halfpenny, K.C., Perez, J.W. and Wright, D.W. (2010) Hairpin DNA-functionalized gold colloids for the imaging of mRNA in live cells. *J Am Chem Soc*, **132**, 9789-9796.

CHAPTER II

OPTIMIZATION OF HAIRPIN DNA-FUNCTIONALIZED GOLD NANOPARTICLES FOR mRNA IMAGING

As mentioned in Chapter I, our group has developedd a new strategy to detect mRNA in live cells: hairpin DNA-gold nanoparticles (hAuNPs). More specifically, our laboratory reported the first use of hAuNP probes for investigating spatiotemporal RNA trafficking in live cells (1,2). Targets for respiratory syncytial virus (RSV) mRNA and glyceraldehyde 3-phosphate dehydrogenase (GAPDH) mRNA were conjugated to 15 nm AuNPs and used in live, RSV-infected and uninfected HEp-2 cells (1). Due to its stable, constitutive expression in almost all mammalian cell types, GAPDH serves as a useful internal control for normalization in standard quantitative molecular biology assays such as RT-PCR. The detection of RSV mRNA concurrently with GAPDH mRNA as an internal control in the assay enabled real-time analysis of mRNA transport and processing in live cells. Similar hAuNP constructs have also been used to positively identify tyrosinase, a common melanoma gene target, in primary melanoma tumor cells (2).

Through these studies, hAuNPs have been shown to enable specific and sensitive imaging of mRNA in live cells and elucidate spatial and temporal aspects of mRNA expression and trafficking. Yet there is still room for improvement in the design and synthesis of these probes. Specifically,

opportunities exist to increase the overall signal-to-noise of the probes by both increasing the overall brightness and decreasing inherent background fluorescence. In order to expand upon the current capabilities and applications of hAuNPs, a series of optimization experiments were performed to elucidate the optimal parameters for a molecular beacon/gold nanoparticle construct. This chapter highlights these studies, specifically detailing experiments concerning particle size, ligand coverage, and hairpin design.

The optical properties of gold nanoparticles make them a well-suited platform for biomarker detection applications. When metallic nanoparticles of a size comparable to the electron mean free path in metals (~100 nm) are irradiated with light having specific frequencies, collective oscillations of electrons are observed along the metallic surface. These oscillations are termed surface "plasmons" or localized surface plasmon resonances (SPRs) (3). For spherical AuNPs (5-200 nm), these collective oscillations are in resonance with the incident radiation in the visible region of the electromagnetic spectrum, giving rise to a characteristic plasmon absorption band centered at 520 nm (3). As gold particles increase in size, the increase in diameter is also accompanied by an increase in the extinction coefficient and a red shift in the plasmon band. The net result is that particles with a diameter of around 15-100 nm are most visible to the human eye. Particles with an 80 nm diameter have an extinction coefficient of around 9×10^{10} M^{-1} cm^{-1}. This exceeds the extinction coefficients of organic dyes by 4 or 5 orders of magnitude. While a larger extinction coefficient would theoretically make for a better quencher, other phenomena must be considered;

in particular, the enhanced electromagnetic field that arises when surface plasmons are confined, which would support smaller spheres acting as better quenchers. To determine the best size of particle for hAuNPs, the quenching radii of a range of sizes of gold nanospheres was determined by measuring the fluorescence of solutions of nanospheres coordinated with increasing lengths of thymine base-fluorophore sequences.

There are also a maximum number of DNA hairpins that will coat the surface of a gold sphere while at the same time avoiding steric interference with one another. It is critical to minimize steric hindrance due to overcrowding of ligands on the Au surface, as such crowding inhibits the hairpin DNA (hDNA) recognition and unfolding mechanism. By employing a smaller thiolated ligand as a spacing ligand, some control in varying the number, and therefore the steric effects, of the hDNA coordinated to the surface of the AuNP is gained. After incorporation of a spacing ligand the limit of detection of the probes in vitro is measured by introducing them to a range of concentrations of target and nonspecific control DNA.

We also want to take a more systematic approach to designing the DNA hairpins. Theoretically, any sequence within a target mRNA can be chosen as a site for molecular beacon binding. The endless possibilities give one the confidence that such regions are easily identified. While a universally ideal oligonucleotide probe sequence length has not been identified, empirical evidence suggests an optimal length in the range of 18-25 bases. This probe length is similar to many oligonucleotides used to prime PCR. Thus, the most

straightforward approach for probe sequence selection is to query the literature for priming sites used successfully in quantitative reverse transcription PCR (qRT-PCR) of the biomarker of interest. Using public databases and sequence comparison tools, we then confirm that the chosen probe sequence is unique to the target biomarker and has little or no homology with other cellular RNA sequences. However, the extent of target accessibility is primarily a consequence of complex secondary and tertiary intramolecular structures, which are not easy to predict and can mask many of these regions. To help predict these folding sites, we have employed RNAstructure, a program available as a free download from the Mathews Lab at the University of Rochester Medical Center (http://rna.urmc.rochester.edu/RNAstructure.html). In this way, we can ensure that the probe sequence is not hidden within secondary or tertiary structure that would inhibit binding and specific enough to identify only the RNA transcripts for our biomarker of interest.

Lastly, the effect of the proximal nucleotide base on the fluorophore will be investigated. hAuNPs used in previous studies have utilized a stem-forming region that resulted in the 3' fluorophore being conjugated to a guanine residue; however there are numerous reports in the literature of fluorescence quenching by an adjacent guanine nucleotide. Fluorescence emission from hAuNPs with identical hairpin recognition loop sequences, but different fluorophore proximal bases (C or G) were evaluated.

Methods

AuNP quenching radius

Prior to coupling of linear DNA to AuNPs, lyophilized DNA was resuspended in 100 mM DTT and 0.1 mM phosphate buffer (pH = 8.3) and incubated for one hour at room temperature (RT) to reduce residual 5' disulfide bonds. The number of nanoparticles/mL was calculated based off of the OD @ 520 nm, which then allowed for the calculation of total surface area/mL. The AuNP solutions were diluted with nuclease-free water to contain the same surface area (SA)/mL (4.532×10^{14} nm^2). One mL AuNP solutions were brought to 0.1% Tween-20. Linear DNA was added to the solution to give 200 nM DNA and incubated for 24 h. The solution was buffered to 10 mM phosphate buffer (pH 7.0) and brought to 0.1 M NaCl. The AuNPs were then incubated for an additional 4 h at RT. The NaCl concentration was adjusted to 0.2 M and the AuNPs were incubated for an additional 4 h at RT. Finally, the NaCl concentration was adjusted to 0.3 M and incubated for a final 4 h at RT. Fluorescence emission spectra of the solutions were collected on a BioTek microplate reader.

T10 spacing ligand

A 1 nM solution of 15 nm citrate-stabilized AuNPs was incubated with T10 DNA at room temperature while protected from light for one hour. To this solution, freshly reduced hDNA (5'-HS-TTT TTT TTT TCG ACG GAG TCC TTC CAC GAT ACC ACG TCG-TAMRA-3') was added and allowed to incubate overnight at room temperature and protected from light. After the initial loading period, the resulting solution was buffered to 10 mM phosphate buffer (PB, pH 7) with 0.1% Tween-20 and vortexed for 20 s. Three successive aliquots of 5 M NaCl were added to the buffered solution in 4 h intervals until a final concentration of 0.3 M NaCl was achieved. The resulting hAuNPs were purified by three centrifugation washes (20 min, 21,100 x g) and stored in phosphate buffered saline (PBS, pH 7.4) at RT.

To determine the DNA loading efficiency for each synthesis parameter, the core AuNP concentration is first determined by measuring the absorbance of the colloidal solution at 520 nm relative to their appropriate extinction coefficient supplied by the commercial provider (Ted Pella, Inc.). In order to determine the exact number of DNA hairpins per particle, the DNA is chemically displaced from the surface of the nanoparticle by addition of equal volumes of hAuNP solution and 1.0 M dithiothreitol (DTT) in 0.2 M phosphate buffer (PB), pH 8.3. Each solution is allowed to incubate for 12 hours at RT followed by centrifugation at 21,100 x g for 1 hr to remove the aggregated gold particles from solution. The resulting solution of displaced DNA is subjected to fluorescence spectroscopy and the concentration of hDNA is determined by a standard addition curve.

Fluorophore-proximal base

Hairpin DNA (hDNA) used for coupling to the AuNP surface was synthesized with the following sequences: MMP26scram_CCy5, 5'-(SH)-TTT TTT TTT TGC AGC **GTT ATC TTA CTC GTT CGA CAG** TGC TGC-(Cy5)-3' and MMP26scram_GCy5, 5'-(SH)-TTT TTT TTT TCG AGC **GTT ATC TTA CTC GTT CGA CAG** TGC TCG-(Cy5)-3'. Bolded regions indicate the region encoding specifically for the target mRNA, and regions in parentheses indicate the modifications of 5' thiol and 3' fluorophore conjugations. The sequences used for evaluation of hAuNP hybridization were: MMP26scramcomp, 5'-TTA CTG TCG AAC GAG TAA GAT AAC TT-3' and MMP26comp, 5'-TTT GCA AGT GGA ATA AGC ACA CTA TT-3'. A spacing ligand for coupling to the AuNP surface was T10, 5'-(SH)-TTT TTT TTT T-3'.

DNA concentration was verified by UV absorbance at 260 nm. Prior to coupling of hairpin DNA to AuNPs, lyophilized DNA was resuspended in 100 mM DTT and 0.1 mM phosphate buffer (pH = 8.3) and incubated for one hour at room temperature (RT) to reduce residual 5' disulfide bonds. A solution of 1 nM 15 nm AuNPs was prepared in nuclease-free water and brought to 0.1% Tween-20. T10 DNA was added to the solution to make 100 nM T10 DNA and incubated for overnight at RT while protected from light. hDNA was added to the solution to give 300 nM hDNA and incubated for 24 h. The solution was buffered to 10 mM phosphate buffer (pH 7.0) and brought to 0.1 M NaCl. The hAuNPs were then

incubated for an additional 4 h at RT. The NaCl concentration was adjusted to 0.2 M and the hAuNPs were incubated for an additional 4 h at RT. Finally, the NaCl concentration was adjusted to 0.3 M and incubated for a final 4 h at RT. The solution was then centrifuged at 21,100 g for 20 min and the hAuNPs were resuspended in PBS. The process of centrifugation and resuspension was repeated two more times.

hAuNP concentration was measured by absorbance at 520 nm, using the extinction coefficient for 15 nm AuNP $\varepsilon_{520} = 3.64 \times 10^8\ M^{-1}\ cm^{-1}$. To determine the effect of the proximal base on the fluorophore emission, 0.1 μM complementary (MMP26scramcomp) or mismatch (MMP26comp) target DNA was added to 0.1 nM hAuNP solutions in either PBS or complete media, incubated at 37 °C for 1 h, then measured for fluorescence emission intensity over time using a BioTek microplate reader.

Hairpin Design

Target mRNA sequences were input in the RNAstructure program as a "New Sequences" and were folded as RNA. Following folding, the RNA sequence was scanned for regions to which various-length oligonucleotides are capable of binding through the RNA OligoWalk module. Detailed instructions on generating these files are given in Appendix A.

The OligoWalk module generates an Excel table that lists the overall free energy of binding of every possible oligonucleotide while taking into account stability of the newly formed duplex, local secondary structure within the target

RNA, as well as intermolecular and intramolecular secondary structures formed by the oligonucleotide. Once the list is generated, sequences are evaluated on a set of characteristics that are necessary for ideal probe performance. It is important to avoid sequences with a stretch of more than three guanine or cytosine bases to avoid forming G-tetrads or G-quadruplexes. Sequences are also checked for cross homologies using the National Center for Biotechnology Information's Nucleotide Basic Local Alignment Search Tool (BLAST). Finally, potential probe sequences are evaluated using UNAfold (IDT) or a similar software tool. This program predicts the most stable secondary structure of an oligonucleotide by minimizing folding free energy, ensuring that the proper hairpin conformation will be adopted by the sequence.

Results and Discussion

AuNP quenching radius

To investigate the ideal particle size for hAuNPs, a range of commercially available gold colloids (2-50 nm diameter) were employed. The absorbance spectrum of each colloid solution was measured (Figure 4) and then the solutions were normalized so that the total surface area per volume was uniform.

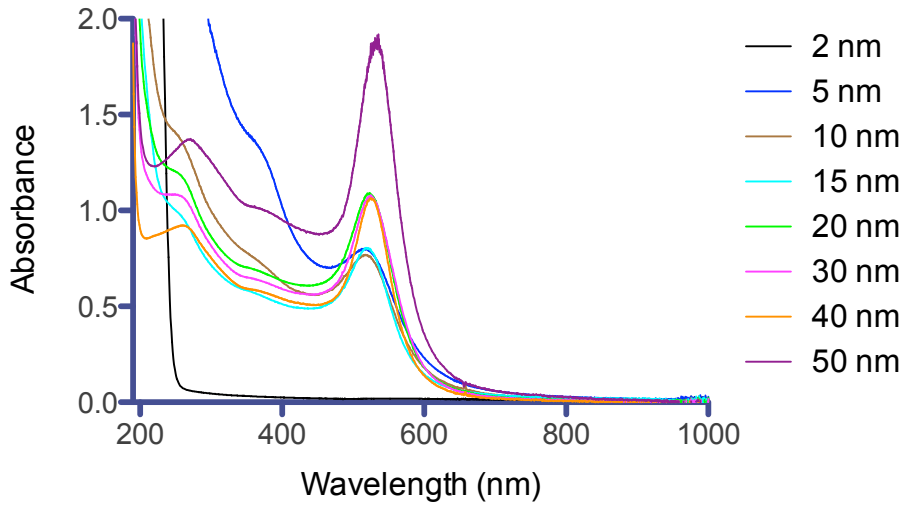

Figure 4. UV-Vis spectra of different sizes of gold nanospheres.

For every solution, equimolar amounts of 2, 5, 7, 10, and 15T sequences with a fluorophore on the 5' end were coordinated to the surface via a C6 thiol on the 3' end. The quenching radius was then examined by measuring the fluorescence of the AuNP/DNA solution. The results are shown in Figure 5. As expected, the closer the fluorophore is to the sphere's surface, the more efficiently the signal is quenched. Also of note, as the spheres decrease in size from 50 to 10 nm in diameter, the fluorescence signal is reduced. This phenomenon is most likely a result of the lightning rod effect in which there is a greater amount of localized electromagnetic fields at the corners and edges of the nanoparticles (4). While not possessing corners or edges, the smaller spheres still confine the surface electrons in a similar manner, increasing the localized electromagnetic field.

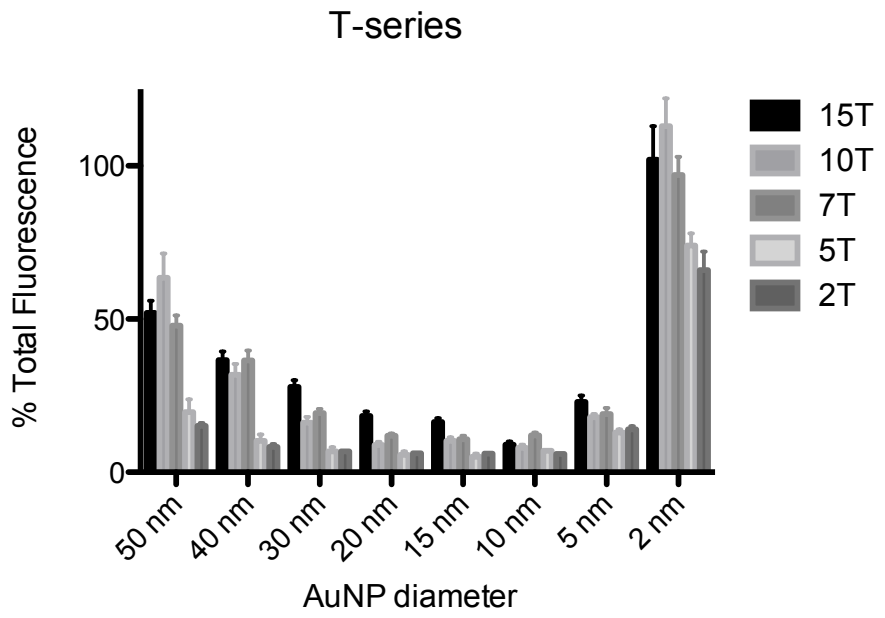

Figure 5. Percent of fluorescence quenched by Au nanospheres ranging from 2-50 nm in diameter as the fluorophore's proximity to the particle is varied.

Given this information, there could potentially be a small decrease in background fluorescence if 10 nm particles are utilized as the gold nanoparticle construct in hAuNPs as opposed to 15 nm. However, the advantage was deemed to not be significant enough to warrant a paradigm shift in research projects already underway (Chapters 3 & 4).

T10 spacing ligand

In order to investigate the surface coverage of the particle to ensure that the maximum number of hDNA strands bound with minimal steric interference between strands, we have incorporated a 10 thymine base sequence (T10) as a spacing ligand on the surface of the AuNPs. hDNA to T10 ratios of 1:0, 3:1, and

1:1 (0, 25, and 50% T10) were compared. The hAuNPs were introduced to complement and mismatch DNA in order to determine a signal-to-noise (S/N) ratio where the signal is the fluorescence units of the probe with complement DNA and noise is the value of the fluorescence units when nonspecific control DNA is added. The experiment was varied by incubating with complement up to temperatures of 85°C, 55°C, 37°C, and by keeping at room temperature. We have consistently achieved S/N ratios above 5 using 25% T10 ligand and by incubating with complement at 37°C.

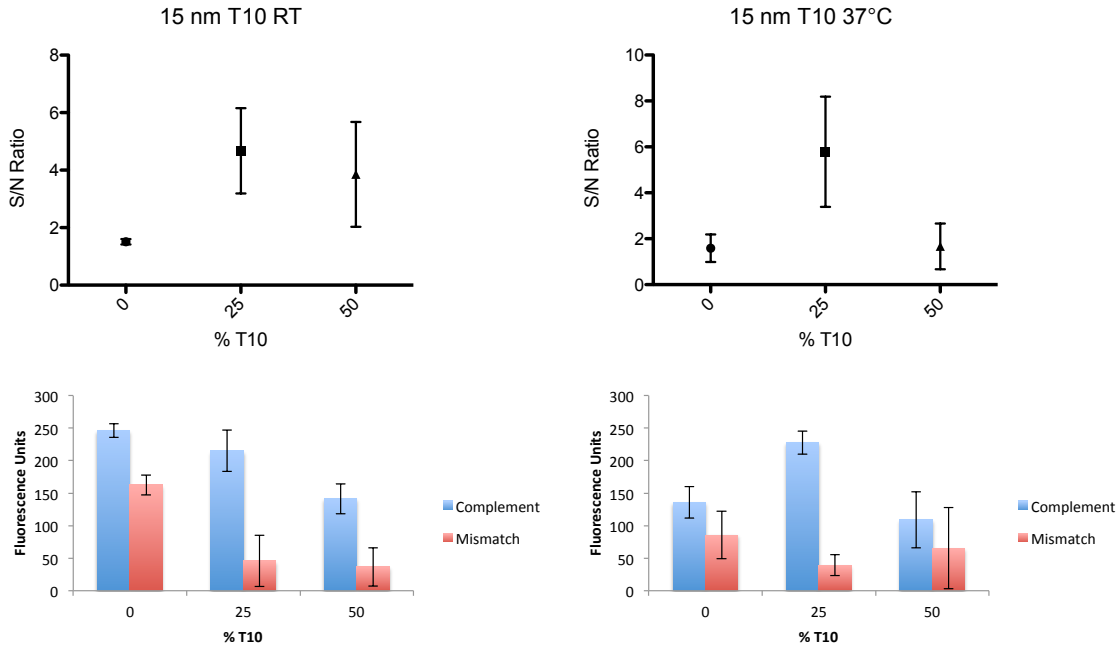

Figure 6. Signal-to-noise (S/N) ratios (top) of hAuNPs with varying surface concentrations of T10 DNA after incubating for 1 h at room temperature or 37 °C. Fluorescence data (bottom) shows total fluorescence signal used to generate S/N values.

The number of hDNA strands for hAuNPs with 0, 25, and 50% T10 have been calculated as 103 ± 2, 74 ±12, and 50 ± 1, respectively.

Fluorophore-proximal base

In multiple biophysical and biochemical applications of fluorescent oligonucleotides it was observed that the fluorescence of some conjugated dyes was sensitive to the environment around the point of attachment (5-11). In all of these cases it was proposed that the photoinduced charge transfer between the dye and a nucleotide residue plays a crucial role in the process. Most of the dyes studied were quenched by a guanine, which was explained by the good electron donating properties of this nucleotide (12,13).

To investigate the effects of fluorescence quenching by an adjacent guanosine nucleotide, a pair of fluorescently labeled oligonucleotides sharing the same core sequence but with differing proximal bases, one cytosine and one guanine were synthesized. The DNA sequences were conjugated to 15 nm spherical gold nanoparticles to give a solution of hAuNPs with all cytosine-proximal fluorophores and a separate hAuNP solution with all guanine-proximal fluorophores. The hAuNP solutions were evaluated by incubating with 0.1 μM complementary or mismatch target DNA. The target DNA was added to 0.1 nM hAuNP solutions in either PBS or complete media, incubated at 37 °C for 1 h, then measured for fluorescence emission intensity. In both PBS and in complete media backgrounds, the guanine-proximal hAuNPs showed a higher overall fluorescent signal upon complement binding, yet a comparable signal for the negative controls. This result is contrary to established reports; however, most of these reports discuss the quenching of fluorophores with an excitation

wavelength between 500 and 550 nm. The fluorophore used in this study was Cy5, which has a longer excitation wavelength (~650 nm).

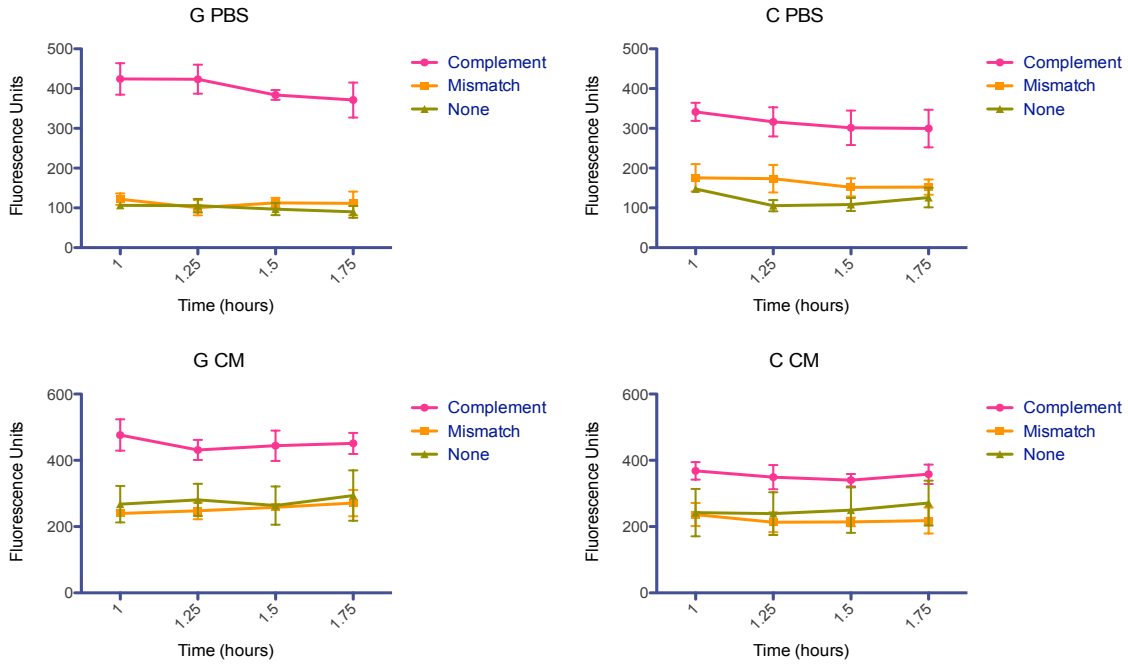

Figure 7. Fluorescence spectrophotometry studies showed a higher fluorescent output when the nucleotide conjugated to the fluorophore was a guanine residue as opposed to a cytosine. Measurements were taken in both phosphate buffered saline (PBS) and complete media (CM).

Conclusions

In summary, the information in this Chapter outlines (1) the experimental quenching radius for a range of Au nanospheres, (2) the number of DNA hairpins that will conjugate to a 15 nm AuNP before steric interference effects are observed, (3) evaluation of the effect that the fluorophore-proximal base has on hAuNP fluorescence, and (4) a protocol for recognition loop design selection that considers, among other parameters, the secondary structure of the target mRNA. Based on the results of these experiments and protocols, we have allowed for

the design of a more effective mRNA probe and thus expanded the potential biological applications of hAuNPs.

References

1. Jayagopal, A., Halfpenny, K.C., Perez, J.W. and Wright, D.W. (2010) Hairpin DNA-functionalized gold colloids for the imaging of mRNA in live cells. *J Am Chem Soc*, **132**, 9789-9796.

2. Harry, S.R., Hicks, D.J., Amiri, K.I. and Wright, D.W. (2010) Hairpin DNA coated gold nanoparticles as intracellular mRNA probes for the detection of tyrosinase gene expression in melanoma cells. *Chem Commun (Camb)*, **46**, 5557-5559.

3. El-Sayed, M.A. (2001) Some interesting properties of metals confined in time and nanometer space of different shapes. *Accounts of Chemical Research*, **34**, 257-264.

4. Orendorff, C.J., Gole, A., Sau, T.K. and Murphy, C.J. (2005) Surface-enhanced Raman spectroscopy of self-assembled monolayers: sandwich architecture and nanoparticle shape dependence. *Anal Chem*, **77**, 3261-3266.

5. Cardullo, R.A., Agrawal, S., Flores, C., Zamecnik, P.C. and Wolf, D.E. (1988) Detection of nucleic acid hybridization by nonradiative fluorescence resonance energy transfer. *Proc Natl Acad Sci U S A*, **85**, 8790-8794.

6. Murchie, A.I., Clegg, R.M., von Kitzing, E., Duckett, D.R., Diekmann, S. and Lilley, D.M. (1989) Fluorescence energy transfer shows that the four-way DNA junction is a right-handed cross of antiparallel molecules. *Nature*, **341**, 763-766.

7. Cooper, J.P. and Hagerman, P.J. (1990) Analysis of fluorescence energy transfer in duplex and branched DNA molecules. *Biochemistry*, **29**, 9261-9268.

8. Clegg, R.M., Murchie, A.I., Zechel, A., Carlberg, C., Diekmann, S. and Lilley, D.M. (1992) Fluorescence resonance energy transfer analysis of the structure of the four-way DNA junction. *Biochemistry*, **31**, 4846-4856.

9. Lee, S.P., Porter, D., Chirikjian, J.G., Knutson, J.R. and Han, M.K. (1994) A fluorometric assay for DNA cleavage reactions characterized with BamHI restriction endonuclease. *Anal Biochem*, **220**, 377-383.

10. Sauer, M., Drexhage, K.H., Lieberwirth, U., Muller, R., Nord, S. and Zander, C. (1998) Dynamics of the electron transfer reaction between an oxazine dye and DNA oligonucleotides monitored on the single-molecule level. *Chemical Physics Letters*, **284**, 153-163.

11. Walter, N.G. and Burke, J.M. (1997) Real-time monitoring of hairpin ribozyme kinetics through base-specific quenching of fluorescein-labeled substrates. *Rna-a Publication of the Rna Society*, **3**, 392-404.

12. Seidel, C.A.M., Schulz, A. and Sauer, M.H.M. (1996) Nucleobase-specific quenching of fluorescent dyes .1. Nucleobase one-electron redox potentials and their correlation with static and dynamic quenching efficiencies. *Journal of Physical Chemistry*, **100**, 5541-5553.

13. Steenken, S. and Jovanovic, S.V. (1997) How Easily Oxidizable Is DNA? One-Electron Reduction Potentials of Adenosine and Guanosine Radicals in Aqueous Solution. *Journal of the American Chemical Society*, **119**, 617-618.

CHAPTER III

HAIRPIN DNA-FUNCTIONALIZED GOLD NANOPARTICLES FOR THE IMAGING OF MATRIX METALLOPROTEINASE MRNA

In the era of personalized medicine for cancer therapy, there is an urgent need for techniques that are able to sensitively detect biomarkers and distinguish tumor-to-tumor heterogeneity. One of the defining characteristics of malignancy is the ability of cancer cells to metastasize and invade distant organ sites. Proteolysis of the extracellular matrix (ECM) is required to accommodate angiogenesis, invasion, and metastasis of tumor cells. The proteases responsible for degrading most of the components of the ECM are matrix metalloproteinases (MMPs), a family of more than 20 extracellular, zinc-dependent endopeptidases (1). In the tumor microenvironment, host and tumor derived MMPs are often misregulated leading to uncontrolled degradation of the ECM. For this reason, the profile of MMP expression is considered to be a potential biomarker for disease type, disease activity, and response to therapy. The recognition of the role of MMPs in tumor growth, migration, and invasion has guided the development of methods to detect and image tumors *in vivo* including magnetic resonance imaging (MRI) (2,3), single-photon emission computed tomography (SPECT) (4), and positron emission tomography (PET) (5); however, optical imaging has been the most intensively validated technique, particularly with fluorescent activatable probes (6,7).

Optical imaging is a non-invasive technique that uses light to probe tissue, making it less expensive than imaging modalities that require strong magnetic fields or radioactive traces to image tissues (8). Fluorogenically labeled substrates have been designed that are quenched due to the proximity of the fluorophores or that utilize Förster resonance energy transfer (FRET) to quench the fluorescent signal that is then enhanced upon proteolytic cleavage (9-11). Optical detection and imaging of *in vivo* protease activity was first demonstrated by Weissleder *et al.* in mouse xenograft tumors using a linear poly-lysine-polyethylene glycol copolymer with cleavable sequences carrying a near-infrared (NIR) fluorophore, Cy5.5 (12). Due to the proximity of the fluorophores, self-quenching prevented almost any detectable fluorescent signal in the nonactivated state. Upon proteolytic cleavage of the poly-lysine peptide linker, Cy5.5 molecules were released from the carrier, and a NIR fluorescence signal was optically detected. This construct was later modified to include a proteolytic beacon for MMP2 that was used to image HT-1080 human fibrosarcoma tumors in mice (13,14). In addition, the Tsien group has developed activatable cell penetrating peptides (ACPPs) containing a MMP recognition site (15,16). These ACPPs consist of a fluorophore-tagged cationic peptide covalently attached to a short stretch of acidic residues via a cleavable linker. The acidic residues prevent cellular uptake of the cationic peptide, but when the ACPPs reach tumor surfaces expressing MMPs, the linker on ACPPs is cleaved, releasing the acidic inhibitory domain, and the cationic peptides are free to carry the fluorophore into cells.

These types of activatable probes have become commercially available and are utilized by many research groups interested in imaging tumor-associated MMPs. However, the majority of these studies are based on proteolytic substrates, which are often cleaved by multiple MMPs, thus lacking the ability to assess and efficiently determine specific MMP activity. In addition, MMPs are inhibited by various means, including binding to tissue inhibitors of metalloproteinases (TIMPs) (17), which would give inconsistent results if measuring gene expression through proteolytic activity. To avoid these shortcomings, we will selectively evaluate single MMPs in a tumor microenvironment using an mRNA imaging probe that combines gold nanoparticles with molecular beacon-based technology. Hairpin DNA-functionalized gold nanoparticles (hAuNP) are constructed of a core gold nanoparticle with covalently attached DNA hairpin beacons via gold-thiol bond formation (18). Each DNA hairpin is constructed of a 5' hexane thiol linker covalently attached to a 10 thymine extension, followed by a ~30 base hairpin recognition sequence and a 3' fluorophore (Figure 8). The first and last five bases of the recognition sequence are complementary resulting in a five base duplex stem. While in the closed position, this construct utilizes the fluorescence quenching ability of the gold nanoparticle to quench the fluorescent signal. Within the cytoplasm, binding of the complementary mRNA sequence to the hairpin DNA causes the 3' fluorophore to extend beyond the quenching range of the gold nanoparticle resulting in emission of a fluorescent signal. hAuNPs improve upon currently used technologies for studying RNA trafficking due to

their efficient internalization within live cells without transfection reagents, improved resistance to DNAse degradation, low cytotoxicity, and high specificity and sensitivity toward the target mRNA sequence (18).

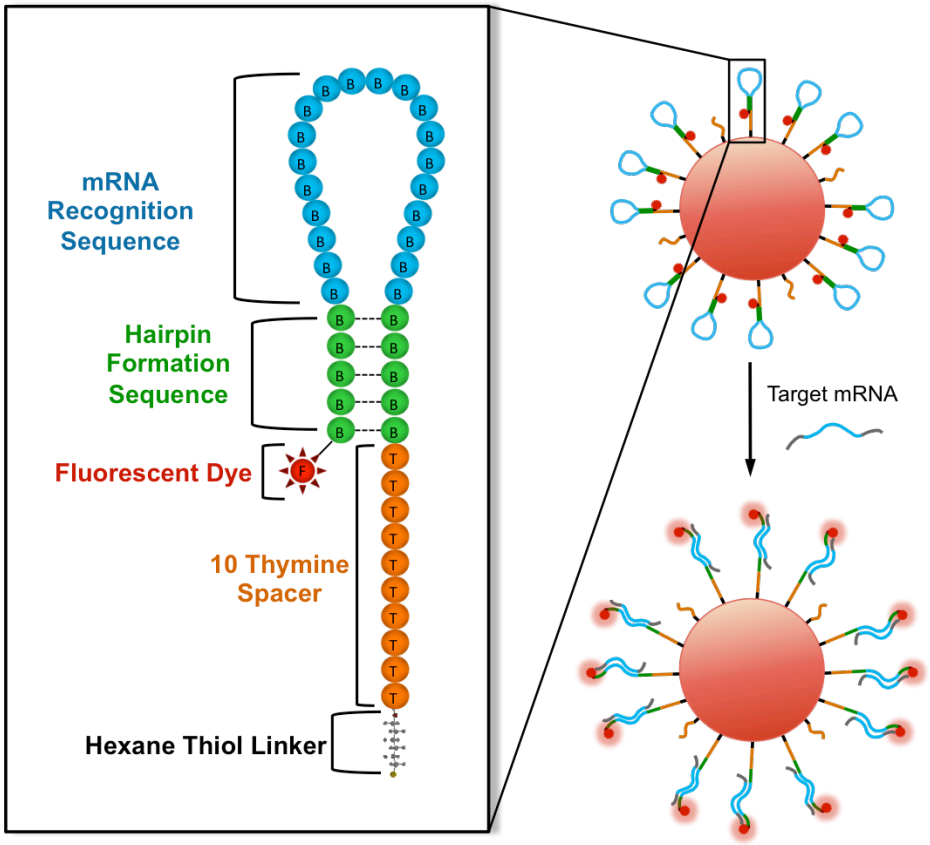

Figure 8. Hairpin DNA-functionalized gold nanoparticles (hAuNPs) for detection of mRNA in living cells.

In this study, we use hAuNPs to image the expression of three specific MMPs in three breast cancer cells of varying invasiveness. By using hAuNPs to target an mRNA sequence instead of utilizing a proteolytic substrate, we are able to assess the activity of specific MMPs. Furthermore, by simply altering the recognition sequence on the hairpin probe we enable the detection of three different MMPs. Finally, the observed expression of specific MMP mRNA using hAuNPs is compared to previously published levels of mRNA detected by RT-

PCR to validate the use of hAuNPs as qualitative mRNA expression probes in living cells. We believe this type of expression profile information for multiple MMPs in tumor and surrounding stromal cells may allow for generation of phenotypic “fingerprints” for different types of cancers and their invasiveness, ultimately leading to more effective personalized therapies.

Materials and Methods

The MDA-MB-231, MCF-7, and MCF-10A cell lines were provided as a gift by the Lynn Matrisian lab at Vanderbilt University. Oligonucleotides were synthesized by Sigma Life Science. High glucose DMEM media, 1% Penicillin-Streptomycin, and 0.25% Trypsin-EDTA were from Life Technologies. MEBM and MEGM were from Lonza. Chambered coverslip u-Slides were from ibidi. Gold nanoparticles were from Ted Pella, Inc. All other chemicals were purchased from Sigma-Aldrich.

Synthesis and Characterization of hAuNPs

Hairpin DNA (hDNA) used for coupling to the AuNP surface was synthesized with the following sequences: GAPDH, 5’-(SH)-TTT TTT TTT TGC ACG **AGG TTT TTC TAG ACG GCA GG**C GTG C-(TAMRA)-3’; MMP13, 5’-(SH)-TTT TTT TTT TGC AGC **TTG ACG CGA ACA ATA CGG TTA A**GC TGC-(Cy5)-3’; MMP14, 5’-(SH)-TTT TTT TTT TGC AGC **GCT CTT CTC CTC TTT TCC GGT TTT** GCT GC-(Cy5)-3’; MMP26, 5’-(SH)-TTT TTT TTT TGC AGC **TAG TGT GCT TAT TCC ACT TGC A**GC TGC-(Cy5)-3’; MMP26scram, 5’-(SH)-

TTT TTT TTT TGC AGC **GTT ATC TTA CTC GTT CGA CAG** TGC TGC-(Cy5)-3'. Bolded regions indicate sequences encoding specifically for target mRNAs, and regions in parentheses indicate modifications of 5' thiol and 3' fluorophore conjugations. Sequences for complementary targets for evaluation of hAuNP hybridization specificity were as follows: GAPDHcomp, 5'-TTC CTG CCG TCT AGA AAA ACC TTT-3'; MMP13comp, 5'-TTT TAA CCG TAT TGT TCG CGT CAA TT-3'; MMP14comp, 5'-TTA AAA CCG GAA AAG AGG AGA AGA GCT T-3'; MMP26comp, 5'-TTT GCA AGT GGA ATA AGC ACA CTA TT-3'; MMP26scramcomp, 5'-TTA CTG TCG AAC GAG TAA GAT AAC TT-3'. A spacing ligand for coupling to the AuNP surface was T10, 5'-(SH)-TTT TTT TTT T-3'.

DNA concentration was verified by UV absorbance at 260 nm. Prior to coupling of hairpin DNA to AuNPs, lyophilized DNA was resuspended in 100 mM DTT and 0.1 mM phosphate buffer (pH = 8.3) and incubated for one hour at room temperature (RT) to reduce residual 5' disulfide bonds. A solution of 1 nM 15 nm AuNPs was prepared in nuclease-free water and brought to 0.1% Tween-20. T10 DNA was added to the solution to make 100 nM T10 DNA and incubated for overnight at RT while protected from light. hDNA was added to the solution to give 300 nM hDNA and incubated for 24 h. The solution was buffered to 10 mM phosphate buffer (pH 7.0) and brought to 0.1 M NaCl. The hAuNPs were then incubated for an additional 4 h at RT. The NaCl concentration was adjusted to 0.2 M and the hAuNPs were incubated for an additional 4 h at RT. Finally, the NaCl concentration was adjusted to 0.3 M and incubated for a final 4 h at RT.

The solution was then centrifuged at 21,100 g for 20 min and the hAuNPs were resuspended in PBS. The process of centrifugation and resuspension was repeated two more times.

hAuNP concentration was measured by absorbance at 520 nm, using the extinction coefficient for 15 nm AuNP $\varepsilon_{520} = 3.64 \times 10^8\ M^{-1}\ cm^{-1}$. To determine sensitivity and specificity of hAuNPs to synthetic targets, increasing concentrations of complementary or mismatch target DNA were added to 1 nM hAuNP solutions in PBS and measured for fluorescence emission intensity using a BioTek microplate reader. For measurement of hydrodynamic diameter, 0.1 nM solutions of AuNPs or hAuNPs were resuspended in nuclease-free PBS and measured using dynamic light scattering (DLS) on a Malvern Nano ZS.

Cell Culture

All cells were cultured as monolayers in a humidified atmosphere of 95% air and 5% CO_2 at 37 °C. MCF-7 and MDA-MB-231 cells were maintained in high glucose DMEM with L-glutamine supplemented with 10% FBS and 1% Pen/Strep. MCF-10A cells were maintained in MEBM supplemented with 100 ng/mL cholera toxin and Lonza CC-4136 but with 1% final penicillin/streptomycin rather than the supplied GA-1000 aliquot.

Flow Cytometric Analysis

For each experiment, cells at 80-90% confluence were incubated with 0.5 nM hAuNPs for 4 h, rinsed three times with Ca^{2+} and Mg^{2+} free DPBS to remove

unbound and uninternalized hAuNPs, and detached using trypsin. Cells were assayed using a BD LSRFortessa cell analyzer. All experiments consisted of ≥ 10,000 events.

Confocal Microscopy

Twelve hours prior to the addition of hAuNPs, chambered coverslip µ-Slides from ibidi were prepared. This was done by lifting a culture of each cell type with 0.25% trypsin-EDTA then plating onto the collagen-IV coated slides in their respective media from above and placed in an incubator at 37 °C until the addition of hAuNPs. At the time of particle addition, each well was approximately 10% confluent. hAuNPs were added to make 0.5 nM total hAuNPs in solution. After 4 hours, the media and suspended hAuNPs were aspirated away, and the chambered slides were washed 3x with Ca^{2+} and Mg^{2+} free DPBS. After the final wash, all cells were kept in phenol red free, high glucose DMEM supplemented with 10% FBS while being imaged.

Results and Discussion

Selection of Probe Sequence

In order to evaluate the effectiveness of hAuNPs as qualitative mRNA expression probes, we chose three individual MMP mRNAs to target: MMP13, MMP14, and MMP26. The majority of studies in the literature suggest that by choosing these three MMPs, we will have high (MMP14), moderate (MMP13),

and little-or-no (MMP26) expression targets in invasive breast cancer cells. We chose to use the housekeeping gene glyceraldehyde 3-phosphate dehydrogenase (GAPDH) as the target for a positive control probe. DNA hairpins with a scrambled version of the MMP26 recognition loop were used to create negative control hAuNPs.

Theoretically, any sequence within a target mRNA can be chosen as a site for recognition loop binding. The most straightforward approach for probe sequence selection is to search the literature for priming sites used successfully in quantitative reverse transcription PCR (qRT-PCR) of the biomarker of interest. However, target accessibility is primarily a consequence of complex secondary and tertiary intramolecular structures, which are not easy to predict and can mask many regions used for primer binding. To help predict sites readily available for binding, we have employed RNAstructure, a program available from the Mathews Lab at the University of Rochester Medical Center, to predict the folding of the target mRNA sequence. After the sequence is folded, a section of 18-25 bases is chosen from an easily accessible region. Using public databases and sequence comparison tools, it is confirmed that the chose probe sequence is unique to the target biomarker and has little or no homology with other cellular RNA sequences. The full probe sequences we selected for this study are given in the Methods section.

Synthesis and Characterization of hAuNPs

AuNPs heavily loaded with DNA strands possess strong interparticle electrostatic repulsion which protects the AuNPs from aggregating in salt solution. However, heavily loading the particle with hairpin DNA (hDNA) causes steric interference between hairpins, inhibiting a complementary sequence from binding to a hairpin or preventing a hairpin from properly opening after binding. To remedy this effect, we employed the use of spacing ligands composed of ten sequential thymine bases with a hexane-thiol linker at the 5' end. Indeed, hAuNPs synthesized with a 3:1 ratio of hairpins:spacing ligands provided the highest fluorescence intensity in response to excess complement (Figure 6, Chapter 2).

The number of hairpins loaded on each particle was determined by subjecting a 10 nM solution of hAuNPs to dithiothreitol reduction to reduce the Au-thiol bonds and precipitate the gold particles, then measuring fluorescence and absorbance values of the DNA-containing supernatant and comparing to standard curves. The oligonucleotide-to-particle ratio for all hAuNPs synthesized in this study was determined to be approximately 68 hairpins and 23 T10 ligands per particle.

UV-visible absorbance spectra of hAuNP exhibited absorbance peaks at nucleic acid- and AuNP-specific peaks of 260 and 520 nm, respectively. Fluorescence spectrophotometry studies confirmed that hAuNPs were specific for target sequences, with emission of fluorescence consistent with the fluorophore coupled to the 3' end of the hDNA (Figure 9A). hAuNPs exhibited

dose-specific increases in fluorescence intensity in response to complement concentration and did not react to an appreciable level when incubated with an equal concentration of mismatched DNA (Figure 9A). DLS analyses indicated an increase in hydrodynamic diameter of 15-16 nm when hDNA was coupled to citrate-capped AuNP (Figure 9B). When introduced to a specific target, the hairpin opening resulted in a hydrodynamic diameter increase of 6-7 nm while the presence of a nonspecific target showed no change.

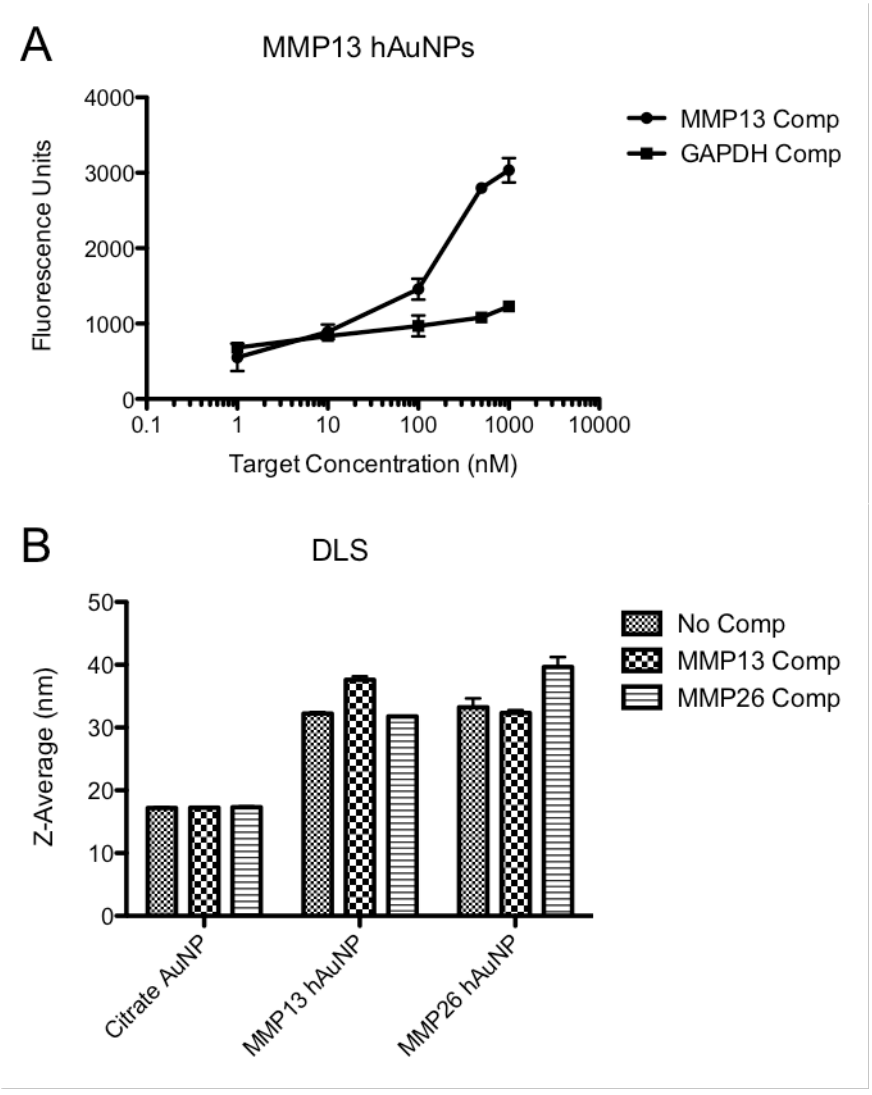

Figure 9. Characterization data from MMP13 hAuNPs. (A) Fluorescence spectrophotometry studies showed an increase in fluorescent signal due to opening of hairpins when hAuNPs were incubated with their

respective complement as opposed to a noncomplementary sequence. (B) Dynamic light scattering studies on hAuNPs showed an increase in hydrodynamic diameter of 15-16 nm when hDNA was coupled to citrate-capped AuNP and an increase of 6-7 nm when hAuNPs are introduced to a specific target.

Flow Cytometry

To evaluate gene expression, three different cell lines that express MMPs at varying levels were used: MCF-10A, a non-tumorigenic epithelial cell line, MCF-7, a poorly invasive breast ductal carcinoma *in situ*, and MDA-MB-231, a highly-malignant invasive ductal carcinoma. The cells were incubated with 0.5 nM hAuNPs and analyzed by flow cytometry (Figure 10). MDA-MB-231 cells showed the highest expression of all three MMPs examined, followed by MCF-7 and MCF-10A cells. A scrambled sequence of MMP26, MMP26scram, served as a nonspecific, negative control probe. MMP26scram had relatively consistent intensities among cell lines. This is important to note in that it assures that the changes of intensities of the same probe between cell lines are due to differences in mRNA expression and not due to differing rates of hAuNP uptake. These results mirror published expression profiles given for these targets using RT-PCR as shown in Figure 10.

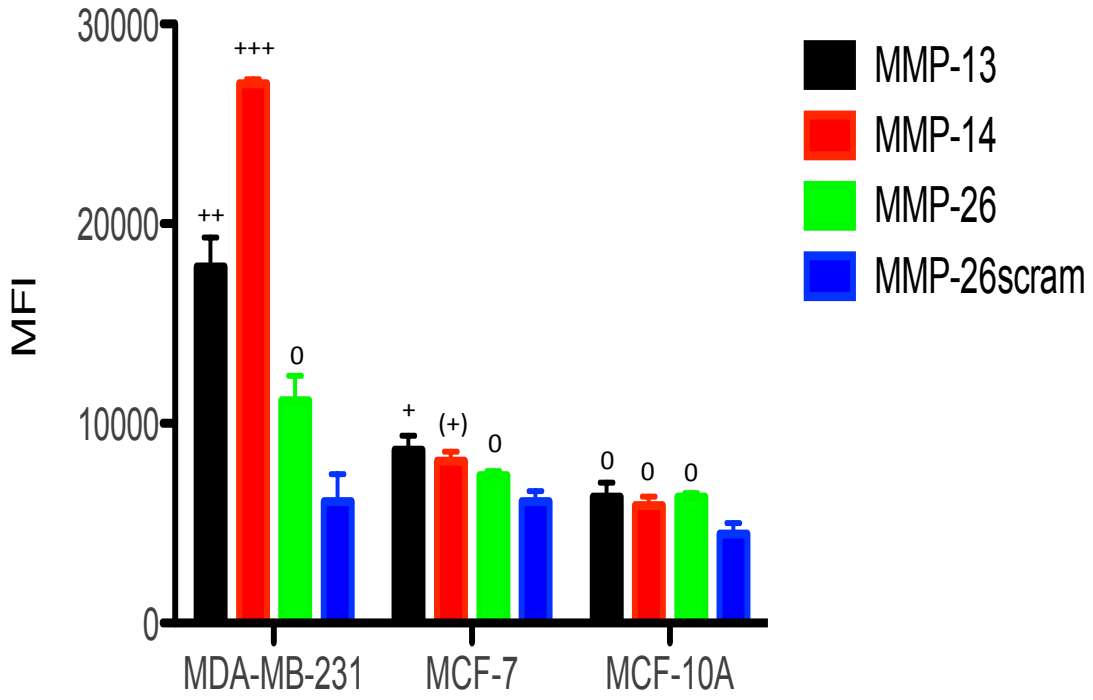

Figure 10. Flow cytometry analysis of the gene expression of select MMPs in cells as measured by hAuNPs. The symbols above the columns refer to relative expression of MMP mRNA determined by RT-PCR from previously published studies (19,20). 0 = no expression, (+) = very weak expression, + = weak expression, ++ = moderate expression, +++ = high expression.

Confocal Microscopy

Confocal microscopy studies were performed for each cell line and probe combination. Representative results are shown in Figures 11 and 12. Figure 11 shows the three cell lines treated with both MMP-14 and GAPDH hAuNPs. Emission from MMP14-specific hAuNPs is greatest in MDA-MB-231 cells, followed by MCF-7 and MCF-10A, consistent with the flow cytometric analysis. The hAuNPs are distributed throughout the cytosol but are not found within the

Syto13 stained nulecus. Figure 12 shows the expression of all hAuNPs in MDA-MB-231 cells. Again, the images reflect the results seen in the flow cytometric analysis, with the greatest signal from MMP14 hAuNPs, followed by MMP13, MMP26, and the negative control, MMP26scram.

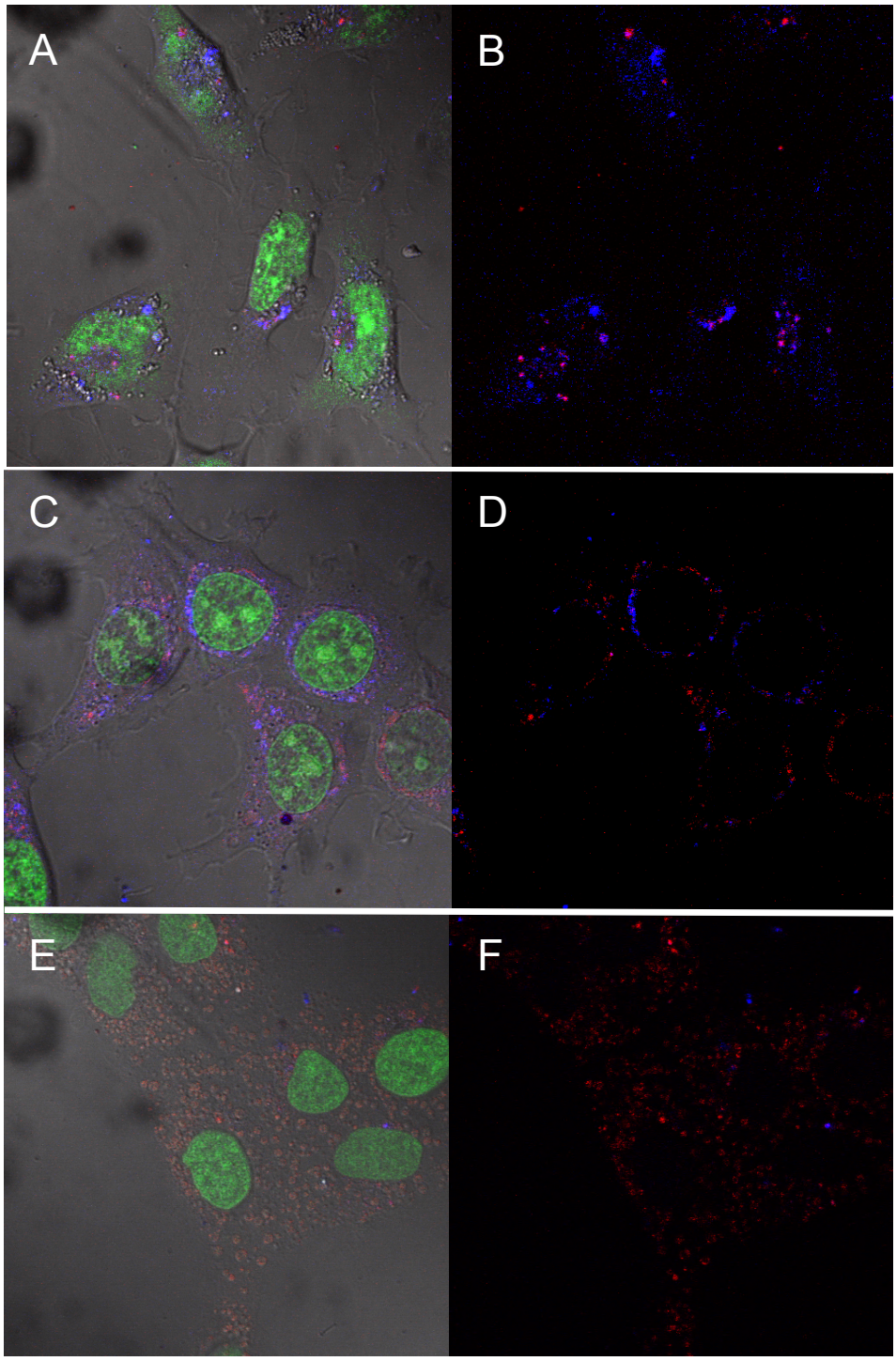

Figure 11. Intracellular uptake and fluorescence emission of hAuNPs across cell lines. MMP14-specific hAuNP emission (blue) decrease from MDA-MB-231 cells (A & B) to MCF-7 (C & D) to MCF-10A (E & F). Red fluorescence is GAPDH-specific hAuNP. Green is Syto13 nuclear counterstain. 100x magnification.

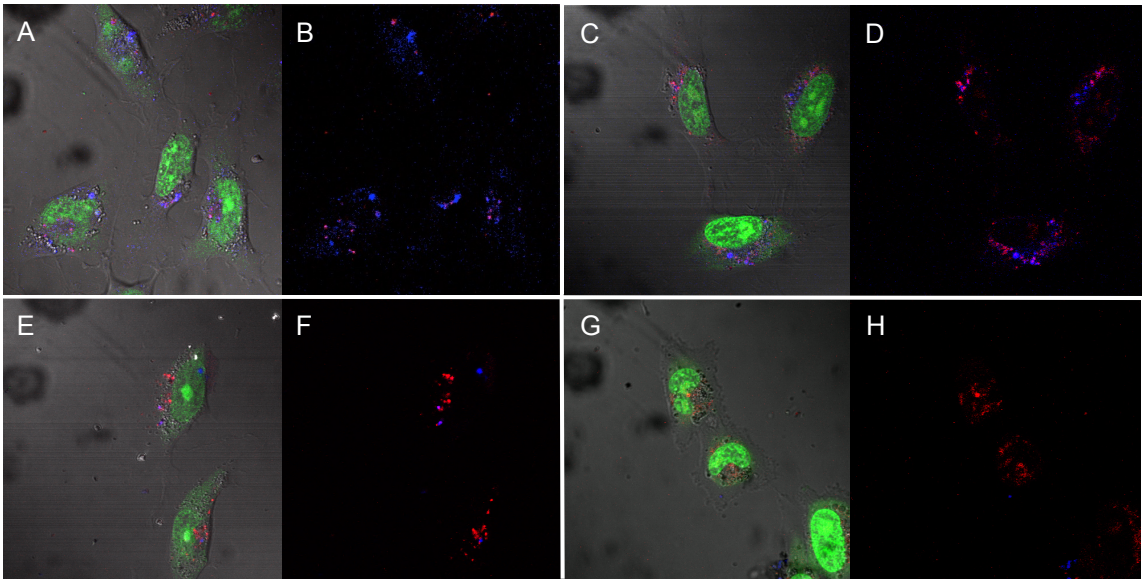

Figure 12. Comparison of MMP hAuNP activation in MDA-MB-231 cells. Blue fluorescence is specific for MMP-14 (A & B), MMP-13 (C & D), MMP-26 (E & F), and the negative control MMP-26scram (G & H). Red fluorescence is GAPDH-specific hAuNP. Green is Syto13 nuclear counterstain. 100x magnification.

Conclusions

In summary, we have successfully demonstrated that hAuNPs can be used to image multiple biomarkers in three different types of living cancer cells. The fluorescence intensities for these probes in cells were measured by flow cytometry and confocal microscopy and showed good agreement with reported RT-PCR values for their target mRNA expression, thus confirming the ability to measure relative expression levels of mRNAs in living cells using hAuNPs. This readout can be applied to profile the invasiveness of single cells or tissues from clinical samples and also serve as an indicator for screening anti-cancer inhibitors. A similar strategy utilizing hAuNPs can be applied to many other systems in which modular detection of multiple mRNAs is advantageous.

References

1. Sternlicht, M.D. and Werb, Z. (2001) How matrix metalloproteinases regulate cell behavior. *Annu Rev Cell Dev Biol*, **17**, 463-516.

2. Lepage, M., Dow, W.C., Melchior, M., You, Y., Fingleton, B., Quarles, C.C., Pepin, C., Gore, J.C., Matrisian, L.M. and McIntyre, J.O. (2007) Noninvasive detection of matrix metalloproteinase activity in vivo using a novel magnetic resonance imaging contrast agent with a solubility switch. *Molecular Imaging*, **6**, 393-403.

3. Schellenberger, E., Rudloff, F., Warmuth, C., Taupitz, M., Hamm, B. and Schnorr, J. (2008) Protease-specific nanosensors for magnetic resonance imaging. *Bioconjug Chem*, **19**, 2440-2445.

4. Medina, O.P., Kairemo, K., Valtanen, H., Kangasniemi, A., Kaukinen, S., Ahonen, I., Permi, P., Annila, A., Sneck, M., Holopainen, J.M. *et al.* (2005) Radionuclide imaging of tumor xenografts in mice using a gelatinase-targeting peptide. *Anticancer Research*, **25**, 33-42.

5. Sprague, J.E., Li, W.P., Liang, K., Achilefu, S. and Anderson, C.J. (2006) In vitro and in vivo investigation of matrix metalloproteinase expression in metastatic tumor models. *Nucl Med Biol*, **33**, 227-237.

6. Zhu, L., Niu, G., Fang, X. and Chen, X. (2010) Preclinical molecular imaging of tumor angiogenesis. *Q J Nucl Med Mol Imaging*, **54**, 291-308.

7. Yang, Y., Hong, H., Zhang, Y. and Cai, W. (2009) Molecular Imaging of Proteases in Cancer. *Cancer Growth Metastasis*, **2**, 13-27.

8. Weissleder, R. and Pittet, M.J. (2008) Imaging in the era of molecular oncology. *Nature*, **452**, 580-589.

9. McIntyre, J.O., Fingleton, B., Wells, K.S., Piston, D.W., Lynch, C.C., Gautam, S. and Matrisian, L.M. (2004) Development of a novel fluorogenic proteolytic beacon for in vivo detection and imaging of tumour-associated matrix metalloproteinase-7 activity. *Biochem J*, **377**, 617-628.

10. McIntyre, J.O. and Matrisian, L.M. (2003) Molecular imaging of proteolytic activity in cancer. *J Cell Biochem*, **90**, 1087-1097.

11. Tsien, R.Y. (2005) Building and breeding molecules to spy on cells and tumors. *FEBS Lett*, **579**, 927-932.

12. Weissleder, R., Tung, C.H., Mahmood, U. and Bogdanov, A., Jr. (1999) In vivo imaging of tumors with protease-activated near-infrared fluorescent probes. *Nat Biotechnol*, **17**, 375-378.

13. Bremer, C., Bredow, S., Mahmood, U., Weissleder, R. and Tung, C.H. (2001) Optical imaging of matrix metalloproteinase-2 activity in tumors: feasibility study in a mouse model. *Radiology*, **221**, 523-529.

14. Bremer, C., Tung, C.H. and Weissleder, R. (2001) In vivo molecular target assessment of matrix metalloproteinase inhibition. *Nat Med*, **7**, 743-748.

15. Jiang, T., Olson, E.S., Nguyen, Q.T., Roy, M., Jennings, P.A. and Tsien, R.Y. (2004) Tumor imaging by means of proteolytic activation of cell-penetrating peptides. *Proc Natl Acad Sci U S A*, **101**, 17867-17872.

16. Olson, E.S., Aguilera, T.A., Jiang, T., Ellies, L.G., Nguyen, Q.T., Wong, E.H., Gross, L.A. and Tsien, R.Y. (2009) In vivo characterization of activatable cell penetrating peptides for targeting protease activity in cancer. *Integr Biol (Camb)*, **1**, 382-393.

17. Brew, K., Dinakarpandian, D. and Nagase, H. (2000) Tissue inhibitors of metalloproteinases: evolution, structure and function. *Biochim Biophys Acta*, **1477**, 267-283.

18. Jayagopal, A., Halfpenny, K.C., Perez, J.W. and Wright, D.W. (2010) Hairpin DNA-functionalized gold colloids for the imaging of mRNA in live cells. *J Am Chem Soc*, **132**, 9789-9796.

19. Kohrmann, A., Kammerer, U., Kapp, M., Dietl, J. and Anacker, J. (2009) Expression of matrix metalloproteinases (MMPs) in primary human breast cancer and breast cancer cell lines: New findings and review of the literature. *BMC Cancer*, **9**, 188.

20. Hegedus, L., Cho, H., Xie, X. and Eliceiri, G.L. (2008) Additional MDA-MB-231 breast cancer cell matrix metalloproteinases promote invasiveness. *J Cell Physiol*, **216**, 480-485.

CHAPTER IV

IMAGING BIOMARKERS OF RETINAL VASCULAR DISEASE IN VIVO USING HAIRPIN DNA-GOLD NANOPARTICLES

Molecular imaging strategies for early detection of retinal vascular diseases are needed for improving clinical diagnosis, timeliness of therapeutic intervention, and assessment of therapeutic response. Approaches for molecular imaging of the retina have been limited by a lack of molecularly targeted imaging agents capable of targeting disease biomarkers *in vivo* with sufficient sensitivity and safety. In this study, we will use hairpin DNA-functionalized gold nanoparticles (hAuNPs) featuring optical contrast agents and RNA-specific nucleic acid targeting sequences to noninvasively image three retinal vascular disease biomarkers: hypoxia-inducible factor-1 alpha subunit (HIF-1α), vascular endothelial growth factor 2 (VEGFR2), and vascular cell adhesion protein 1 (VCAM1).

Age-related macular degeneration (AMD) is the leading cause of vision loss in humans fifty and older in developed countries, and choroidal neovascularization (CNV) is the most common cause of severe vision loss in age-related macular degeneration. CNV is responsible for substantial vision loss in pathologic myopia, presumed ocular histoplasmosis syndrome, angioid streaks, and idiopathic polypoidal choroidal vasculopathy (1). In all of these conditions, CNV results from the growth of new blood vessels into the subretinal

space through a break in Bruch's membrane, the innermost layer of the choroid. Recent studies have agreed that this growth is characterized by a stereotypical tissue repair response at the cellular level, including fibrin deposition with provisional matrix formation, inflammation, neovascularization, extracellular matrix deposition and remodeling (disciform scar formation) (2-4). Pivotal in the neovascular response is the production of VEGF (5). It is suggested that anti-angiogenesis therapy may be beneficial in the treatment of CNV. Several novel therapies for CNV have emerged based on antagonism of EGF or the VEGF receptor, such as intravitreal administration of bevacizumab (Avastin), ranibizumab (Lucentis) and pegaptanib (Macugen) (6-8). However, a potential drawback of these therapies is that there has been some evidence showing that suppressed expression of VEGF alone is not sufficient to inhibit CNV (9-11).

The initiation of a submacular wound-healing response may require a hypoxic stimulus, which in turn leads to the production of HIF-1, a transcription factor that functions as a master regulator of oxygen homeostasis (12). Clinical studies have shown that the age-related changes in Bruch's membrane and the dropout of choriocapillaris cause impaired diffusion of oxygen (13,14). Outer retina hypoxia and the resulting transcriptional activation of the HIF-1 may become an important driving force of CNV formation by stimulating VEGF overexpression, in addition to the effects of increased oxidative stress and low-grade inflammation (15-19). Recently, it has also been shown that CNV membranes are positive for HIF-1 expression, and this expression tends to be localized to the retinal pigment epithelium (RPE) cells. As a 'master switch' for

mammalian circulation in response to low oxygen tension, HIF-1 regulates the transcription of many proangiogenic growth factors, inducing VEGF, erythropoietin and platelet-derived growth factor. Knocking down of HIF-1α gene results in the down regulation of VEGF. Moreover, RPE cells senescence and hypoxia may decrease expression of angiogenesis inhibitors such as pigmentepithelium-derived factor (PEDF), further shifting the balance to a pro-angiogenic state in the aging eye. Thus, much attention has been drawn to this master modulator, because it may not only down-regulate the VEGF expression, but may also adjust some other uncertain factors to achieve a synergistic effect.

To address the need for clinically-relevant retinal molecular imaging agents, hairpin DNA functionalized gold nanoparticles (hAuNP) featuring optical contrast agents and RNA-specific nucleic acid targeting sequences were developed to noninvasively image messenger RNA biomarker in the retina. The goal of this study was to evaluate the utility of hAuNP for longitudinal imaging of mRNA biomarkers in an animal model of laser-induced choroidal neovascularization (LCNV), with the long-term goal of developing imaging agents for clinical detection of subclinical and advanced CNV. This animal model is widely employed to model pathologic angiogenesis of the type that occurs in neovascular age-related macular degeneration.

Materials and Methods

Stellaris FISH mRNA probes and hairpin oligonucleotides were purchased from Biosearch Technologies. Gold nanoparticles were from Ted Pella, Inc.

FITC-conjugated isolectin B4 was purchased from Sigma. Mice were C57BL6/J mice 6-8 wk old females from Jackson Laboratories. In vivo retinal imaging was performed using a Phoenix Research Labs Micron III retinal imaging microscope. 10% AK-Fluor (sodium fluorescein) was from Akorn Inc.

Synthesis and Characterization of hAuNPs

Hairpin DNA (hDNA) used for coupling to the AuNP surface was synthesized with the following sequences: HIF1α, 5'-(SH)-TTT TTT TTT TCC GGT **ATT GTC CTT CGT CTC TGT TTT TG**A CCG G-(Cy5)-3'; BetaActin, 5'-(SH)-TTT TTT TTT TCG ACG **GTC GTC CTA CAC CTA GTC GTT CGT CCT CA**C GTC G-(Cy3)-3'; VEGFR2, 5'-(SH)-TTT TTT TTT TCG AGC **TCT CAA TCG GAC GGC AGT AGC** GCT CG-(Cy5)-3'; VCAM1, 5'-(SH)-TTT TTT TTT TGC AGC **GTT TGC GTA CTC TGC CTT TGT TTG** GCT GC-(Cy5)-3'; HIF1αscram, 5'-(SH)-TTT TTT TTT TCC GGT **TTA GTT CCT GTT CTG TTG TCT TC**A CCG G-(Cy5)-3'; VEGFR2scram, 5'-(SH)-TTT TTT TTT TCG AGC **TCT CAA TCG GAC GGC AGT AGC** GCT CG -(Cy5)-3'. Bolded regions indicate sequences encoding specifically for target mRNAs, and regions in parentheses indicate modifications of 5' thiol and 3' fluorophore conjugations. Sequences for complementary targets for evaluation of hAuNP hybridization specificity were as follows: HIF1αcomp, 5'-TTC AAA AAC AGA GAC GAA GGA CAA TTT-3'; BetaActincomp, 5'-TTT GAG GAC GAA CGA CTA GGT GTA GGA CGA CTT-3'; VEGFR2comp, 5'-TTG CTA CTG CCG TCC GAT TGA GAT T-3'; VCAM1comp, 5'-TTC AAA CAA AGG CAG AGT ACG CAA ACT T-3';

HIF1αscramcomp, 5'-TTG AAG ACA ACA GAA CAG GAA CTA ATT-3'; VEGFR2scramcomp, 5'-TTG CTA CTG CCG TCC GAT TGA GAT T-3'. A spacing ligand for coupling to the AuNP surface was T10, 5'-(SH)-TTT TTT TTT T-3'.

DNA concentration was verified by UV absorbance at 260 nm. Prior to coupling of hairpin DNA to AuNP, lyophilized DNA was resuspended in 100 mM DTT and 0.1 mM phosphate buffer (pH = 8.3) and incubated for one hour at room temperature (RT) to reduce residual 5' disulfide bonds. A solution of 1 nM 15 nm AuNPs was prepared in nuclease-free water and brought to 0.1% Tween-20. T10 was added to the solution to make 100 nM T10 DNA and incubated for 4 h at RT while protected from light. After 4 h, hDNA was added to the solution to give 300 nM hDNA and incubated for an additional 4 h. The solution was then buffered to 10 mM phosphate buffer (pH 7.0) and brought to 0.1 M NaCl. The hAuNPs were then incubated for an additional 4 h at RT. The NaCl concentration was then adjusted to 0.2 M and the hAuNPs were incubated for an additional 4 h at RT. Finally, the NaCl concentration was adjusted to 0.3 M and incubated for a final 4 h at RT. The solution was then centrifuged at 21,100 g for 20 min and the hAuNPs were resuspended in PBS. The process of centrifugation and resuspension was repeated two more times.

hAuNP concentration was measured by absorbance at 520 nm, using the extinction coefficient for 15 nm AuNP $\varepsilon_{520} = 3.64 \times 10^8\ M^{-1}\ cm^{-1}$. To determine sensitivity and specificity of hAuNPs to synthetic targets, increasing concentrations of complementary DNA were added to 1 nM hAuNP solutions in

PBS and measured for fluorescence emission intensity using a SpectraMax M5 microplate reader (Molecular Devices). A AuNP functionalized with a 10 thymine spacer with an identical fluorophore on the 3' end was used to correct for intrinsic background fluorescence of the quenched hAuNP.

Ex vivo analyses

Human choroidal microvascular endothelial cells were conditioned under normoxic or hypoxic environments in a 37C 5% CO2 incubator. For hypoxic conditioning (<0.1% O2), cells were cultured in a Billups-Rothenberg chamber flushed for 5 min with 95% N2/5% CO2 mixture at a rate of 20 L/min. Hypoxia was confirmed using this system using RT-PCR analysis, which confirmed hypoxia-specific expression of HIF1 alpha mRNA. 1 nM hAuNP solutions were added to the growth medium and allowed to incubate for 2 hours. After incubation, cells were rinsed with HBSS using a plate washer (Biotek ELX405CW) and the fluorescence emission intensity was measured using a Biotek Synergy Mx microplate reader.

Choroid-RPE flatmounts were prepared as previously described and stained for isolectin B4 or ICAM-2 to label choroidal neovascular lesions as previously described. Flatmounts were also analyzed by fluorescence in situ hybridization (FISH) where indicated using Stellaris RNA FISH probes according to manufacturers instructions (Biosearch Technologies). Fluorescence imaging was conducted using a Nikon Ti-E Eclipse deconvolution inverted microscope.

CNV production in mice

The CNV was produced by administering laser radiation between the major retinal vessels of the fundus by following a previously published method (20-23). The animals were anesthetized with an IP injection of 80/12 mg/kg ketamine/xylazine (K113, Sigma), treated with proparacaine (0.5 %) drops for corneal anesthesia, and the pupils dilated with phenylephrine (2.5 %) and atropine sulfate (1 %) drops. A handheld coverslip and (2.5 %) Gonak solution (Akorn) were used as a contact lens for the maintenance of corneal clarity during photocoagulation. Animals were positioned before a slit lamp (Carl Zeiss Meditec, Inc.; Jena, Germany) laser delivery system. An argon green laser (Coherent, Palo Alto; CA, USA) was used for photocoagulation (532 nm wavelength; 360 mW power; 0.07 s duration; and 50 μm spot size). The laser beam was focused on Bruch's membrane with the intention of rupturing it, as evidenced by subretinal bubble formation without intraretinal or choroidal hemorrhage at the lesion site. Each lesion was made in the regions between the major vessels of the retina for a total of five lesions per eye concentrically applied approximately two optic discs from the center. The choroidal capillaries proliferated through the break in Bruch's membrane into the disrupted outer layers of the retina.

Sodium fluorescein was administered through 100 μL i.p. injection and allowed to circulate for 10 min prior to imaging.

Results and Discussion

hAuNPs designed to specifically target the CNV-relevant mRNA biomarkers HIF1α, VCAM-1, and VEGFR2 were evaluated using *in vitro* endothelial cell cultures and mouse models of LCNV. Nonspecific control hAuNP and hAuNP targeting housekeeping mRNA transcripts were utilized in parallel as negative controls and normalization of emission signal, respectively.

Before introducing the probes into an animal model, hAuNPs were evaluated for specificity to a synthetic complement. Fluorescence spectrophotometric quantification of targeted and scrambled hAuNPs mixed with complementary RNA reveals that targeted hAuNP, but not scrambled hAuNPs, are specific for their mRNA targets (Figure 13).

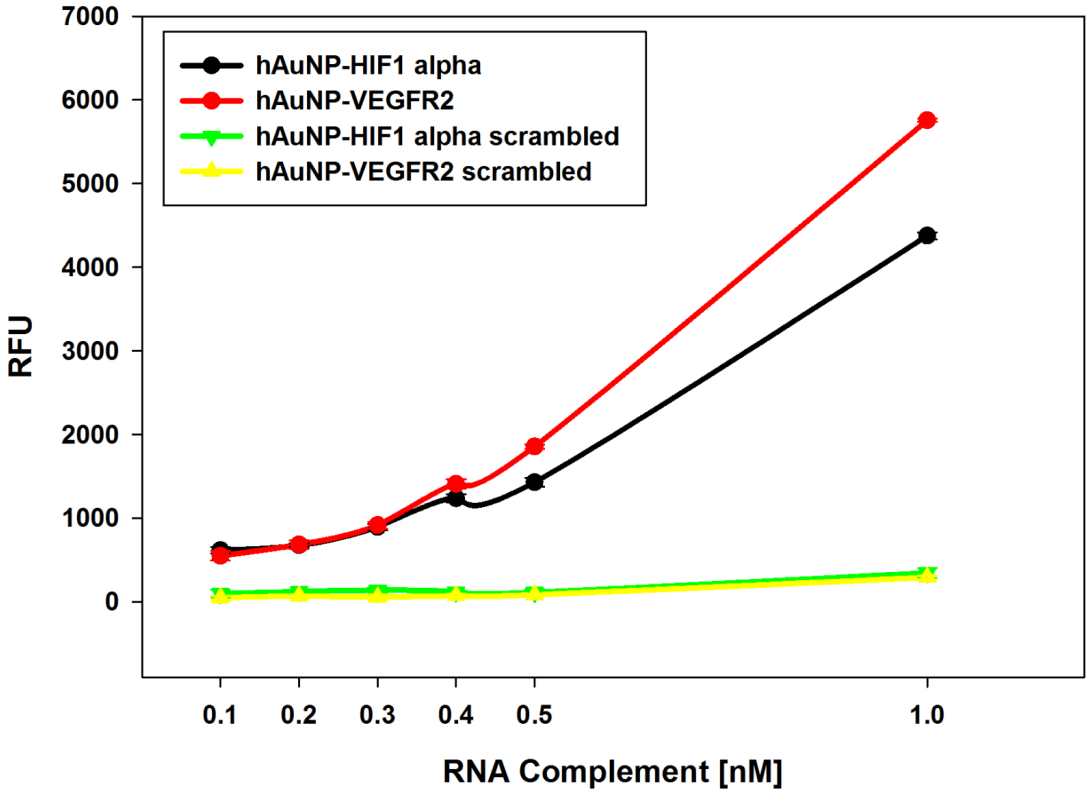

Figure 13. Fluorescence spectrophotometry studies showed an increase in fluorescent signal due to opening of hairpins when hAuNPs were incubated with their respective complement as opposed to a noncomplementary sequence.

To assess the same probes' ability to image cellular mRNA as opposed to synthetic complement, retinal microvascular endothelial cells were subjected to normoxia or hypoxia and incubated for two hours with 1 nM targeted or control hAuNPs. The hypoxic cells reveal upregulation of hypoxia-sensitive HIF1α as indicated by enhanced fluorescence emission signal, with stable levels of beta-actin. Beta-actin hAuNPs act as a loading control, showing that increased levels of HIF1α hAuNP fluorescence in hypoxic cells aren't due to an increased amount of probe uptake. Minimal background signal was detected from cells incubated with the same dose of HIF1α scrambled hAuNP.

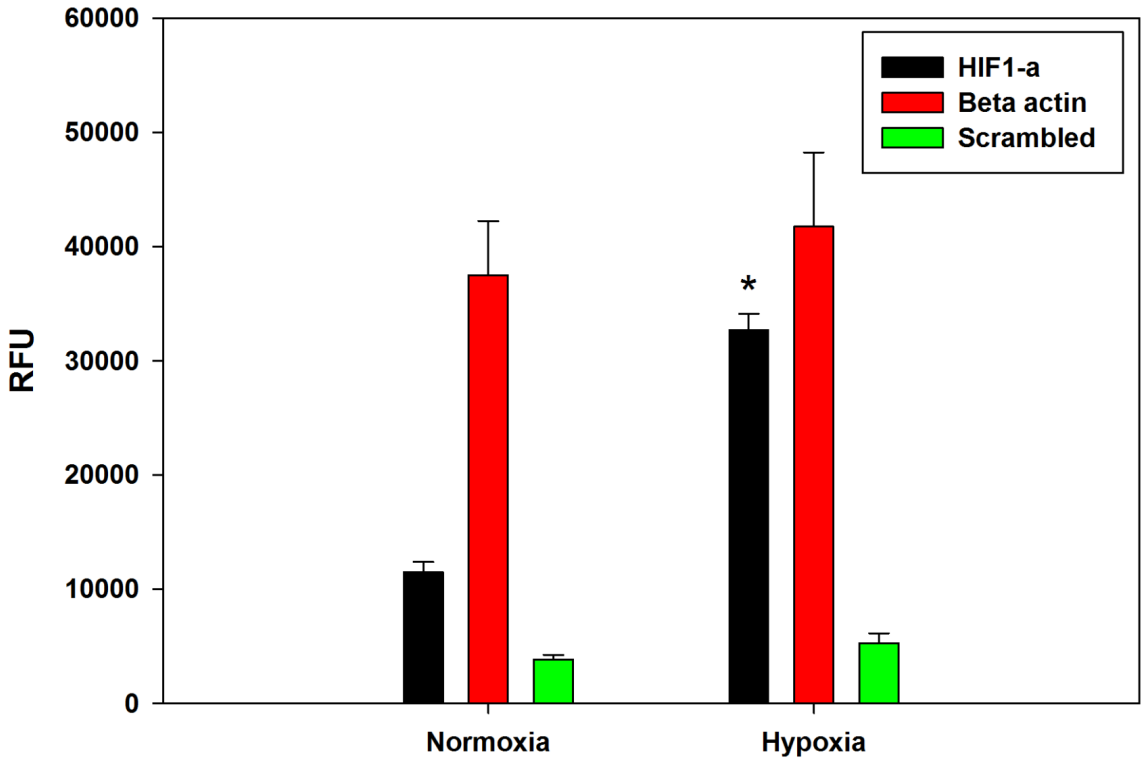

Figure 14. hAuNP uptake and fluorescence in human retinal microvascular endothelial cells. Hypoxia-sensitive HIF1a is upregulated as indicated by enhanced fluorescence from HIF1a hAuNPs and consistent levels of beta actin-specific hAuNPs.

Moving closer towards *in vivo* mRNA imaging with hAuNPs, it was important to establish that the retinal disease biomarkers we are targeting are present and are able to be imaged using established mRNA labeling techniques. To do this, fluorescence *in situ* hybridization (FISH) probes were added to retinal flat mounts of LCNV mice. Figure 15 shows that HIF1α and VCAM1 were present in significant amounts while a negative control probe shows little background fluorescence.

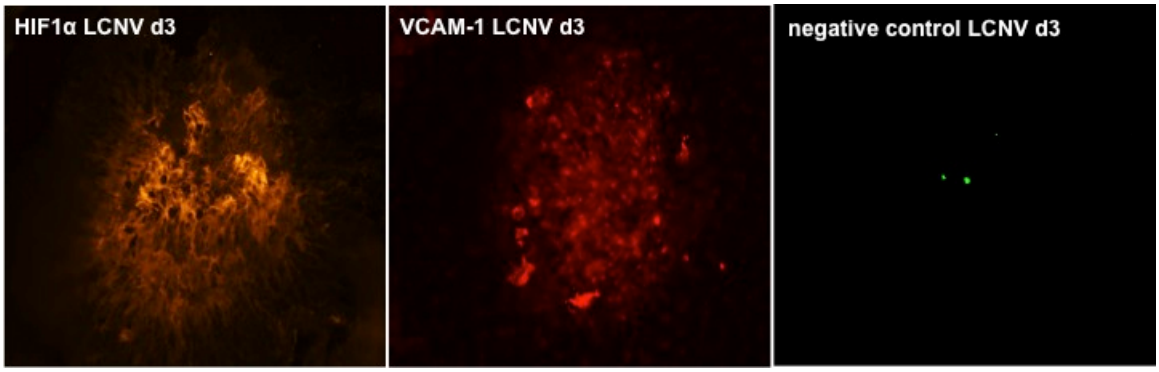

Figure 15. Fluorescence in situ hybridization analyses of retinal flat mounts from early LCNV (d3) mice reveal expression of HIF1a and VCAM-1. A negative control probe exhibited minimal fluorescence in flat mounts.

Unlike the FISH probes, hAuNPs are able to diffuse into cells without transfection reagents. This enables the administration of hAuNPs in a living animal intravenously. Figure 16 shows the expression of target mRNAs imaged in retinal flat mounts after an intravenously injected hAuNP solution in a LCNV mouse. HIF1α mRNAs could be detected by hAuNPs in early stage CNV (LCNV d1-d3).

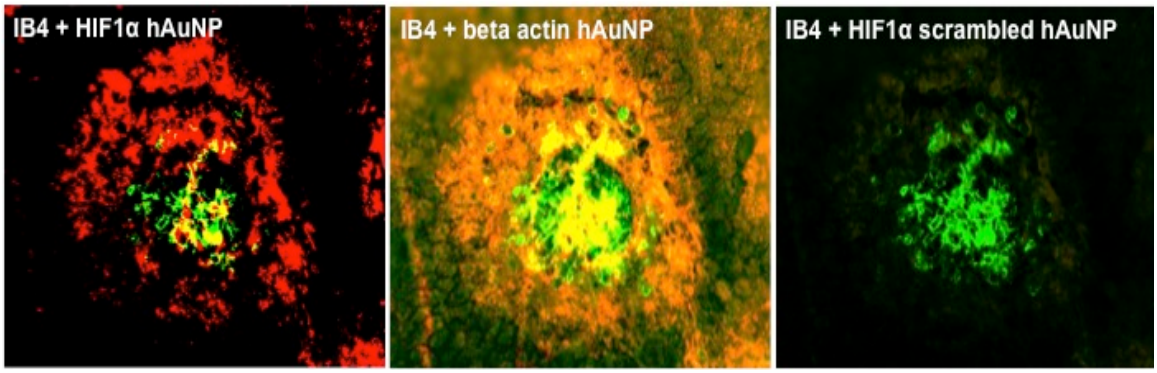

Figure 16. Retinal flat mounts from mouse models of LCNV (d3) were stained with isolectin B4 (IB4, green), a marker of endothelial cells lining blood vessels, to identify CNV lesions. Intravenously injected (50 uL of 20 nM solution) hAuNP targeting HIF1α and beta actin co-localized with CNV lesions, although beta actin targeted hAuNP labeled other ocular cells.

Similarly, VEGFR2-targeted hAuNPs revealed significant fluorescence emission signal and co-localization with CNV lesions, after a being intravenously injected.

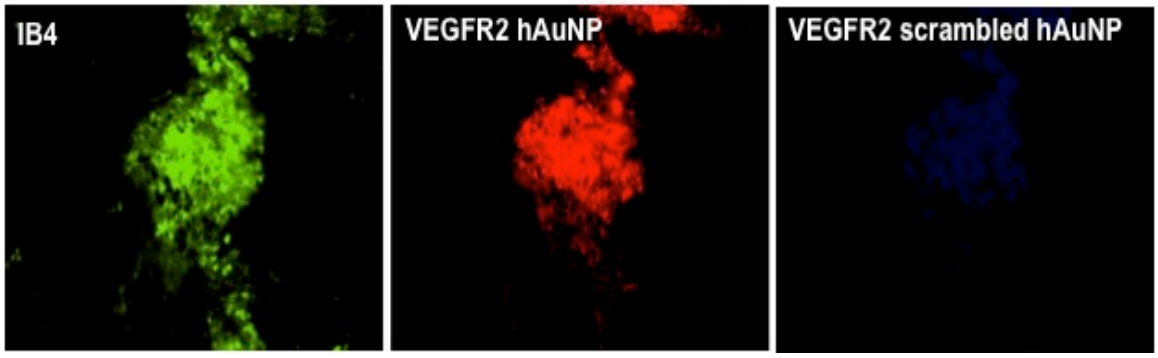

Figure 17. IB4 stained retinal flatmounts exhibiting advanced CNV (LCNV d5) revealed significant fluorescence emission signal from VEGFR2-targeted hAuNPs.

In humans, choroidal neovascularization has various patterns and configurations of proliferation that have been described based on its appearance with fluorescein angiography (FA). This technique allows one to determine the pattern, boundaries, composition and location of the neovascular lesions with respect to the center of the fovea. FA involves injection of sodium fluorescein into the systemic circulation, and then an angiogram is obtained by photographing the fluorescence emitted after illumination of the retina with a blue light, typically ~490 nm. Figure 18A shows a fluorescein angiogram in a LCVN d1 mouse. HIF1α targeted hAuNPs in the same retina showed localization at CNV lesions (Figure 18B) while a nonspecific scrambled HIF1α hAuNP did not show significant fluorescence (Figure 18C).

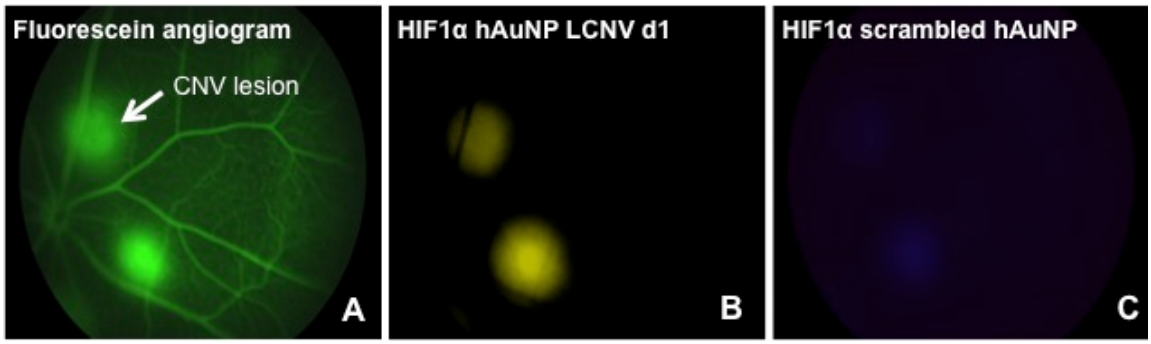

Figure 18. In vivo retinal imaging of injected fluorescein dye in LCNV d1 mice reveals CNV lesions (arrow). (B-C) In the same retina as shown in (A) (Pseudo-colored) Cy3-functionalized HIF1a targeted hAuNPs enable imaging of specific mRNA, whereas a Cy5-functionalized scrambled hAuNP did not exhibit significant signal above background tissue fluorescence.

HIF1α expression over time was also monitored by intravenous injections of hAuNPs in LCNV mice every 2 days for a week. Figure 19 shows the decrease in fluorescence emission from HIF1α-specific hAuNPs, indicating the healing of the laser-induced wounds.

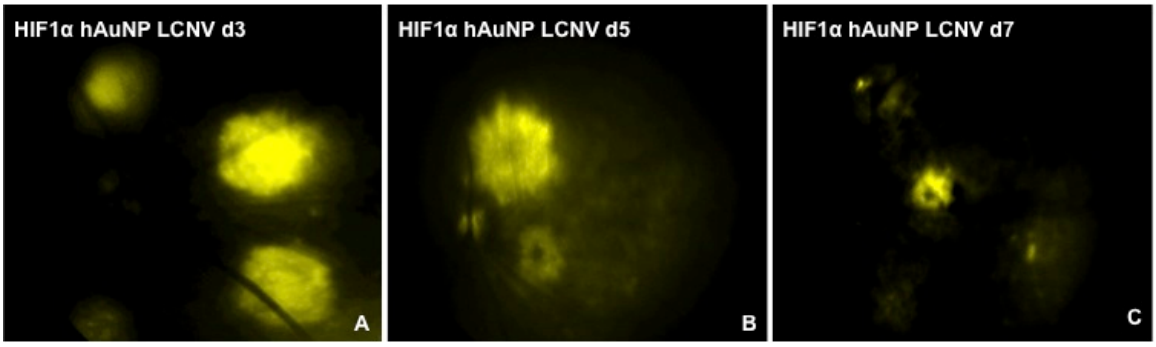

Figure 19. (A-C) Cy3 hAuNP targeting HIF1a were injected to longitudinally monitor HIF1a expression in LCNV mice, along with age-matched controls (not shown).

When emission intensities from hAuNPs were corrected for negative control hAuNP fluorescence, the total size of the lesion, and the native fluorescence from nearby unaffected tissues, large signal to noise ratios were observed over the course of CNV (Figure 20).

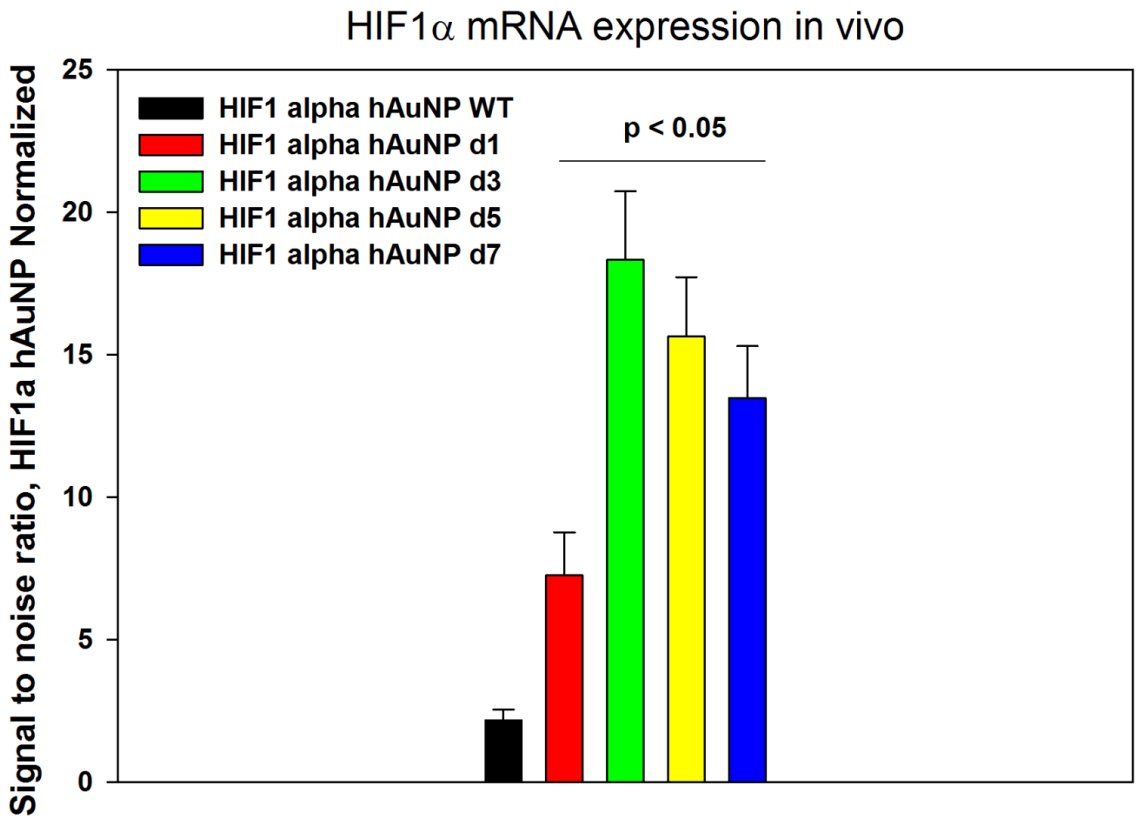

Figure 20. Signal to noise ratios calculated by measuring hAuNP emission intensities corrected for negative control hAuNP fluorescence, lesion area, and adjacent normal tissue fluorescence provided for quantification of HIF1a mRNA expression through the time course of CNV from early (day 1) to advanced stages (days 5-7) (n = 7 mice per group with 5 laser burns/retina).

The same analysis was applied toward monitoring of VCAM-1 mRNA expression in LCNV and age-matched control mice (n = 9 mice per group, 5 laser burns/retina). Figure 21 shows an illuminated image of a LCNV d7 mouse and fluorescence emission of VCAM-1 targeted hAuNPs.

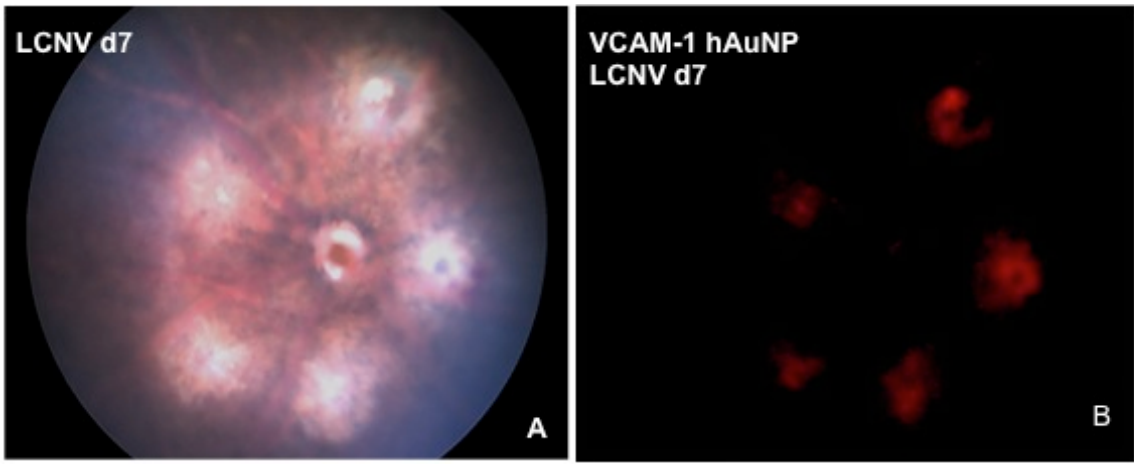

Figure 21. (A-B) Cy5 hAuNP targeting VCAM-1 were injected to longitudinally monitor VCAM-1 expression in LCNV mice. (A = white light illuminated image of (B)).

Similarly to HIF1a hAuNPs, corrected emission intensities from VCAM-1 hAuNPs displayed large signal to noise ratios over the course of CNV (Figure 22).

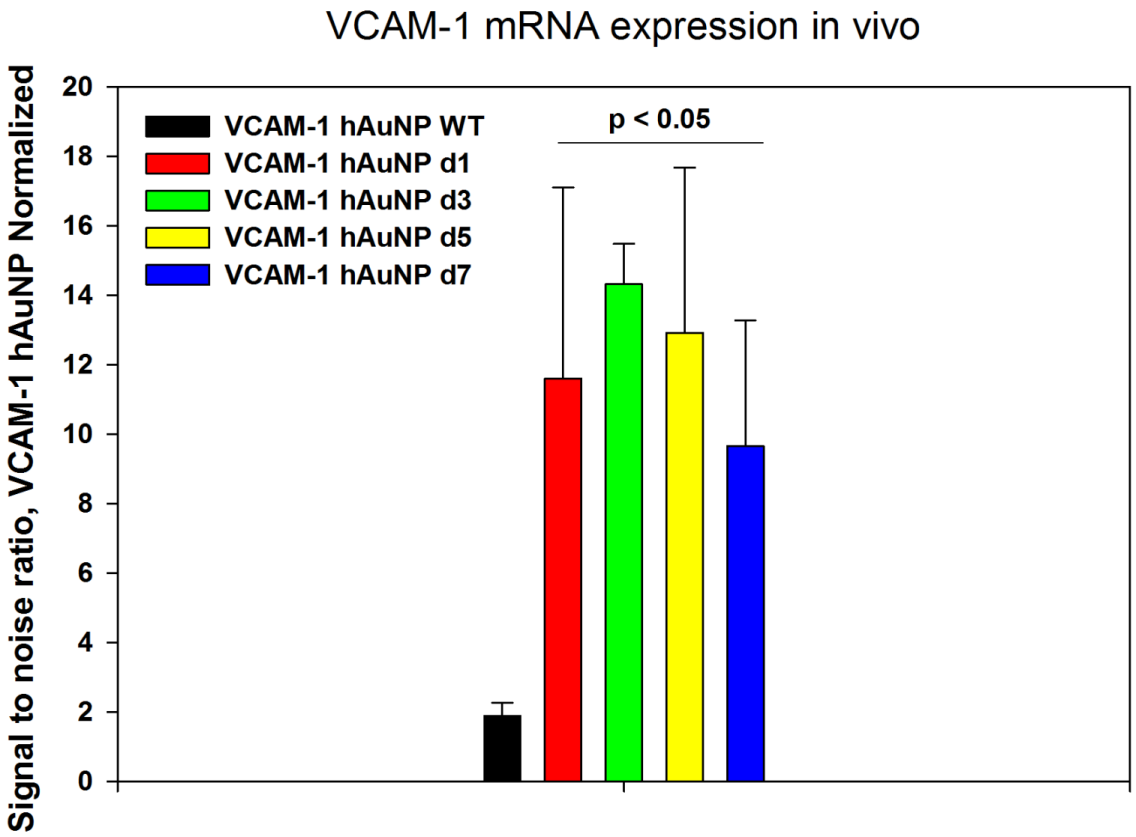

Figure 22. Signal to noise ratios calculated by measuring hAuNP emission intensities corrected for negative control hAuNP fluorescence, lesion area, and adjacent normal tissue fluorescence provided for quantification of VCAM-1 mRNA expression through the time course of CNV from early (day 1) to advanced stages (days 5-7) (n = 7 mice per group with 5 laser burns/retina).

The results of our experiments demonstrate that hAuNPs make up a large portion of the lesions, and that they frequently coalesce in the middle of the lesion. This observation suggests that hAuNPs home to the developing lesions through the blood stream and add to the growth of the lesions through their own proliferation as well as the release of growth factors, thereby encouraging neighboring mature endothelial cells to proliferate. This method of cell labeling

can be used to efficiently track and study the effects of these mRNAs or others influencing neovascular lesions.

Conclusions

hAuNP were specific for their targets in cell cultures and tissue as evaluated by confocal imaging, *in situ* FISH analysis, flow cytometry, and spectrophotometry. Specific imaging of RNA biomarkers was achieved in retinal tissue using in vivo retinal fluorescence imaging of LCNV animal models. Intravenous or subretinal administration of hAuNP was not associated with adverse effects on retinal tissue as evaluated by cell proliferation, ERG and TUNEL analysis. hAuNP are promising clinically translatable nanoscale imaging agents which can be utilized in conjunction with clinically-available ophthalmic imaging instrumentation for noninvasive, high sensitivity, and high specificity imaging of RNA disease biomarkers in retinal vascular disease.

References

1. Soubrane, G. (2008) Choroidal neovascularization in pathologic myopia: recent developments in diagnosis and treatment. *Surv Ophthalmol*, **53**, 121-138.

2. Grossniklaus, H.E., Ling, J.X., Wallace, T.M., Dithmar, S., Lawson, D.H., Cohen, C., Elner, V.M., Elner, S.G. and Sternberg, P., Jr. (2002) Macrophage and retinal pigment epithelium expression of angiogenic cytokines in choroidal neovascularization. *Mol Vis*, **8**, 119-126.

3. Sheridan, C.M., Rice, D., Hiscott, P.S., Wong, D. and Kent, D.L. (2006) The presence of AC133-positive cells suggests a possible role of endothelial progenitor cells in the formation of choroidal neovascularization. *Invest Ophthalmol Vis Sci*, **47**, 1642-1645.

4. Kent, D. and Sheridan, C. (2003) Choroidal neovascularization: a wound healing perspective. *Mol Vis*, **9**, 747-755.

5. Otani, A., Takagi, H., Oh, H., Koyama, S., Ogura, Y., Matumura, M. and Honda, Y. (2002) Vascular endothelial growth factor family and receptor expression in human choroidal neovascular membranes. *Microvasc Res*, **64**, 162-169.

6. Ferrara, N., Damico, L., Shams, N., Lowman, H. and Kim, R. (2006) Development of ranibizumab, an anti-vascular endothelial growth factor antigen binding fragment, as therapy for neovascular age-related macular degeneration. *Retina-the Journal of Retinal and Vitreous Diseases*, **26**, 859-870.

7. Kinose, F., Roscilli, G., Lamartina, S., Anderson, K.D., Bonelli, F., Spence, S.G., Ciliberto, G., Vogt, T.F., Holder, D.J., Toniatti, C. *et al.* (2005) Inhibition of retinal and choroidal neovascularization by a novel KDR kinase inhibitor. *Mol Vis*, **11**, 366-373.

8. Aiello, L.P. (2005) Angiogenic pathways in diabetic retinopathy. *N Engl J Med*, **353**, 839-841.

9. Schwesinger, C., Yee, C., Rohan, R.M., Joussen, A.M., Fernandez, A., Meyer, T.N., Poulaki, V., Ma, J.J., Redmond, T.M., Liu, S. *et al.* (2001)

Intrachoroidal neovascularization in transgenic mice overexpressing vascular endothelial growth factor in the retinal pigment epithelium. *Am J Pathol*, **158**, 1161-1172.

10. Song, S.J., Chung, H. and Yu, H.G. (2008) Inhibitory effect of YC-1, 3-(5'-hydroxymethyl-2'-furyl)-1-benzylindazole, on experimental choroidal neovascularization in rat. *Ophthalmic Res*, **40**, 35-40.

11. Ceradini, D.J., Kulkarni, A.R., Callaghan, M.J., Tepper, O.M., Bastidas, N., Kleinman, M.E., Capla, J.M., Galiano, R.D., Levine, J.P. and Gurtner, G.C. (2004) Progenitor cell trafficking is regulated by hypoxic gradients through HIF-1 induction of SDF-1. *Nat Med*, **10**, 858-864.

12. Arjamaa, O., Nikinmaa, M., Salminen, A. and Kaarniranta, K. (2009) Regulatory role of HIF-1alpha in the pathogenesis of age-related macular degeneration (AMD). *Ageing Res Rev*, **8**, 349-358.

13. Birch, D.G. and Liang, F.Q. (2007) Age-related macular degeneration: a target for nanotechnology derived medicines. *Int J Nanomedicine*, **2**, 65-77.

14. Riva, C.E., Cranstoun, S.D., Grunwald, J.E. and Petrig, B.L. (1994) Choroidal blood flow in the foveal region of the human ocular fundus. *Invest Ophthalmol Vis Sci*, **35**, 4273-4281.

15. Schlingemann, R.O. (2004) Role of growth factors and the wound healing response in age-related macular degeneration. *Graefes Arch Clin Exp Ophthalmol*, **242**, 91-101.

16. Zhu, J., Wang, Y.S., Zhang, J., Zhao, W., Yang, X.M., Li, X., Jiang, T.S. and Yao, L.B. (2009) Focal adhesion kinase signaling pathway participates in the formation of choroidal neovascularization and regulates the proliferation and migration of choroidal microvascular endothelial cells by acting through HIF-1 and VEGF expression in RPE cells. *Exp Eye Res*, **88**, 910-918.

17. Martin, G., Schlunck, G., Hansen, L.L. and Agostini, H.T. (2004) Differential expression of angioregulatory factors in normal and CNV-derived human retinal pigment epithelium. *Graefes Arch Clin Exp Ophthalmol*, **242**, 321-326.

18. Zhang, P., Zhang, X., Hao, X., Wang, Y., Hui, Y., Wang, H., Hu, D. and Zhou, J. (2009) Rac1 activates HIF-1 in retinal pigment epithelium cells under hypoxia. *Graefes Arch Clin Exp Ophthalmol*, **247**, 633-639.

19. Kvanta, A., Algvere, P.V., Berglin, L. and Seregard, S. (1996) Subfoveal fibrovascular membranes in age-related macular degeneration express vascular endothelial growth factor. *Invest Ophthalmol Vis Sci*, **37**, 1929-1934.

20. Toma, H.S., Barnett, J.M., Penn, J.S. and Kim, S.J. (2010) Improved assessment of laser-induced choroidal neovascularization. *Microvasc Res*, **80**, 295-302.

21. Yanni, S.E., Barnett, J.M., Clark, M.L. and Penn, J.S. (2009) The role of PGE2 receptor EP4 in pathologic ocular angiogenesis. *Invest Ophthalmol Vis Sci*, **50**, 5479-5486.

22. Kaplan, H.J., Leibole, M.A., Tezel, T. and Ferguson, T.A. (1999) Fas ligand (CD95 ligand) controls angiogenesis beneath the retina. *Nat Med*, **5**, 292-297.

23. Bora, P.S., Hu, Z., Tezel, T.H., Sohn, J.H., Kang, S.G., Cruz, J.M., Bora, N.S., Garen, A. and Kaplan, H.J. (2003) Immunotherapy for choroidal neovascularization in a laser-induced mouse model simulating exudative (wet) macular degeneration. *Proc Natl Acad Sci U S A*, **100**, 2679-2684.

CHAPTER V

ANISOTROPIC GOLD NANOPARTICLES

Biological Applications of Gold Nanorods

The DNA hairpin-gold nanoparticle (hAuNP) has provided a new tool that can be applied to any system of interest to allow for live cell imaging of a specific sequence of mRNA and to learn about how that sequence is trafficked within the cellular environment. However, these probes can be further utilized by varying the construct of the gold nanoparticle. Over the past decade, gold nanoparticles having non-spherical morphologies have opened up additional possibilities for sensing and imaging applications. Anisotropic nanoparticles are expected to have different chemical reactivity as a result of varying ligand and crystallographic packing (1-3). Second, and perhaps most interestingly, non-spherical particles have different absorption profiles and potentially will be better suited as quenchers in parts of the electromagnetic spectrum available to cellular imaging. Gold particles having an anisotropic shape, such as a rod-like morphology like those shown in Figure 23, are of particular interest due to their large absorption cross-section, a narrow spectral width of the longitudinal plasmon resonance band, and tunability of the longitudinal plasmon resonance wavelength based on aspect ratio.

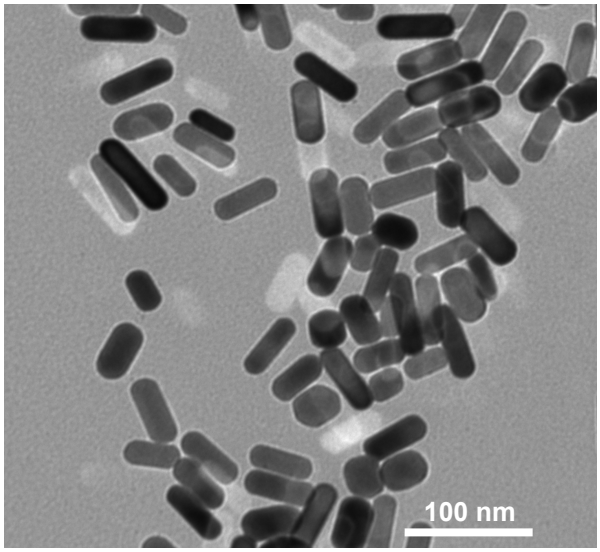

Figure 23. Transmission electron micrograph of synthesized CTAB-coated gold nanorods.

Gold nanorod absorption spectra exhibit two plasmon bands that correspond to localized surface plasmon resonance (LSPR) along their length (longitudinal resonance) and across their diameter (transverse resonance) (4). LSPR occurs when an electromagnetic field drives the collective oscillations of a nanoparticle's free electrons into resonance. This classical effect was theoretically described by Mie in 1908 by solving Maxwell's equations for a plane wave incident on a metal sphere surrounded by a dielectric medium, given the dielectric function of the metal. Mie theory provides an exact analytical solution for nanosphere LSPR in terms of a multipole expansion. Although the lack of spherical symmetry precludes an exact analytical description of their LSPR by Mie theory, gold nanorod spectra are qualitatively described by Gans theory, which is an extension of Mie theory derivitized for spheroidal nanoparticles. Gans theory calculates a depolarization factor along each axis of the spheroid based on the aspect ratio of the semimajor and semiminor radii. In both Gans

theory for spheroids and experimental measurements on gold nanorods, as the aspect ratio increases, the longitudinal mode along the semimajor axis red shifts and the transverse resonance along the semiminor axis slightly blue shifts. However, the agreement is only qualitative. To quantitatively fit a nanorod spectrum with Gans theory usually requires an unrealistically large dielectric constant for the medium (4,5). Also Gans theory overestimates the size of the extinction cross-section relative to recent experimental measurements (6,7).

As mentioned before, the longitudinal plasmon band of nanorods is tunable based on aspect ratio. As the rod length increases, so does the plasmon frequency position. This means that gold nanorods may be tailored to have strong absorptions spanning a wide range of wavelengths, i.e. visible or near-infrared (NIR), simply by changing rod length. Rods have been synthesized with aspect ratios ranging from 1.3 to 20 with longitudinal bands at 700 to 1400 nm, respectively. Particles that absorb between 700-900 nm are of particular physiological interest due to the large penetration depth of near-infrared (NIR) radiation in most biological media. Pairing a NIR dye on the end of the hairpin-DNA probe with a NIR-absorbing gold particle would offer the potential for imaging at significant depths in living tissues.

Furthermore, particles having anisotropic shapes may possess different chemical affinities for different crystallographic faces making possible controlled assembly (1-3). For example, gold nanorods have been shown to link preferably end-to-end under appropriate conditions (8). This is due to differences in gold atom packing on the end faces when compared to side-face packing. This type

of particle linking leads to plasmonic coupling resulting in controlled frequency shifts (8). Gold nanorods have also demonstrated the ability to enhance quantum yields of fluorescent molecules at specific distances from the rod surface (9). This enhancement is unique and does not occur with spherical particles, which are known only to quench fluorescence as a result of a FRET-like mechanism.

Gold nanorods are often prepared following a seed-mediated approach in which spherical “seed” nanoparticles (~ 4 nm) are added to a growth solution containing gold salt, silver nitrate, ascorbic acid, and cetyltrimethylammonium bromide (CTAB) leading to the formation of gold nanoparticles having a rod-like morphology (1). Mechanistically, gold salt in the growth solution is slowly reduced in the presence of “seed” particles while the growth-directing agent, CTAB, facilitates rod formation by binding preferentially to the side faces of the nanoparticle. Silver nitrate additions are varied to alter rod length resulting from under-potential deposition of silver on the gold nanorod surface. Once synthesized, gold nanorod solutions are purified via centrifugation to remove excess CTAB, unreacted metal ions, and ascorbic acid. This step is important as CTAB is known to be cytotoxic and failure to remove unreacted species will result in morphological changes over time. Other methods for nanorod synthesis include the electrochemical method in which nanorods are grown in an electrolytic solution between two electrodes under a 3 mA current, a photochemical synthesis in which gold nanorods are formed by the UV irradiation of gold salt in the presence of CTAB and tetradodecylammonium bromide, and

the electrochemical method in which gold nanorods are grown by electrochemically depositing metal inside a porous membrane (10-12).

While control over nanoparticle shape and size continues to be an underlying theme in current research efforts, much of the recent research has shifted toward the manipulation of these metallic particles for biological and medicinal applications. As a result of the concerted effort to understand their fundamental properties, metallic nanoparticles have become viable materials for improvements in medicine and biological processes.

The Transition to Application Based Research

Despite their unique optical properties, carrier functionality, colloidal stability, and cytotoxicity have hindered the widespread use of gold nanorods as carriers in biological and biomedical applications. Therefore, to harness the full potential of nanomaterials in these applications, the surface coating material as well as the gold core material deserves attention. With respect to cytotoxicity, while the gold core is widely accepted as being biocompatible, bare gold nanoparticles are known to interact with proteins and induce misfolding under physiological conditions. Specifically, in the case of gold nanorods, the asymmetric geometry is obtained by synthesizing the nanorods in the presence of a high concentration (0.1 M) of cetyltrimethylammonium bromide (CTAB), a cationic micellar surfactant. However, CTAB is known to degrade biomembranes and peptides, raising significant concern about the cytotoxicity of CTAB-coated nanorods *in vivo*. CTAB has a poor biocompatibility profile with *in vitro*

toxicological studies yielding IC_{50} values in the low micromolar range. The cytotoxic effects of CTAB-coated nanorods can be minimized by reducing the CTAB concentration below the critical micellar concentration, but at the expense of the nanrod suspension stability. This has severely limited the use of nanorods in biological applications, especially when compared to non-CTAB containing Au nanospheres. As a result, gold nanorods and other formulations containing CTAB will require a rigorous purification process prior to clinical testing.

The unresolved issue of biocompatibility underlies the numerous methods of surface coating methodologies developed for Au nanorods and other nanoparticles in recent years. Most of these appear to be useful for exploratory investigations in a laboratory setting, although few if any have been subject to the rigors of through preclinical evaluation. For example, a widely used method of nanoparticle coating involves the electrostatic physisorption of polyelectrolytes, which can provide dispersion stability as well as providing functionality for the immobilization of antibodies or protein biomarkers. However, the stability and biocompatibility of nanoparticles functionalized in this manner cannot be assumed, as the surface binding energies are often variable or attenuated under physiological conditions with possible leaching of the physisorbed species. Chemisorption of alkanethiols and other organosulfur molecules on noble metal nanostructures has been widely used due to their ability to form well-organized self-assembled monolayers. However, with alkanethiol molecules such as 11-mercaptoundecanoic acid and thiocitic acid, only partial functionalization is typically obtained at the ends of gold nanorods. Complete replacement of the

CTAB molecules with thiols is non-trivial as a fine balance is required to avoid irreversible aggregation of the nanoparticles upon destabilization of the protective CTAB bilayer.

The goal of this work is to expand upon the current capabilities and applications of gold nanoparticle-MBs. To do so, we will first synthesize different sizes and shapes of gold nanoparticles, including spheres, rods, cubes, and stars. After synthesis we will functionalize nanostructures with the designed hairpin DNA probes. As the different structures have different surfactants and surface properties, numerous functionalization strategies will be employed.

Methods

Synthesis of nanorods

Gold nanoparticle seed solution was prepared first by adding 0.6 mL of an ice-cold solution of 10 mM sodium borohydride to 10 mL of 2.5 x 10^{-4} M gold chloride solution prepared in 0.1 M CTAB solution under vigorous stirring. The yellow color changed immediately to brown indicating the formation of gold nanoparticle seeds. Stirring was continued further for 2 minutes. The following solutions were then added to an Erlenmeyer flask in the order mentioned: 95 mL 0.1 M CTAB solution, 0.3 – 1.0 mL 10 mM silver nitrate solution, and 5 mL 10 mM chloroauric acid. To this 0.55 mL of 0.1 M ascorbic acid was added and the mixture was homogenized by swirling gently. Finally 0.12 mL of seed solution was added and the entire solution was homogenized and left undisturbed

overnight. The violet-brown colored gold nanorod solution was purified by centrifugation to remove excess CTAB (twice at 13,300 rpm, 10 minutes).

Synthesis of nanocubes

Seed particles were prepared using a 7.75 mL growth solution containing 0.1 M CTAB and 3.23×10^{-4} M $HAuCl_4$. To this growth solution, 600 µL of an ice cold 0.01 M $NaBH_4$ solution was added. The resulting solution was stirred for 2 minutes and allowed to sit for one hour before use. The seed solution was diluted by a factor of 10 using DI water. Growth solutions were prepared that contained 4 mL of DI water, 800 µL of 0.1 M CTAB and 100 µL of 0.01 M $HAuCl_4$. A 600 µL portion of 0.1 M ascorbic acid was then added to the growth solution and mixed thoroughly, turning the solution colorless. Next, 2.5 µL of the diluted seed solution was added to the reaction vessel, and the solution was allowed to sit overnight. Nanocube solutions were purified using two rounds of centrifugation at 13,300 rpm for 10 minutes each.

Synthesis of nanostars

20 nm PVP-coated Au seeds in ethanol were prepared according to a modified version of the protocol by Graf *et al*., resulting in a colloidal suspension containing [Au] = 1.75 mM. A 10 mM solution of PVP in 15 mL DMF was prepared, into which 84 µL of an aqueous solution of 50 mM $HAuCl_4$ was added. 700 µL of either the synthesized 20 nm PVP-coated seeds, or 15 nm citrate-capped Au spheres purchased from Ted Pella were injected into the solution

under vigorous stirring. Within 30 minutes of synthesis, the solution experienced a three-color transition: pink to colorless to blue.

Polyelectrolyte coatings with sulfo-SMCC coupling

One mL aliquots of 4x concentrated gold nanorods were added to 1.5 mL microcentrifuge tubes. To this, 200 µL of PAA stock solution (10 mg/mL prepared in 10 mM NaCl solution) and 100 µL 10 mM NaCl were added simultaneously and vortexed for 2 minutes. After 30 mintues adsorption time, the excess polymer in the supernatant fraction was removed by centrifugation (13,300 rpm, 8 minutes), and the pellet was redispersed in 1 mL DI water. 200 µL of PAH stock solution (10 mg/mL prepared in 10 mM NaCl solution) and 100 µL 10 mM NaCl were added simultaneously and vortexed for 2 minutes. After 30 minutes adsorption time, the excess polymer in the supernatant fraction was removed by centrifugation (13,300 rpm, 8 minutes), and the pellet was redispersed in 1 mL water. Various amounts of sulfo-SMCC stock solution (1.2 mg/mL PBS) were added for final concentrations ranging from 1.2-120 µg/ml. After mixing for 30 minutes, the excess sulfo-SMCC was removed by centrifugation (13,300 rpm, 8 minutes), and the pellet was resuspended in 1 mL DI water.

CTAB-to-thiol exchange

1 mL of 30 mM cystamine dihydrochloride was added to 10 mL of purified CTAB-stabilized gold nanorods, and the solution was kept at 50 °C under

constant sonication for 3 hours. The solution was then centrifuged at 8,000 rpm for 10 minutes to remove excess CTAB and cystamine dihydrochloride.

The polyethylene glycol layer was formed by adding equivalent volumes of gold nanorods (as-prepared, roughly 0.5 nM) in water and polyethyleneglycol-thiol solution (1 mg/mL in H_2O) were mixed, sonicated for 30 s and left to react for 2 h. Excess PEG molecules were removed by centrifugation at 7,000 rpm for 10 minutes and the PEGylated rods were resuspended in H_2O.

Exchanges involving a nonionic surfactant

500 µL of 0.1 mM unmodified CTAB-coated nanorods were centrifuged at 5,000 rpm for 10 minutes. A 10 µL pellet was transferred to a new microcentrifuge tupe, resuspended in 500 µL of 0.01 mM Brij56, briefly vortexed, and sonicated for 1 minute.

Gold nanorod overgrowth

As-synthesized nanorods were spun down (10 min, 13400 rcf) once and resuspended in water, followed by a second centrifugation to concentrate the particles with resuspension in 0.01 M CTAB. Nanorod concentrations were quantified using optical extinction spectra and the absorbance value ant the longitudinal surface plasmon resonance (LSPR) maximum. A 900 pM solution of nanorods was then prepared in 0.01 M CTAB and sequentially brought to 1 mM ascorbic acid and 0.005 mM $HAuCl_4$. After allowing 30 min to 1 h for the overgrowth to occur, the solution was then brought to 0.05 M CTAB.

When ready to functionalize with DNA, the 0.05 M CTAB-stabilized particles were spun down twice and resuspended in DI water. hDNA was then immediately added to the colloidal solution. After allowing 3 hours for the hDNA to react with the gold surface, the solutions were brought to 0.01% dodecyl sulfate (SDS) and 0.01 M sodium phosphate and allowed to sit for 1 h. The solution was then buffered to 0.1 M NaCl and incubated for 4 h at RT. The NaCl concentration was then adjusted to 0.2 M and the solution was incubated for an additional 4 h at RT. Finally, the NaCl concentration was adjusted to 0.3 M and incubated for a final 4 h at RT. The solution was then centrifuged at 21,100 g for 20 min and the AuNPs were resuspended in PBS with 0.01% SDS. The process of centrifugation and resuspension was repeated two more times.

Results and Discussion

Synthesis of nanorods

Gold nanorods were synthesized by seeded growth methods in micellar CTAB solutions as described by Murphy *et al.* to have distinct aspect ratios and morphologies (13,14). Figure 24 shows the observed optical absorption of gold nanorods of different aspect ratios obtained by varying the silver nitrate concentration during the growth process. The longitudinal absorption band shifts from the visible to the NIR. As-prepared gold nanorods are capped with a bilayer of CTAB, giving these nanorods a net positive surface charge (approximately +40 mV) from the quaternary ammonium surfactant headgroup (15). While the nature of the CTAB-gold interactions is the subject of some debate, there is evidence to

suggest it is mediated by electrostatic interactions between adsorbed bromide anions at the gold nanorod surface (1,15). In addition, the surfactant bilayer is stabilized by hydrophobic interchain coupling interactions within the bilayer (16).

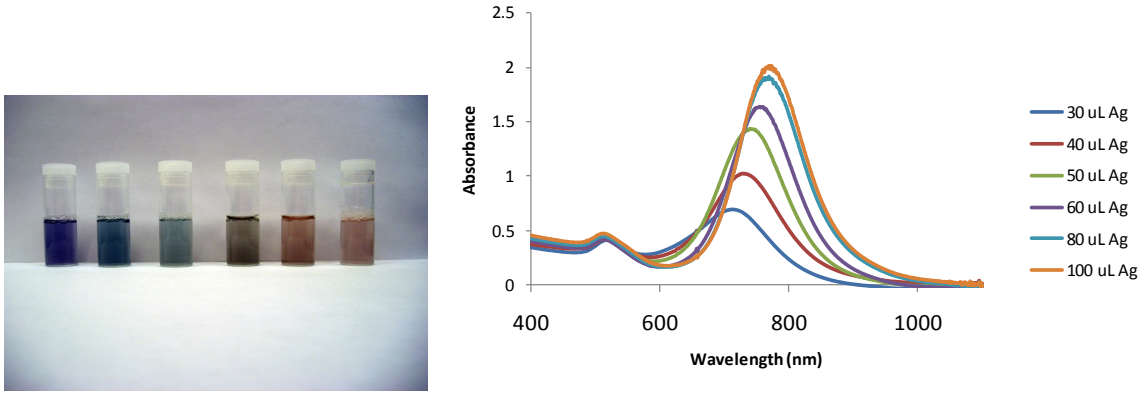

Figure 24. (Left) Photograph of aqueous solutions of gold nanorods as aspect ratio (AR) increases from left to right. (Right) UV-Vis spectra of the same series with the lowest AR corresponding to the smallest silver addition.

Synthesis of nanocubes

Unlike nanorods which are prepared in the presence of a large quantity of CTAB, gold nanorcubes are formed in the presence of a lesser amount of CTAB. Figure 25 shows a typical transmission electron micrograph (TEM) of the synthesized gold nanocubes with their average particle size being approximately 45 nm. It is believed that, as in the case of Pt^0-polymer systems reported by El-Sayed *et al*., the shape of the fine Au seeds produced in the presence of CTAB is faceted with the most stable [111] faces solvent-accessible. CTAB molecules appear to bind more strongly to the [100] than the [111] faces. Thus, lower CTAB and higher ascorbic acid concentration conditions favor the faster formation and deposition of Au^0 onto the [111] faces, leading to their

disappearance and the formation of [100] faces, thereby producing cubic shapes (17). Gold cubes have only one plasmon band at approximately 545 nm. The gold nanocubes also possess a bilayer of the structure-directing surfactant CTAB imparting a high positive effective charge to the particles and leads to the trimethylammonium headgroup of CTAB facing the solvent (1,15,18).

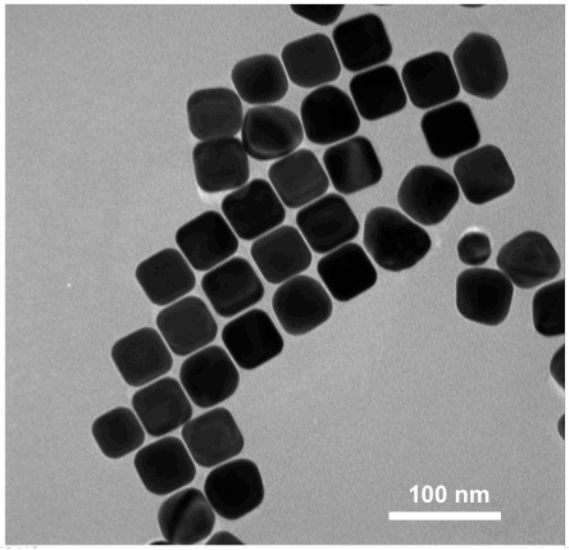

Figure 25. TEM of synthesized nanocubes.

Synthesis of nanostars

The procedure for synthesis of star-like, multipod nanoparticles is based on the reducing ability of N,N-dimethylformamide (DMF), in combination with a large concentration of poly(vinylpyrolidone) (PVP) as a stabilizer, and preformed nanoparticle seeds as catalysts (Figure 26). The yield of branched particles is extremely high (near 100%). The size of nanostars is controlled by varying the concentration of Au seed suspended in a DMF growth solution. The higher the seed concentration, the lower the number of available Au atoms per seed and,

thus, the smaller the resulting nanostar. A negative correlation also exists between seed concentration and synthesis time: the higher the seed concentration, the thinner the deposition layer of Au atoms per seed and, thus, the shorter the time until depletion of Au atoms in the growth solution. It is also hypothetically possible to control the star size by increasing the $HAuCl_4$ concentration in the growth solution yielding larger stars, but this approach would require impractical PVP concentrations to maintain the large [Au]/[PVP] ratio required for the reduction of $HAuCl_4$ and formation of the branches, as previously pointed out (19).

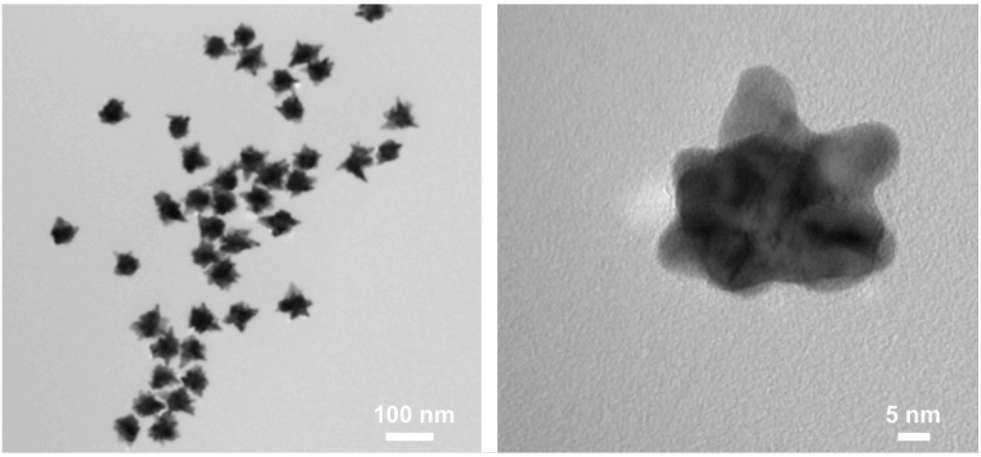

Figure 26. TEMs of synthesized nanostars.

Polyelectrolyte coatings with sulfo-SMCC coupling

A layer-by-layer (LbL) approach to nanorod surface modification has been developed by the groups of Decher (20-23), Moehwald (24-27), and Caruso (28-33) and used extensively to coat different 2-D and 3-D surfaces. This approach involves sequential deposition of anionic and cationic polyelectrolytes onto

oppositely charged surfaces through electrostatic self-assembly. In our case, the as-prepared gold nanorods are positively charged due to the presence of the CTAB bilayer. The nanorods were further coated with two layers of polymers: anionic poly(acrylic acid) (PAA) and cationic polyallylamine hydrochloride (PAH). The amine-terminated rods were then allowed to react with sulfosuccinimidyl-4-(N-maleimidomethyl)cyclohexane-1-carboxylate (sulfo-SMCC) at the amine-reactive N-hydroxysuccinimide end to form a stable amide bond. The sulfhydryl-reactive maleimide group was then available to react with the sulfhydryl groups present at the end of the DNA hairpin.

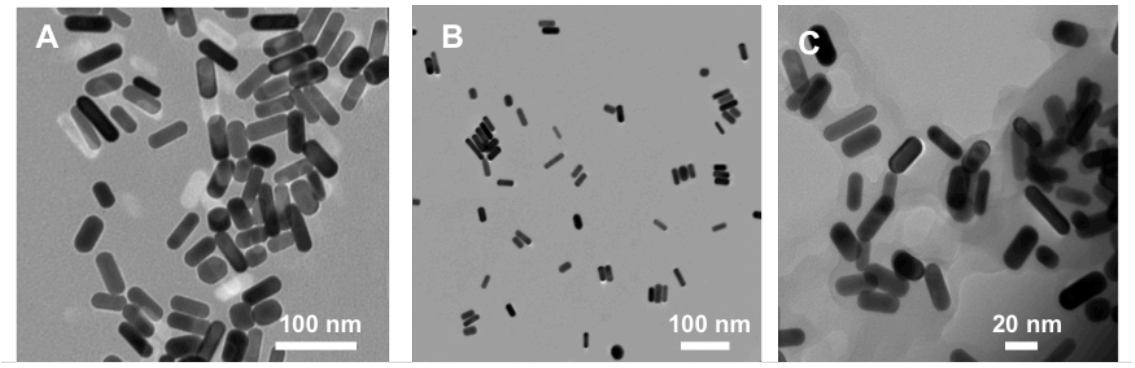

Figure 27. AuNRs (A) before polyelectrolyte addition, (B) after PAH coating, and (C) after SMCC coupling.

Even at low concentrations of sulfo-SMCC (μM) this approach resulted in aggregation of the rods due to the formation of a group coating shown in the TEM images in Figure 27. This is not ideal for our purposes, as the conjugated DNA and fluorophore is much too far from the surface of the rod for quenching to occur.

CTAB-to-thiol exchange

Instead of coating the tightly packed CTAB bilayer, another approach for making biocompatible nanorods is to exchange the surfactant altogether, replacing it with covalently bound thiolated ligands. While there are several reports of such a direct exchange, replicating the procedures proved challenging. Water soluble cystamine has been proposed to fully activate the gold nanorod surface using a disulfide that can access the gold nanorod surface more easily than a single thiol in organothiol compounds, which are insoluble in water. In this procedure, control of reaction temperature is the key to success of the amine activation protocol. The temperature is increased to drive CTAB molecules to dissociate from the gold nanorod surface; however, if the temperature is increased too much or rises too quickly, the exposed gold nanorods will aggregate. The normalized visible /NIR spectra measured for gold nanorods before and after amine modification show that the optical properties of the gold nanorods are altered (Figure 28). The amine terminated gold nanorods showed a blueshift of approximately 5 nm.

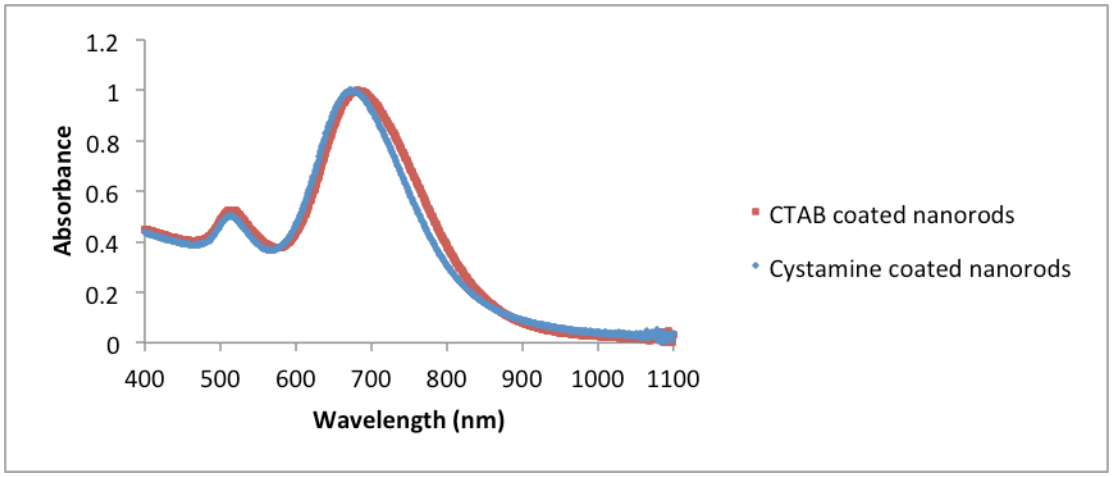

Figure 28. UV-Vis absorption spectra of CTAB coated nanorods before and after functionalization with cystamine.

After centrifugation, however, the cystamine coating on the rods seems to be unstable and fails to prevent aggregation as indicated by the large, broadened longitudinal peak shown in Figure 29.

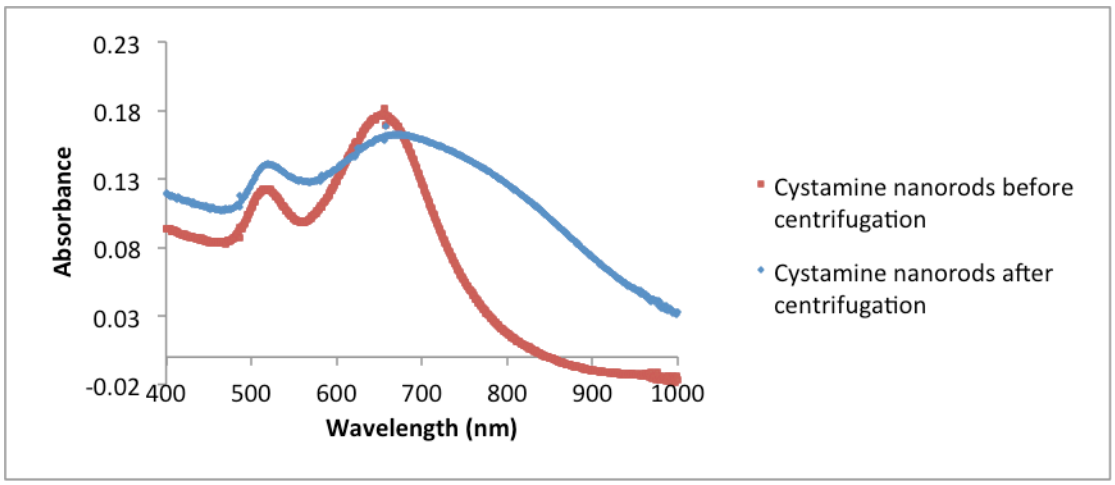

Figure 29. UV-Vis absorption spectra of cystamine coated nanorods before and after centrifugation.

In order to provide more stability while centrifuging, a longer thiolated ligand was chosen to displace the CTAB bilayer. O-(2-Mercaptoethyl)-O'-methylpolyethylene glycol (PEG-SH) (5,000 MW) was thought to be able to provide efficient steric stabilization of the nanoparticles during the ligand

exchange reaction. Less aggregation did occur; however, the bulky ligands prevented a pellet from being formed after centrifugation at 21,100 g. Even if a pellet had been formed, the 5,000 MW PEG was not ideal for our purposes, since its bulk might interfere with the hDNA. When a smaller PEG thiol was used, poly(ethylene glycol) monomethyl ether thiol 1,000, the particles did pellet out of solution after centrifugation. However, upon addition of hDNA and phosphate buffer, the AuNRs irreversibly aggregated and crashed out of solution.

Exchanges involving a nonionic surfactant

An alternative route to achieving thiolated nanorods is to first place-exchange the CTAB surfactant with the nonionic surfactant Brij56, followed by place-exchange with the thiolated molecule. Lee *et al*. published a procedure for a similar two-step place-exchange with Brij56 that resulted with a cationic phospholipid (34). This procedure was modified and multiple thiolated ligands were used during the secondary exchange. The increase in particle radius and decrease in zeta potential shown in Figure 30 both support the successful exchange from the smaller, positively charged CTAB to the larger, non-ionic Brij molecule.

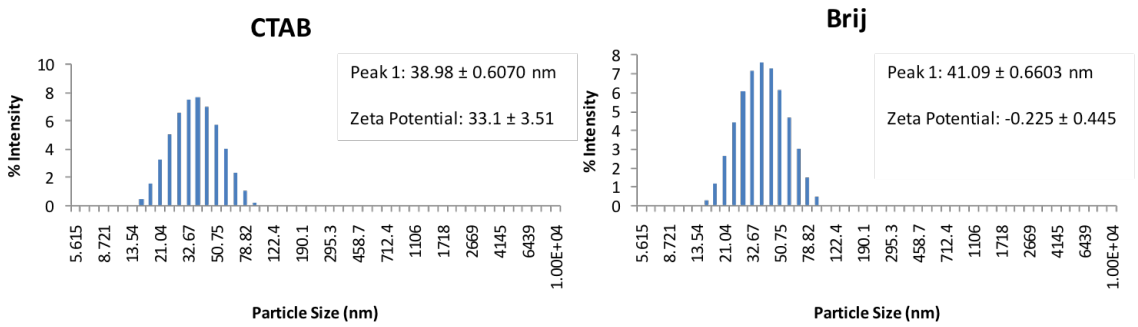

Figure 30. Dynamic light scattering and zeta potential measurements for CTAB and Brij56 coated nanorods.

As shown in Figure 31, nanorods with Brij56 as a surfactant are also subject to aggregation after centrifugation. It is hypothesized that while a positively or negatively charged surfactant sufficiently prevents aggregation by ionic repulsion, a non-ionic surfactant does not.

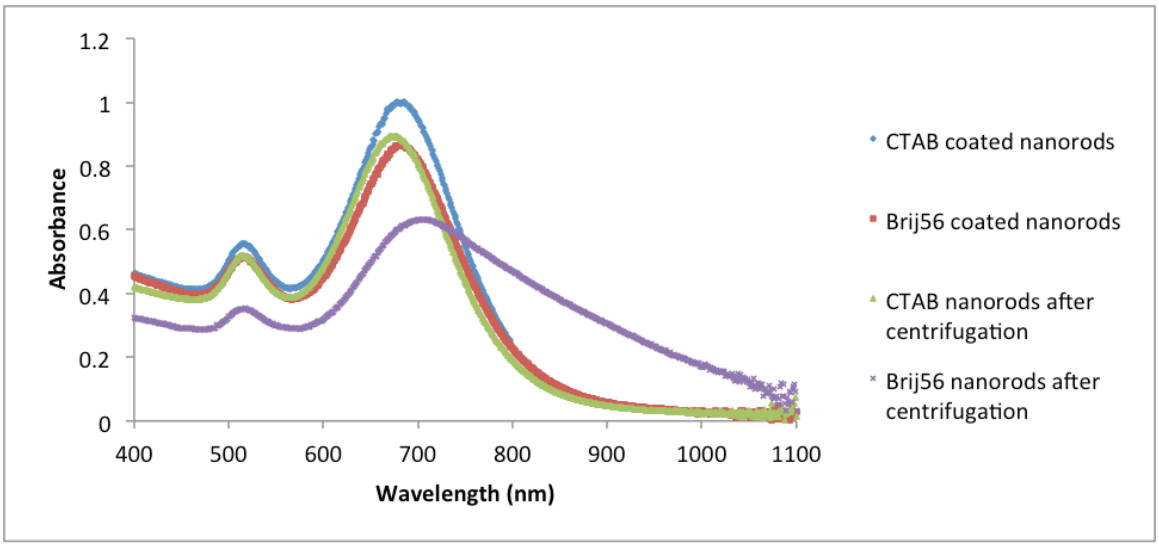

Figure 31. CTAB and Brij56 coated nanorods before and after centrifugation.

Gold Nanorod Overgrowth

Jones *et al*. observed that gold nanorods synthesized using the silver-assisted growth procedure could not be functionalized with oligonucleotides as

evidenced by either particle aggregation during the salting step or a lack of cooperative melting behavior, which indicates low DNA density on a nanoparticle's surface. They hypothesized that the difficulty in conjugating thiolated DNA to the particle was due to a thin layer of silver present on the nanorod surface preventing Au-S bond formation. This may be the case, or alternatively, a cetyltrimethylammonium-Br-Ag^+ complex exists on the surface of the AuNR and while displacing the CTAB, Ag^+ ions are also removed. This could compromise the integrity of the crystal structure of the AuNR resulting in aggregation. Either way, an additional overgrowth procedure was used to deposit a thin layer of gold on the nanorod, which allowed for facile DNA functionalization. The overgrown nanorods showed minimal change in their optical properties and their dimensions, but were able to be functionalized with oligonucleotides.

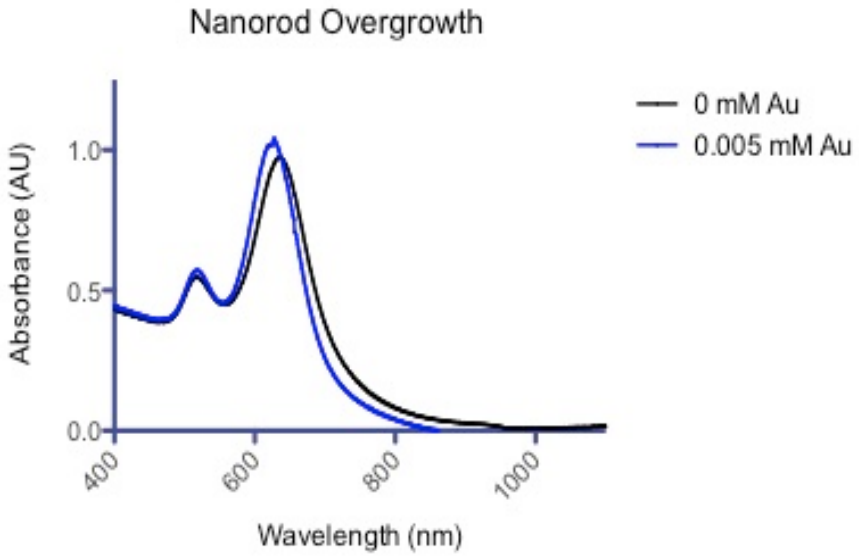

Figure 32. Absorbance spectra of gold nanorods before (black) and after (blue) overgrowth procedure.

Hairpin DNA was conjugated to the overgrown AuNRs by a protocol similar to that which hAuNPs were functionalized in Chapters 3 and 4. Changes to the AuNRs after functionalization were monitored by DLS and zeta potential measurements (Table 1). The effects of conjugation were comparable to those seen with DNA conjugation to spherical AuNPs.

Table 1. DLS and Zeta potential measurements for DNA functionalized AuNRs.

	CTAB	hDNA	Complement	Mismatch	None
Hydrodynamic Radius (nm)	68.28 ± 0.250	76.89 ± 0.654	85.93 ± 1.274	75.67 ± 1.925	81.54 ± 2.279
Zeta Potential (mV)	37.0 ± 1.64	-0.72 ± 1.5	-6.49 ± 0.78	-5.98 ± 1.61	-1.07 ± 0.30

Fluorescence spectrophotometry analysis of hAuNRs specificity to synthetic complement after incubation at 37 °C for 1 h shows a small increase in total fluorescence output (Figure 33). However, there is thought to be significant room for improvement in the optimization of surface ligands that will most certainly reduce background signal.

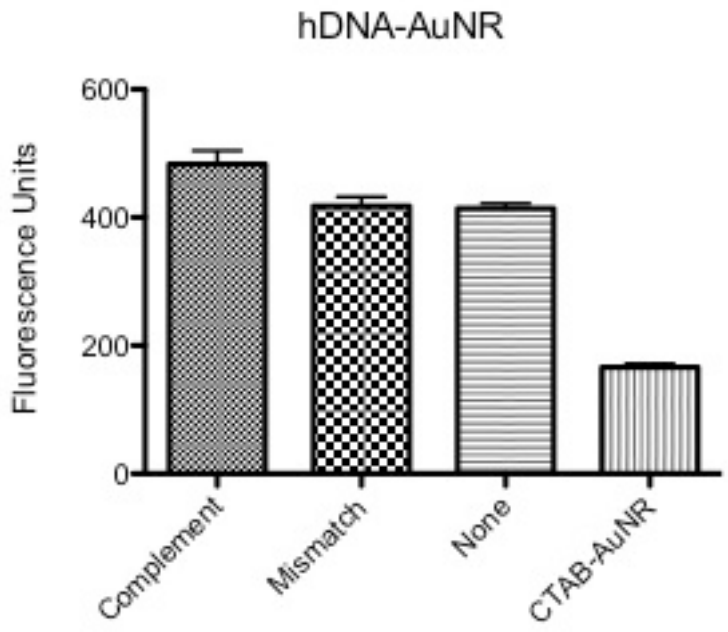

Figure 33. Fluorescence data of hDNA-AuNRs shows total fluorescence increases with the addition of complement, but a poor S/N ratio.

Conclusions

In order to expand upon the current capabilities and applications of gold nanoparticle-MBs, I synthesized different shapes of gold nanoparticles, eventually focusing my efforts on gold nanorods. As the different structures have different surfactants and surface properties, numerous functionalization strategies were investigated. Hairpin DNA functionalization was achieved on AuNRs after on overgrowth step in which a thin layer of gold atoms were reduced on a preformed AuNR, masking the trace silver ions that are thought to complicate other functionalization strategies. Hairpin DNA on AuNRs showed a small increase in fluorescence upon complement binding. A series of optimization steps akin to those outlined in Chapter 2 would greatly improve the

S/N of the hAuNRs, creating a powerful “next-generation” hAuNP that, among other things, will allow for NIR imaging at significant depths in living tissues.

References

1. Murphy, C.J., Sau, T.K., Gole, A.M., Orendorff, C.J., Gao, J., Gou, L., Hunyadi, S.E. and Li, T. (2005) Anisotropic metal nanoparticles: Synthesis, assembly, and optical applications. *J Phys Chem B*, **109**, 13857-13870.

2. Murphy, C.J., Gole, A.M., Hunyadi, S.E. and Orendorff, C.J. (2006) One-dimensional colloidal gold and silver nanostructures. *Inorg Chem*, **45**, 7544-7554.

3. Murphy, C.J., Gole, A.M., Hunyadi, S.E., Stone, J.W., Sisco, P.N., Alkilany, A., Kinard, B.E. and Hankins, P. (2008) Chemical sensing and imaging with metallic nanorods. *Chem Commun (Camb)*, 544-557.

4. Link, S., Mohamed, M.B. and El-Sayed, M.A. (1999) Simulation of the optical absorption spectra of gold nanorods as a function of their aspect ratio and the effect of the medium dielectric constant. *Journal of Physical Chemistry B*, **103**, 3073-3077.

5. Sprunken, D.P., Omi, H., Furukawa, K., Nakashima, H., Sychugov, I., Kobayashi, Y. and Torimitsu, K. (2007) Influence of the local environment on determining aspect-ratio distributions of gold nanorods in solution using Gans theory. *Journal of Physical Chemistry C*, **111**, 14299-14306.

6. Liao, H. and Hafner, J.H. (2005) Gold Nanorod Bioconjugates. *Chemistry of Materials*, **17**, 4636-4641.

7. Orendorff, C.J. and Murphy, C.J. (2006) Quantitation of metal content in the silver-assisted growth of gold nanorods. *J Phys Chem B*, **110**, 3990-3994.

8. Thomas, K.G., Barazzouk, S., Ipe, B.I., Joseph, S.T.S. and Kamat, P.V. (2004) Uniaxial plasmon coupling through longitudinal self-assembly of gold nanorods. *Journal of Physical Chemistry B*, **108**, 13066-13068.

9. Bardhan, R., Grady, N.K., Cole, J.R., Joshi, A. and Halas, N.J. (2009) Fluorescence enhancement by Au nanostructures: nanoshells and nanorods. *ACS Nano*, **3**, 744-752.

10. Yu, Y.Y., Chang, S.S., Lee, C.L. and Wang, C.R.C. (1997) Gold nanorods: Electrochemical synthesis and optical properties. *Journal of Physical Chemistry B*, **101**, 6661-6664.

11. Kim, F., Song, J.H. and Yang, P. (2002) Photochemical synthesis of gold nanorods. *J Am Chem Soc*, **124**, 14316-14317.

12. Martin, B.R., Dermody, D.J., Reiss, B.D., Fang, M.M., Lyon, L.A., Natan, M.J. and Mallouk, T.E. (1999) Orthogonal self-assembly on colloidal gold-platinum nanorods. *Advanced Materials*, **11**, 1021-1025.

13. Jana, N.R., Gearheart, L. and Murphy, C.J. (2001) Wet chemical synthesis of high aspect ratio cylindrical gold nanorods. *Journal of Physical Chemistry B*, **105**, 4065-4067.

14. Murphy, C.J. and Jana, N.R. (2002) Controlling the aspect ratio of inorganic nanorods and nanowires. *Advanced Materials*, **14**, 80-82.

15. Nikoobakht, B. and El-Sayed, M.A. (2001) Evidence for bilayer assembly of cationic surfactants on the surface of gold nanorods. *Langmuir*, **17**, 6368-6374.

16. Gao, J., Bender, C.M. and Murphy, C.J. (2003) Dependence of the Gold Nanorod Aspect Ratio on the Nature of the Directing Surfactant in Aqueous Solution. *Langmuir*, **19**, 9065-9070.

17. Elechiguerra, J.L., Reyes-Gasga, J. and Yacaman, M.J. (2006) The role of twinning in shape evolution of anisotropic noble metal nanostructures. *Journal of Materials Chemistry*, **16**, 3906-3919.

18. Sau, T.K. and Murphy, C.J. (2005) Self-assembly patterns formed upon solvent evaporation of aqueous cetyltrimethylammonium bromide-coated gold nanoparticles of various shapes. *Langmuir*, **21**, 2923-2929.

19. Senthil Kumar, P., Pastoriza-Santos, I., Rodriguez-Gonzalez, B., Javier Garcia de Abajo, F. and Liz-Marzan, L.M. (2008) High-yield synthesis and optical response of gold nanostars. *Nanotechnology*, **19**, 015606.

20. Decher, G. (1997) Fuzzy nanoassemblies: Toward layered polymeric multicomposites. *Science*, **277**, 1232-1237.

21. Lvov, Y., Decher, G. and Sukhorukov, G. (1993) Assembly of Thin-Films by Means of Successive Deposition of Alternate Layers of DNA and Poly(Allylamine). *Macromolecules*, **26**, 5396-5399.

22. Ruths, J., Essler, F., Decher, G. and Riegler, H. (2000) Polyelectrolytes I: Polyanion/polycation multilayers at the air/monolayer/water interface as elements for quantitative polymer adsorption studies and preparation of hetero-superlattices on solid surfaces. *Langmuir*, **16**, 8871-8878.

23. Lavalle, P., Gergely, C., Cuisinier, F.J.G., Decher, G., Schaaf, P., Voegel, J.C. and Picart, C. (2002) Comparison of the structure of polyelectrolyte multilayer films exhibiting a linear and an exponential growth regime: An in situ atomic force microscopy study. *Macromolecules*, **35**, 4458-4465.

24. Caruso, F., Caruso, R.A. and Mohwald, H. (1998) Nanoengineering of inorganic and hybrid hollow spheres by colloidal templating. *Science*, **282**, 1111-1114.

25. Antipov, A.A., Sukhorukov, G.B. and Mohwald, H. (2003) Influence of the ionic strength on the polyelectrolyte multilayers' permeability. *Langmuir*, **19**, 2444-2448.

26. Caruso, F., Lichtenfeld, H., Donath, E. and Mohwald, H. (1999) Investigation of electrostatic interactions in polyelectrolyte multilayer films: Binding of anionic fluorescent probes to layers assembled onto colloids. *Macromolecules*, **32**, 2317-2328.

27. Donath, E., Sukhorukov, G.B., Caruso, F., Davis, S.A. and Mohwald, H. (1998) Novel hollow polymer shells by colloid-templated assembly of polyelectrolytes. *Angewandte Chemie-International Edition*, **37**, 2202-2205.

28. Caruso, F. (2001) Nanoengineering of particle surfaces. *Advanced Materials*, **13**, 11-+.

29. Cho, J., Quinn, J.F. and Caruso, F. (2004) Fabrication of polyelectrolyte multilayer films comprising nanoblended layers. *J Am Chem Soc*, **126**, 2270-2271.

30. Blomberg, E., Poptoshev, E., Claesson, P.M. and Caruso, F. (2004) Surface interactions during polyelectrolyte multilayer buildup. 1. Interactions and layer structure in dilute electrolyte solutions. *Langmuir*, **20**, 5432-5438.

31. Mayya, K.S., Gittins, D.I., Dibaj, A.M. and Caruso, F. (2001) Nanotubes Prepared by Templating Sacrificial Nickel Nanorods. *Nano Letters*, **1**, 727-730.

32. Gittins, D.I. and Caruso, F. (2001) Tailoring the polyelectrolyte coating of metal nanoparticles. *Journal of Physical Chemistry B*, **105**, 6846-6852.

33. Mayya, K.S., Schoeler, B. and Caruso, F. (2003) Preparation and organization of nanoscale polyelectrolyte-coated gold nanoparticles. *Advanced Functional Materials*, **13**, 183-188.

34. Lee, S.E., Sasaki, D.Y., Perroud, T.D., Yoo, D., Patel, K.D. and Lee, L.P. (2009) Biologically functional cationic phospholipid-gold nanoplasmonic carriers of RNA. *J Am Chem Soc*, **131**, 14066-14074.

CHAPTER VI

WHERE'S THE SILVER? IMAGING TRACE SILVER COVERAGE ON THE SURFACE OF GOLD NANORODS

The development of seeded growth syntheses for gold nanorods (AuNRs) spurred a dramatic increase in interest in the optical properties and applications of these nanoparticles (AuNPs) (1). The original three-step seeded growth procedure using seed citrate-stabilized gold nanoparticles produced high aspect ratio AuNRs allowing researchers to clearly demonstrate their size and aspect ratio-dependent optical properties (2,3). However, it was the evolution of the silver-assisted seeded growth approach, utilizing a silver nitrate salt, which provided access to AuNRs in much higher yield (4-6). Shorter aspect ratios (AR) and single crystals are obtained compared to longer, penta-twinned AuNRs synthesized without silver(I) nitrate. Short AR rods present both transverse and longitudinal plasmon bands in the visible region of the spectrum, enabling a host of fascinating new AuNR-enabled sensing and imaging applications (7).

Despite over a decade of research, many key features of AuNR growth mechanisms remain poorly understood (8). Indeed, several synthesis components have been advanced as the driving force for anisotropy (9). Research into the role of silver ions in the silver-assisted seeded growth synthesis has been a particularly challenging area of mechanistic investigation. The ability to control the aspect ratio of these single-crystalline AuNRs by varying

the silver nitrate concentration used in the synthesis is well-established, but some disagreement exists as to the exact mechanism of its action (10). Three primary mechanisms have been proposed to account for the aspect ratio control that silver provides: (a) the deposition of a submonolayer quantity of silver metal on the longitudinal faces of the AuNR (silver under-potential deposition, UPD) (11,12); (b) the action of a cetyltrimethylammonium-Br-Ag^+ complex as a face-specific capping agent (12,13); and (c) silver acting with bromide to alter the shape of cetyltrimethylammonium bromide (CTAB) micelles from spherical to cylindrical shapes (soft template) (14).

Part of the challenge in establishing the role of silver in this synthesis stems from the instrumental challenges in characterizing the speciation and location of silver at the AuNR surface. Here we report the first experimental evidence on the position of silver ions present on AuNRs using a Tecnai Osiris equipped with a Super-X EDS energy dispersive X-ray spectroscopy (EDS) system. High sensistivity and high spectral count rates are enabled by the simultaneous X-ray detection of four solid-state detectors in conjunction with a high brightness Schottky-type field emission gun, allowing for element-specific mapping at subnanometer resolution across the periodic table (15). In particular, the system allowed for the spatial detection of trace amounts of silver without significantly damaging the AuNR.

The AuNRs in this study were synthesized using the popular seed-mediated, Ag-assisted growth procedure (6). Briefly, a solution of Au seed particles was prepared by the rapid reduction of $HAuCl_4$ by $NaBH_4$ in the

presence of CTAB. Growth solutions were then prepared by sequentially adding $HAuCl_4$, variable amounts of $AgNO_3$ (30-100 μM final concentration), and ascorbic acid to an aqueous solution of CTAB. The reactions were initiated by the addition of Au seed particles to the growth solutions, and then they were mixed gently and allowed to sit undisturbed overnight. The resulting nanorod solutions were dialyzed in deionized water for 3 days to remove unreacted reagents and excess surfactant.

Figure 34 shows the HRTEM image of a AuNR paired with corresponding scanning transmission electron microscopy (STEM)-EDS map showing the gold signal (gray scale) and the silver signal (red to yellow intensity scale). The silver signal follows the surface of the AuNR, indicating that the detected silver is on the surface rather than doped into the particle. Levels of silver ranged from approximately 1 to 4 atomic percent relative to gold, consistent to values from published ICP (16) and scanning electron microscopy EDS (6) measurements. The results of mapping 38 individual AuNRs suggest that the location of silver atoms does not correspond with any one particular facet as previously suggested (1,17,18). The analysis also indicates that the location of silver is found on all faces of the rod, sides, corners, and ends, seeming to give support to those growth mechanisms, like the proposed “soft template” mechanism, that do not rely on face-specific deposition of Ag species.

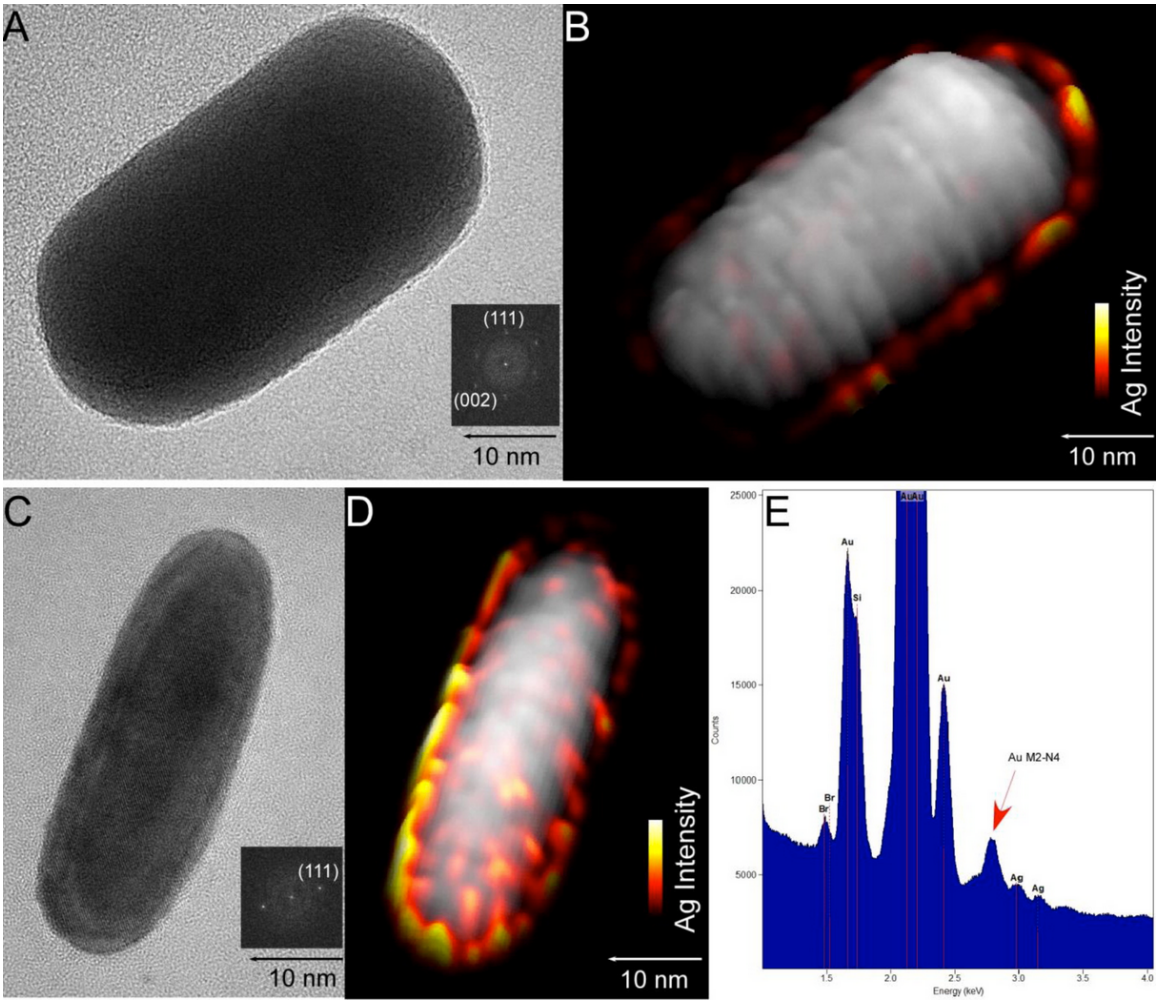

Figure 34. HRTEM images and correlated STEM-EDS maps of AuNRs (A and B, C and D). The EDS maps were generated by overlaying the background subtracted signals for gold and silver. The insets of A and C are fast Fourier transforms from the individual nanoparticles. (E) A typical EDS spectrum showing the presence of silver, gold, and bromine. The peak indicated with the red arrow is a gold M2-N4 transition typically too weak to detect.

Other detected elements include nitrogen, bromine, and trace amounts of iodine. Nitrogen and bromine atoms are found in CTAB, and iodine is known to be a common impurity in commercially available CTAB (19). No clear correlation with the AuNR structure was observed for any of these elements. The halide signals were of particular interest, since a number of reports have been recently

published regarding the specific use of halides to direct the formation of certain nanocrystal shapes (20,21); however, the signals were difficult to resolve, as signal would often be generated from excess surfactant that deposited on the support film, even after extensive purification of the AuNR solutions.

To confirm that the ubiquitous presence of Ag atoms seen on AuNRs is not simply due to poor elemental spatial resolution, we show that distinct regions of trace Ag content are discernible on a similar nanostructure. This was accomplished by imaging gold nano 'dog bones'. Nanoscale gold 'dog bone'-like structures have been formed by preferentially depositing more Au metal at the ends of AuNRs prepared by a seed-mediated approach (22,23). Fully formed AuNRs act as the seed particle, and additional Au atoms in solution are reduced by ascorbic acid. The Au atoms accumulate at the ends of the rod, inflating the corners of the particle, giving rise to the 'dog bone' morphology.

Au nano 'dog bones' were synthesized for this study by modification of a previously published procedure (23). Briefly, an aqueous solution of $HAuCl_4$ and ascorbic acid was added to a sample of purified AuNRs at room temperature. The sample was left undisturbed for 24 h before being purified by dialysis for three days. Figure 35 shows HRTEM images and STEM-EDS maps of two AuNR 'dog bones' produced from a sample of seed-mediated synthesized AuNR. In each case, the silver intensity is shown to be greater in the indentations on the ends than in the inflated lobes. Since the only metal atoms being reduced at this time were Au, the deposition in these specific areas creates relatively Ag-rich and Ag-poor regions on the same nanostructure. It is also important to note that this

was achieved without adding to the trace amounts of silver used to synthesize the original AuNR, confirming that the unbiased localization of silver seen on AuNRs in this study is neither a result of poor spatial resolution nor an undetectable amount of Ag atoms present.

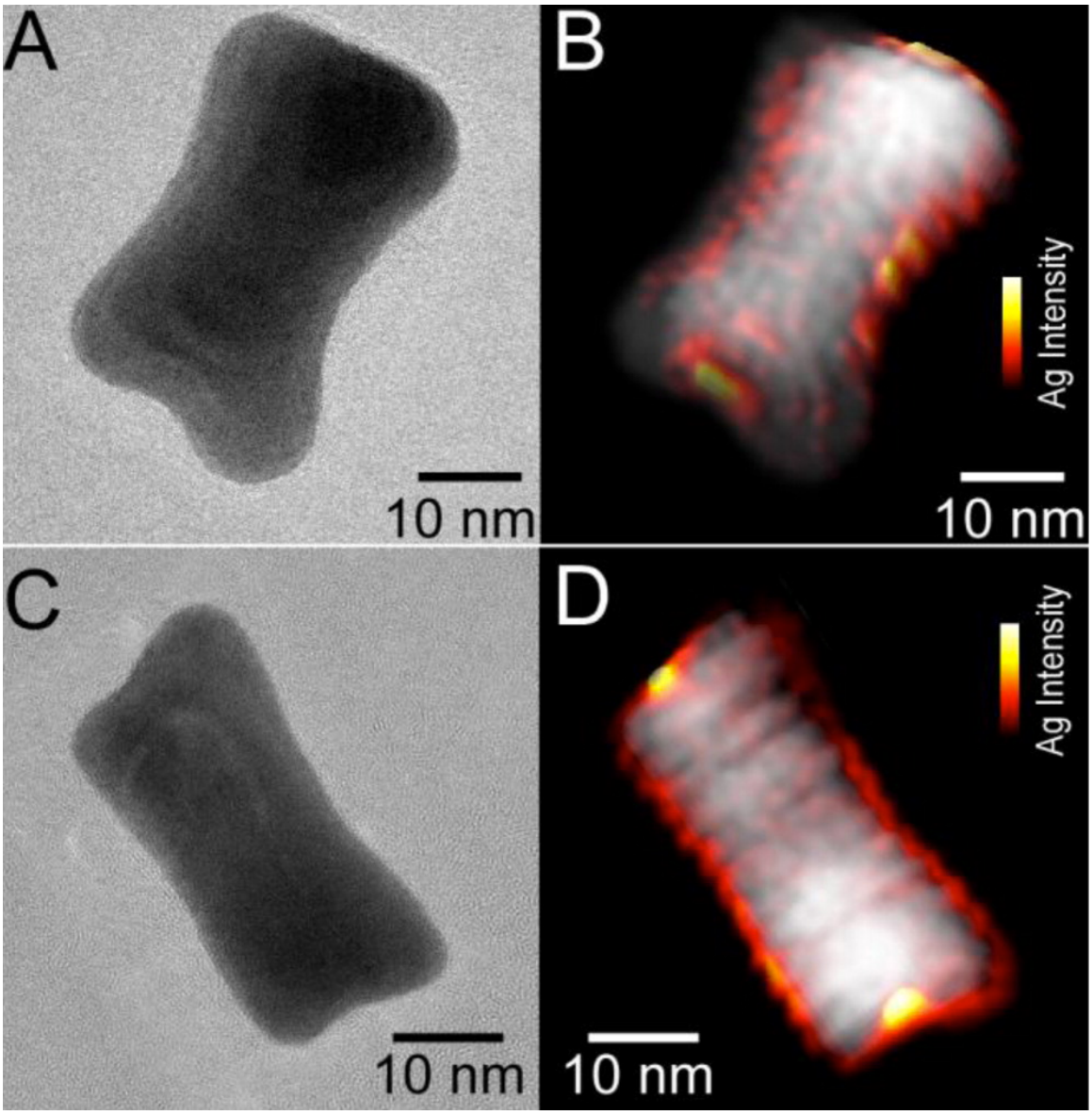

Figure 35. HRTEM images (A and C) and correlated STEM-EDS maps (B and D) of gold nano 'dog bones'. The silver EDS intensity is, in general, greater in the regions that are not formed as a result of excess Au atom depostion.

The analysis described here presents another step toward the full structural and elemental characterization of AuNRs. Such information will provide needed insight into the mechanisms by which AuNRs grow, ultimately allowing for the improvement of the performance of AuNR syntheses. Further, STEM-EDS mapping will have a notable impact in the field by allowing for the characterization of modified AuNRs by evaluating efficiencies of surface modification and ligand exchange protocols. It is our hope that insights into the composition of nanomaterials like these will ultimately allow for improved seeded growth reactions, manipulating anisotropic AuNP shapes in more exquisite detail, and reduce our reliance on large amounts of cytotoxic surfactants to achieve shape control. Beyond AuNPs, trace metals play important roles in many types of nanomaterials syntheses (24-26). The ability to visualize and understand the role of these trace elements on nanostructures will enhance capabilities to achieve new complex architectures and more efficient syntheses for existing systems.

References

1. Murphy, C.J., Sau, T.K., Gole, A.M., Orendorff, C.J., Gao, J., Gou, L., Hunyadi, S.E. and Li, T. (2005) Anisotropic metal nanoparticles: Synthesis, assembly, and optical applications. *J Phys Chem B*, **109**, 13857-13870.

2. Jana, N.R., Gearheart, L. and Murphy, C.J. (2001) Wet chemical synthesis of high aspect ratio cylindrical gold nanorods. *Journal of Physical Chemistry B*, **105**, 4065-4067.

3. Jana, N.R., Gearheart, L. and Murphy, C.J. (2001) Seed-mediated growth approach for shape-controlled synthesis of spheroidal and rod-like gold nanoparticles using a surfactant template. *Advanced Materials*, **13**, 1389-1393.

4. Nikoobakht, B. and El-Sayed, M.A. (2003) Preparation and growth mechanism of gold nanorods (NRs) using seed-mediated growth method. *Chemistry of Materials*, **15**, 1957-1962.

5. Sau, T.K. and Murphy, C.J. (2004) Room temperature, high-yield synthesis of multiple shapes of gold nanoparticles in aqueous solution. *J Am Chem Soc*, **126**, 8648-8649.

6. Sau, T.K. and Murphy, C.J. (2004) Seeded high yield synthesis of short Au nanorods in aqueous solution. *Langmuir*, **20**, 6414-6420.

7. Stone, J., Jackson, S. and Wright, D. (2011) Biological applications of gold nanorods. *Wiley Interdiscip Rev Nanomed Nanobiotechnol*, **3**, 100-109.

8. Lohse, S.E. and Murphy, C.J. (2013) The Quest for Shape Control: A History of Gold Nanorod Synthesis. *Chemistry of Materials*, **25**, 1250-1261.

9. Vigderman, L., Khanal, B.P. and Zubarev, E.R. (2012) Functional gold nanorods: synthesis, self-assembly, and sensing applications. *Adv Mater*, **24**, 4811-4841, 5014.

10. Murphy, C.J., Thompson, L.B., Chernak, D.J., Yang, J.A., Sivapalan, S.T., Boulos, S.P., Huang, J.Y., Alkilany, A.M. and Sisco, P.N. (2011) Gold nanorod crystal growth: From seed-mediated synthesis to nanoscale sculpting. *Current Opinion in Colloid & Interface Science*, **16**, 128-134.

11. Grzelczak, M., Perez-Juste, J., Mulvaney, P. and Liz-Marzan, L.M. (2008) Shape control in gold nanoparticle synthesis. *Chem Soc Rev*, **37**, 1783-1791.

12. Jain, P.K., Huang, X., El-Sayed, I.H. and El-Sayed, M.A. (2008) Noble metals on the nanoscale: optical and photothermal properties and some applications in imaging, sensing, biology, and medicine. *Acc Chem Res*, **41**, 1578-1586.

13. Niidome, Y., Nakamura, Y., Honda, K., Akiyama, Y., Nishioka, K., Kawasaki, H. and Nakashima, N. (2009) Characterization of silver ions adsorbed on gold nanorods: surface analysis by using surface-assisted laser desorption/ionization time-of-flight mass spectrometry. *Chem Commun (Camb)*, 1754-1756.

14. Jana, N.R. (2005) Gram-scale synthesis of soluble, near-monodisperse gold nanorods and other anisotropic nanoparticles. *Small*, **1**, 875-882.

15. Schlossmacher, P., Klenov, D.O., Freitag, B. and von Harrach, H.S. (2010) Enhanced Detection Sensitivity with a New Windowless XEDS System for AEM Based on Silicon Drift Detector Technology. *Microscopy Today*, **18**, 14-20.

16. Orendorff, C.J. and Murphy, C.J. (2006) Quantitation of metal content in the silver-assisted growth of gold nanorods. *J Phys Chem B*, **110**, 3990-3994.

17. Nikoobakht, B. and El-Sayed, M.A. (2001) Evidence for bilayer assembly of cationic surfactants on the surface of gold nanorods. *Langmuir*, **17**, 6368-6374.

18. Leontidis, E., Kleitou, K., Kyprianidou-Leodidou, T., Bekiari, V. and Lianos, P. (2002) Gold colloids from cationic surfactant solutions. 1. Mechanisms that control particle morphology. *Langmuir*, **18**, 3659-3668.

19. Smith, D.K., Miller, N.R. and Korgel, B.A. (2009) Iodide in CTAB prevents gold nanorod formation. *Langmuir*, **25**, 9518-9524.

20. Lohse, S.E., Burrows, N.D., Scarabelli, L., Liz-Marzán, L.M. and Murphy, C.J. (2014) Anisotropic Noble Metal Nanocrystal Growth: The Role of Halides. *Chemistry of Materials*, **26**, 34-43.

21. Langille, M.R., Personick, M.L., Zhang, J. and Mirkin, C.A. (2012) Defining rules for the shape evolution of gold nanoparticles. *J Am Chem Soc*, **134**, 14542-14554.

22. Xu, X.D. and Cortie, M.B. (2006) Shape change and color gamut in gold nanorods, dumbbells, and dog bones. *Advanced Functional Materials*, **16**, 2170-2176.

23. Gou, L.F. and Murphy, C.J. (2005) Fine-tuning the shape of gold nanorods. *Chemistry of Materials*, **17**, 3668-3672.

24. Chu, Y.T., Chanda, K., Lin, P.H. and Huang, M.H. (2012) Aqueous phase synthesis of palladium tripod nanostructures for Sonogashira coupling reactions. *Langmuir*, **28**, 11258-11264.

25. Chen, Y.H., Hung, H.H. and Huang, M.H. (2009) Seed-mediated synthesis of palladium nanorods and branched nanocrystals and their use as recyclable Suzuki coupling reaction catalysts. *J Am Chem Soc*, **131**, 9114-9121.

26. Li, L., Hu, F., Xu, D., Shen, S. and Wang, Q. (2012) Metal ion redox potential plays an important role in high-yield synthesis of monodisperse silver nanoparticles. *Chem Commun (Camb)*, **48**, 4728-4730.

APPENDIX A

RNAStructure Protocols

(Version 5.6)

Fold a New Sequence:

1. Click “New Sequence” icon.
2. Enter a title for the new sequence in “Title” box. Input the RNA sequence (in CAPS) in the “Sequence” box.
3. Click “Fold as RNA”.
4. Enter a name for the .seq file (Sequence File) and choose the destination folder for the generated files.
5. Click “Save”. The file will be saved as a sequence file, and a “CT File” (.ct) will automatically be generated. This file contains the sequence with base pair information.
6. Use the default Suboptimal Structure Parameters. Start fold.
7. Click “OK” to show the .ct file of the folded sequence.

Generate Probe Sequences:

1. Click “RNA OligoWalk” icon.
2. Click “CT File” button and choose .ct file of folded mRNA sequence from above. A report file (.rep) will be automatically generated in the same folder.

3. Use the default mode, “Break Local Structure”, for calculating the free energy of intramolecular structure of the oligonucleotide and of the local RNA structure predicted. In this mode, the target structure breaks wherever the oligonucleotide binds ($\Delta G_{break\ target}$), and oligonucleotides lose pairs in self-structures ($\Delta G_{oligo\text{-}oligo}$ and $\Delta G_{oligo\text{-}self}$) and gain pairs in oligonucleotide-target binding (ΔG_{duplex}). This algorithm calculates the equilibrium affinity of a set-length complementary oligonucleotide to the RNA target and predicts its overall free energy of binding while taking into account stability of the newly formed duplex, local secondary structure within the target RNA, as well as intermolecular and intramolecular secondary structures formed by the oligonucleotide (1).
4. Run OligoWalk calculation for an oligonucleotide concentration of 1 uM, ranging in length from 18 to 25 nucleotides, including suboptimal target structures.
5. The ΔG bar graph generated will facilitate the “walk” of the oligonucleotide on the RNA sequence, one nucleotide at a time, thus obtaining information about each oligonucleotide/RNA hybrid formed.
6. Compile in one Excel sheet the information for all lengths of oligonucleotide files (18-25) and sort by decreasing $\Delta G_{overall}$.
7. Choose a target region that generates the most negative (-) kcal/mol values for $\Delta G_{overall}$ that does not contain more than three consecutive G or C bases.

8. Check selected sequence in BLAST to see if sequence is unique to target mRNA.
9. Add T10 stem and Hairpin formation region and fold in IDT UNAfold to ensure that lowest energy conformation is a hairpin structure.

APPENDIX B

Supplementary Information for Chapter III

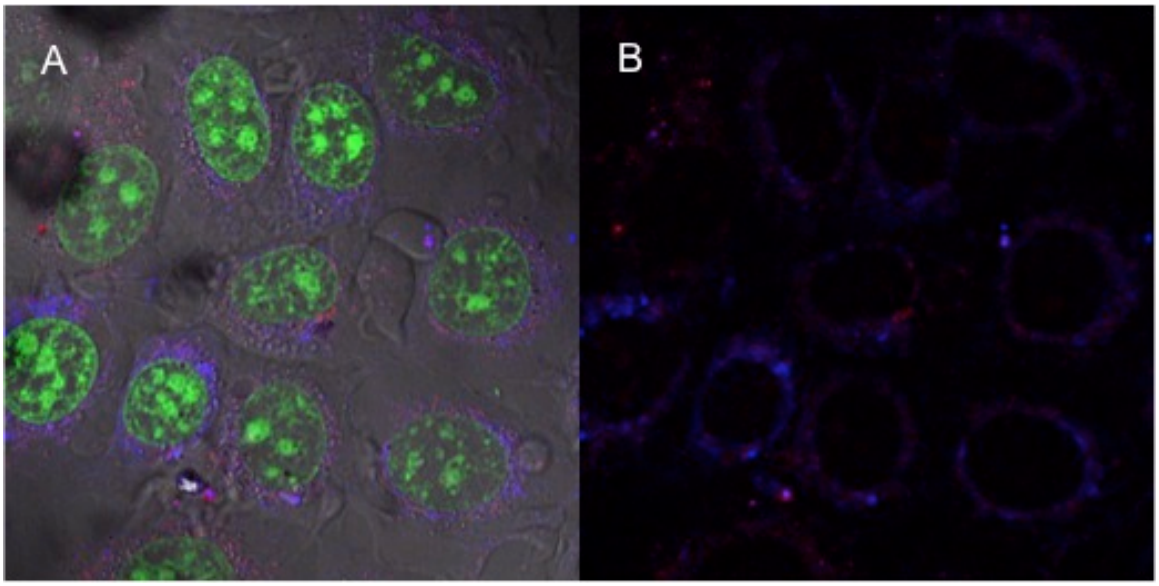

Figure 36. Confocal microscopy image of MMP-13 hAuNPs (blue) in MCF-7 cells. Also shown are Syto-13 nuclear stain (green) and GAPDH-specific hAuNPs (red). 100x magnification.

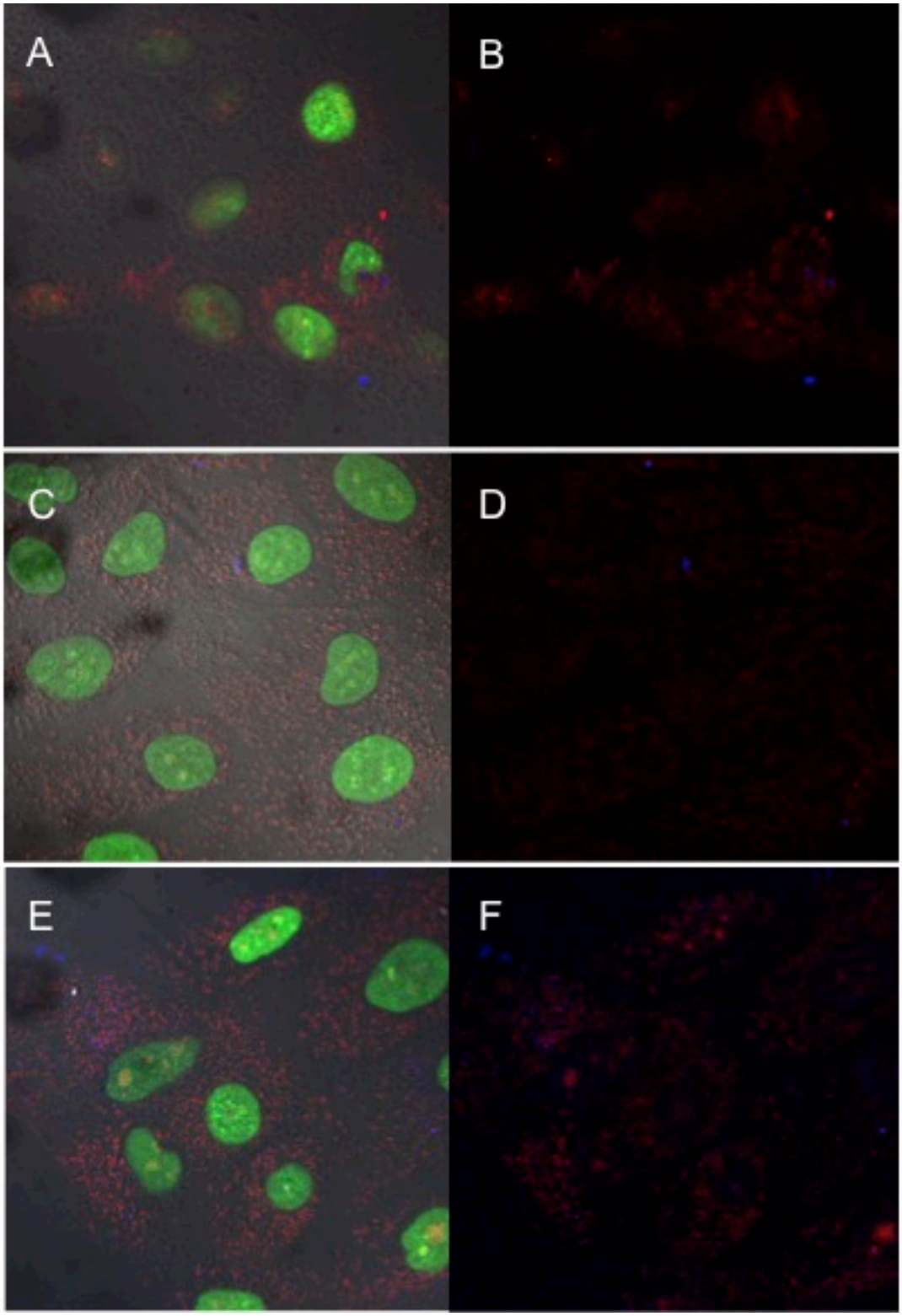

Figure 37. Comparison of MMP hAuNP activation in MCF-10A cells. Blue fluorescence is specific for MMP-13 (A & B), MMP-26 (C & D), and the negative control MMP-26scram (E & F). Red fluorescence is GAPDH-specific hAuNP. Green is Syto13 nuclear counterstain. 100x magnification.

APPENDIX C

Supplementary Information for Chapter V

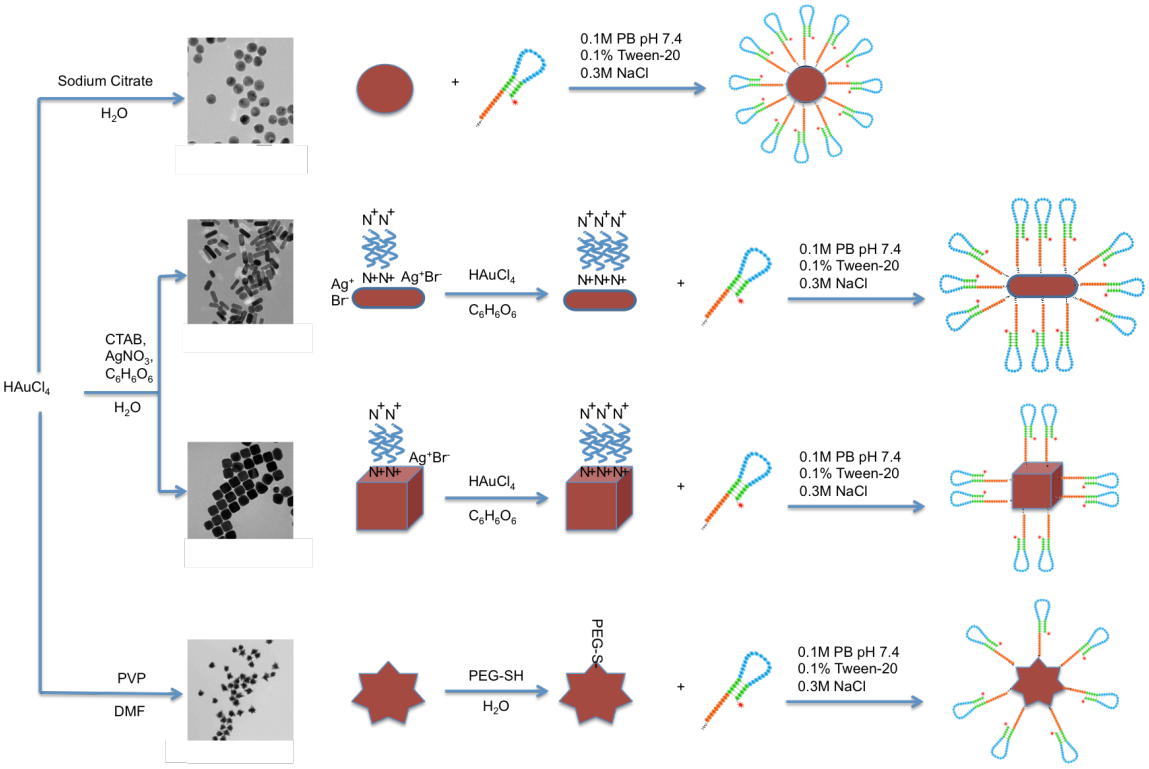

Figure 38. Schematic depicting hDNA functionalization strategies for varying AuNP constructs.

APPENDIX D

Supplementary Information for Chapter VI

STEM-EDS Procedure

Graphene-coated support films were dipped into purified AuNR solutions. Any excess solvent was then wicked away. STEM-EDS was performed using a Tecnai Osiris equipped with a Super-X EDS system. STEM-EDS maps were acquired with an ~0.3 nm probe size with a measured screen current of ~0.9 nA and a maximum peak count rate of ~20 kcps. Drift corrected EDS mapping was performed using TEM Imaging and Analysis (TIA) software. The per pixel dwell time was set to 0.5 seconds and the average map time was approximately 15 minutes. Longer dwell times result in noticeable changes in the nanorod appearance. The EDS maps in Figure 34 and Figure 35 were smoothed, and the rendered in 3D using ImageJ.

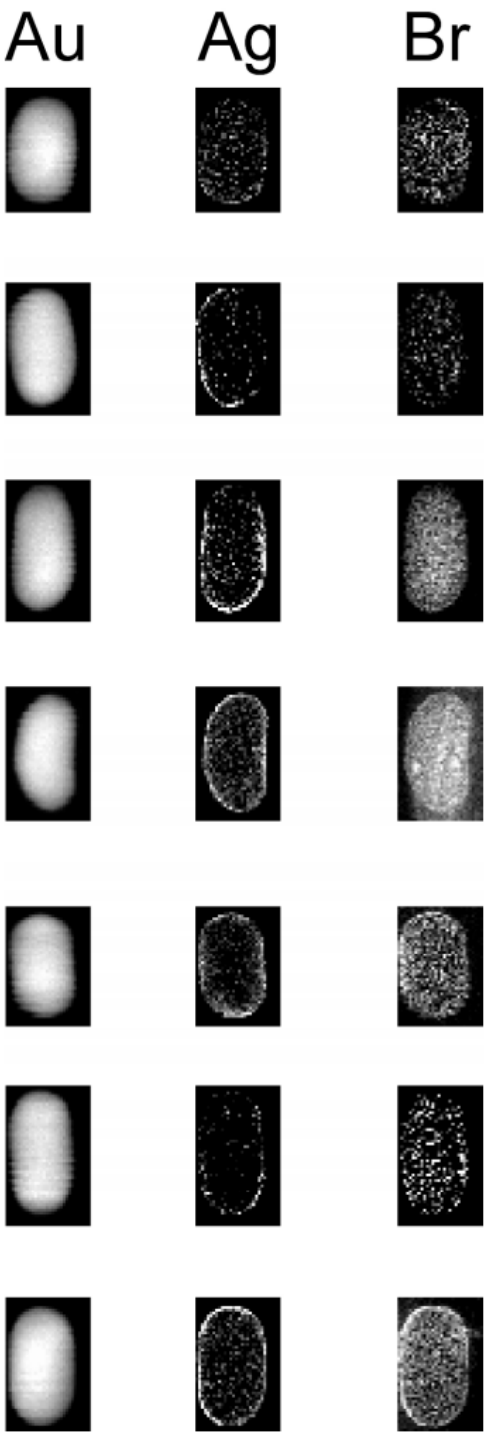

Figure 39. Background subtracted EDS maps of several AuNRs. In general, the bromine signal tracks with the gold EDS signal, indicating poor deconvolution.

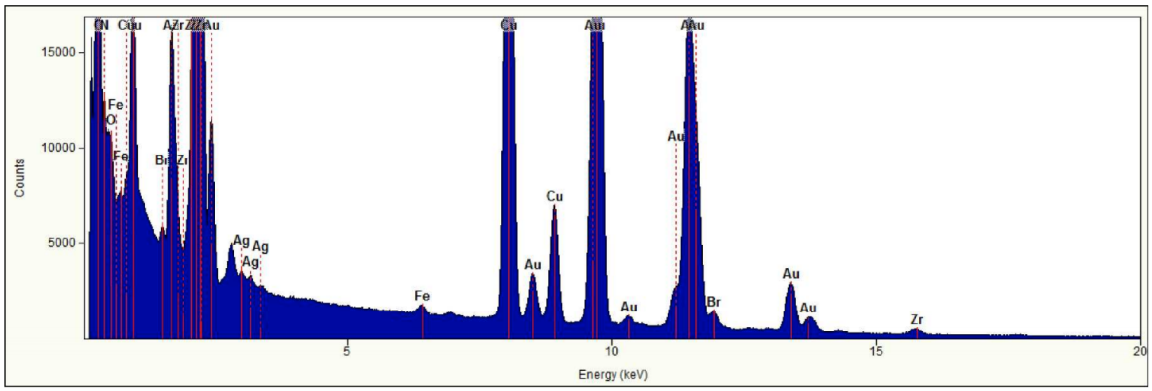

Figure 40. Typical EDS Spectrum of AuNR map. The above spectrum is generated by integrating all the pixels from an individual EDS map. Peaks from copper are from the TEM grid and the iron and zirconium peaks are system peaks.

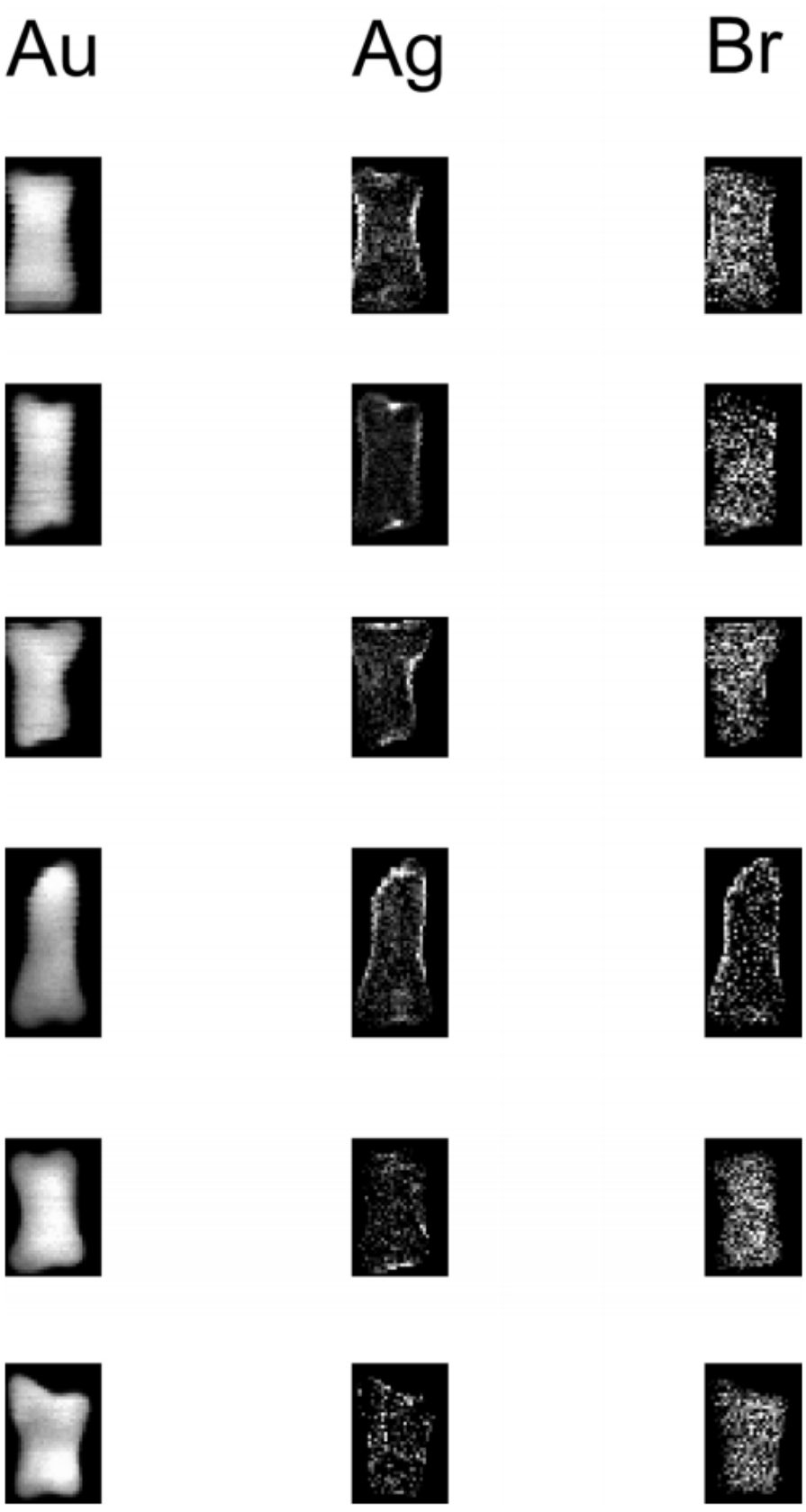

Figure 41. Background subtracted EDS maps for AuNR ‘dog bone’ structures.

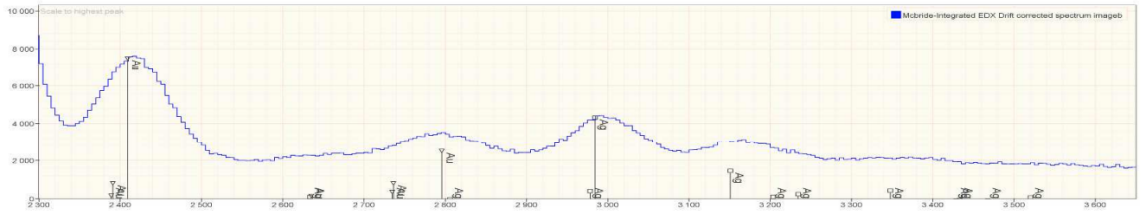

Figure 42. Screen shot of NIST DTSA-II identifying Au M2-N4 centered around 2.76 keV.

References

1. Sugimoto, N., Nakano, S., Katoh, M., Matsumura, A., Nakamuta, H., Ohmichi, T., Yoneyama, M. and Sasaki, M. (1995) Thermodynamic parameters to predict stability of RNA/DNA hybrid duplexes. *Biochemistry*, **34**, 11211-11216.